The Effect of Surface Plasmonic Resonances and Enhancement of the Optical Response on Magneto-Plasmonic $Fe_3O_4@Ag$ Spherical Core-Shell Nanoparticles

By

Kinde Yeneayehu

A THESIS SUBMITTED TO THE GRADUATE PROGRAMS IN PARTIAL FULFILLMENT
OF THE REQUIREMENTS FOR THE DEGREE OF DOCTOR OF PHILOSOPHY IN
CONDENSED MATTER PHYSICS
AT
ADDIS ABABA UNIVERSITY
ADDIS ABABA, ETHIOPIA
DECEMBER 2024

ADDIS ABABA UNIVERSITY
DEPARTMENT OF PHYSICS

The undersigned hereby certify that they have read and recommend to the Graduate Programs for acceptance a thesis entitled "**The Effect of Surface Plasmonic Resonances and Enhancement of the Optical Response on Magneto-Plasmonic** $Fe_3O_4@Ag$ **Spherical Core-Shell Nanoparticles**" by **Kinde Yeneayehu** in partial fulfillment of the requirements for the degree of **Doctor of Philosophy in Condensed Matter Physics**.

Dated: December 2024

External Examiner: ______________________
Dr. Nebiyu Gemechu

Research Supervisor: ______________________
Prof. Teshome Senbeta and Dr. Belayneh Mesfin

Internal examiner: ______________________
Prof. Fekadu Gashaw

____
Dr. Kenate Nemera (Chairman)

ADDIS ABABA UNIVERSITY

Date: **December 2024**

Author: **Kinde Yeneayehu**

Title: **The Effect of Surface Plasmonic Resonances and Enhancement of the Optical Response on Magneto-Plasmonic $Fe_3O_4@Ag$ Spherical Core-Shell Nanoparticles**

Department: **Physics**

Degree: **Ph.D.** Convocation: **June** Year: **2025**

Permission is herewith granted to Addis Ababa University to circulate and to have copied for non-commercial purposes, at its discretion, the above title upon the request of individuals or institutions.

Signature of Author

Dedicated To My Family.

Table of Contents

List of Figures

Abstract

In this work, the optical properties of $Fe_3O_4@Ag$ core/shell spherical nanostructures embedded in a dielectric host matrix are investigated theoretically. The theoretical analysis is carried out based on the electrostatic approximation and Maxwell-Garnet effective medium theory to obtain the effective electric permittivity and magnetic permeability, electric polarizability, refractive index, absorbance, as well as the corresponding scattering and absorption cross-sections. Moreover, for a fixed size of NPs (of radius $r_2 = 30\ nm$) numerical analysis is carried out to see the effect of varying the metal fraction (β), the filling fraction (f), and the permittivity (ε_h) of the host matrix on the optical properties of the nanostructures. The results show that graphs of real and imaginary parts of polarizability, refractive index, absorbance, extinction cross-sections as a function of wavelength possess two sets of resonance peaks in the UV and visible regions. These sets of peaks arise due to the strong couplings of the surface plasmon oscillations of silver with the semiconductor/dielectric at the inner (Fe_3O_4/Ag) and outer (Ag/host) interfaces. Moreover, the two set of resonance peaks are found to be enhanced with an increase of β, f, or ε_h; keeping two of these parameters constant at a time. On the other hand for the case of absorption and extinction cross-sections, as β increases, the absorption and scattering cross-sections are blue-shifted in the first peak and red shifted in the second set of peaks. Similarly, as ε_h increases or as β decreases, the sets of resonance peaks for extinction cross-section get enhanced. The results obtained might be utilized in a variety of applications that are designed to integrate plasmonic effects of noble metals with magnetic semiconductors in a core/shell nanostructure ranging from UV to Visible spectral regions.

Abbreviations

- MNP - Magnetic Nanoparticle
- CSNP - Core-shell nanoparticle
- CSNS - Core-shell nanostructure
- DF - Dielectrics function
- EMW - Eelectromagnetic Wave
- NP - Nanoparticle
- NS - Nanostructure
- PR - Plasmonic resonance
- QD - Quantum dot
- SPR - Surface plasmonic resonance
- LSPR - Localized surface plasmon resonance
- SERS - Surface Enhanced Resonance Scattering Or Spectroscopy
- RI - Refractive index
- UV-Vis - Ultraviolet visible

Acknowledgements

First of all I would like to be grateful to almighty God for the accomplishment of this work and adventure of experience I have been through.

In this study, it is impossible to complete without the contribution and support of many individuals and institutions. It would be thus fair to mention people and institutions that have provided much needed support for the successful completion of this work.

Primarily, I am genuinely thankful to my advisors, Prof. Teshome Senbeta and Dr. Belyaneh Mesfin, for their willingness to help me in every thing I wanted, for their brotherly approach, for their followups, for their insightful professional assistance and endless academic support on this study. Thank you all for your unforgettable and invaluable support. I want to extend my gratitude to Ms. Tsilat Adinew for her help in paper works, like finance, documentation and related facilities.

It is my pleasure to acknowledge all the staff members of the Physics department at ASTU for their enormous support and providing a good atmosphere in the department. I will always be grateful to them for helping me to develop the scientific approach and attitude. Dr. Gashaw from ASTU, I am very thankful for your encouragement, for numerous discussions on related topics of my studies, you are the man in need and indeed. It would not have been possible to carry out this research without the financial support for research work from Addis Ababa University and Adama Science and Technology University, is also acknowledged for the study leave.

Finally, and most importantly, I would like to express my deepest gratitude to my dearest wife Tiruwork for her support, encouragement, patience and love. I owe you love and respect with this little phrases. I would like to thank my lovely daughters Haset, Hiwot and Eleni for their wonderful smile and playful time that you were always able to create. I thank my parents, brothers and sisters and all my friends and colleagues for their continuous support, concern and faith in me and allowing me to be as ambitious as I wanted. Thank all for your support.

Chapter 1

Introduction

Nanomaterials have attracted a lot of attention in recent years, on account of their distinct electrical, magnetic, and optoelectronic characteristics as well as their many uses in novel nano-devices [1]. In everyday life as well as research, the terms "nanotechnology," "nanoscience," and "nanomaterials" are now widely used. When nanoparticles and nanostructures formed in the first meteorites following the big bang, the history of nanomaterials (NMs) officially began. Afterwards nature produced a vast array of additional nanoparticles and nanostructures. Compared to the same chemical substances in a larger size, NMs can display distinct optical, mechanical, magnetic, and conductive properties. Gaining more insight into the characteristics of NM opens the door to the possibility of creating novel materials in the future, which could raise standards of living. NMs are finding their way into the market, starting to function as commodities, and finding their way into a variety of cutting-edge technological applications and goods, including a broad spectrum of consumer goods. However, the different types of NMs (i.e., organic, inorganic, carbon, and composite based NMs) exhibit distinct physical, chemical, and biological properties, which can be harnessed for specific applications [2].

There are numerous instances of ancient artifacts using nanocomposites. A stunning example was the Lycurgus cup (Fig. 1.1), a glass that changes color when light passes through it and was created by the Romans in AD 400. The glass's composition is Au/Ag alloyed nanoparticles, which are arranged to give the appearance of green when reflected light strikes the cup, but expose a vivid red when light passes through it.

Figure 1.1: An example of the application of nanotechnology in antiquity is the Lycurgus cup, Placed in the British Museum in London[2].

understanding light matter Interaction reveals novel optical phenomena which are prerequisites for indicating unrivalled optical properties of these materials. The linear and nonlinear optical response of metal nanoparticles is specified by oscillations of the surface electrons in the Coulomb potential formed by the positively charged ionic core. This type of excitation is called the Surface Plasmon (SP). In 1908 Mie proposed a solution of Maxwell equations for spherical particles interacting with plane electromagnetic waves, which explains the origin of surface plasmon resonance (SPR) in the extinction spectra and colouration of metal colloids. During the last century optical properties of nanoparticles have extensively been studied and metal-dielectric nanocomposites have found various applications in different fields of science and technology [3] -[5]. Since the optical properties of metal nanoparticles are governed by SPR, they are strongly dependent on the nanoparticles size, shape, concentration and spatial distribution as well as on the properties of the surrounding matrix. Control over these parameters enables such metal dielectric nanocomposites to become promising media for development of novel non-linear materials, nanodevices and optical elements [6]-[8]

Nanoparticles have a great importance in present and future potential technology, mainly in structures and devices with physical, chemical and biological properties increased or created from those of the bulk materials [9]. Semiconductor nanostructured materials are significantly cherished because they can link the gap between small molecules and bulk materials. The nanostructured materials show distinct optical and electronic properties when their size varies in the range of $1-100$ nm with the variation of dimension and their density of states can be classified as (1) two-dimensional, e.g., nano-sheets or thin films or quantum wells; (2) one-dimensional, e.g., quantum wires; and (3) zero-dimensional, e.g., quantum dots as shown Fig. 1.2[10].

It is well known that decreasing of materials size to the nanometer scale, such as nanotubes, nanorods, and nanowires, have attracted considerable attention due to their unique and extraordinary physical properties, shape, polarization direction of incident light and surrounding medium-dependent of the dielectric function of the host matrix. The nanometer-sized magnetite (Fe_3O_4) is one of the ferromagnetic

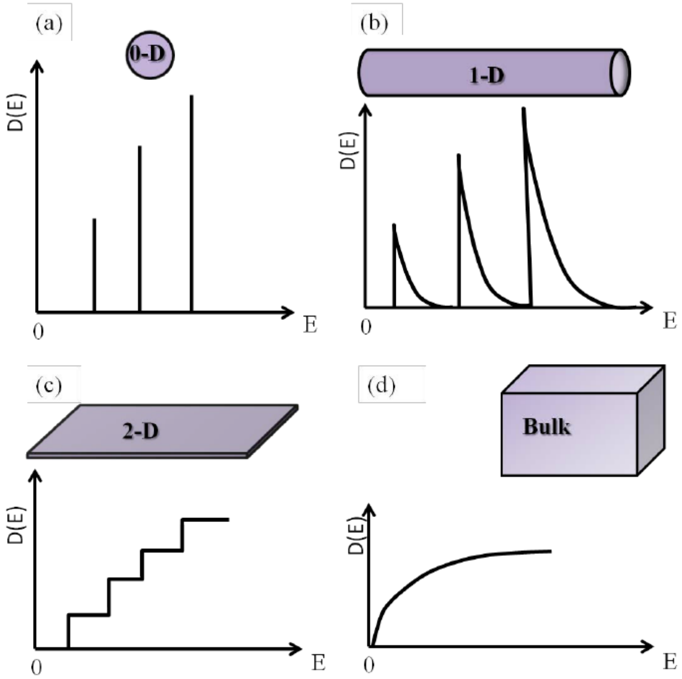

Figure 1.2: Schematic representation of density of states: (a) 0-dimension (0-D), (b) 1- dimension (1-D), (c) 2-dimension (2-D) and (d) 3-dimension(3-D)[10].

materials that have been widely used as functional materials due to very attractive magneto-optical (MO) properties [9].

Magnetite (Fe_3O_4) nanoparticles, in particular, are attractive because of their high magnetic moment, nontoxic nature, and ease of synthesis. Magnetic iron oxide nanoparticles have recently become the focus of a considerable amount of research activities and have potential application in several areas, both in vivo and in vitro, as cell separation, immunoassay, immunomagnetic array, magnetic recording material such as audio and videotape, and high-density digital recording disks (magnetic storage), magnetic resonance contrast agent, magnetic ink printing and microwave absorption. Magnetic nanoparticles (MNPs) Fe_3O_4 are drawing increased attention due to their remarkable physical properties and their applications in various fields, not only in the field of biomedical care, but also as the alternating current hyperthermia, being considered one of the most promising techniques for cancer treatment, electrical energy storage and magnetic resonance imaging [10, 9], drug delivery [11, 12] gene therapy, and in environmental protection. In addition to their magnetic properties, the biomedical applicability of nanoscale magnetite particles is dependent upon their stability against aggregation in physiological environments, and the ability to predictably functionalize the particle surface for specific biomolecule interactions. Because of their large surface area to volume ratio and low surface charge at neutral pH, magnetite nanoparticles tend to aggregate in physiological environments, magneto-optics devices, sensors, catalysis, magnetic sensing and high frequency applications [13]-[15].

Magnetite constitutes the most abundant magnetic mineral in the Earths crust. Magnetite (Fe_3O_4) nanoparticles have attracted an increasing interest in the fields of nanoscience and nanotechnology because of the unique and novel physiochemical properties that can be attained according to their particle size (quantum size effect), shape morphology, and engineering form (films or selfassembled nanocrystals and ferrofluids) [16]. Magnetite is a mixed valence iron oxide, Fe_3O_4, with cubic inverse spinel structure (see Fig. 1.3) at room temperature is a prototype ferrimagnetic system that still attracts considerable attention mainly due to the presence of the so-called Verwey transition a structural phase transition accompanied by substantial changes of magnetic and electrical properties [17].

Metal nanoparticles have fascinated scientists for over a century and are the focus of interest because of their huge potential in nanotechnology. Nowadays, several

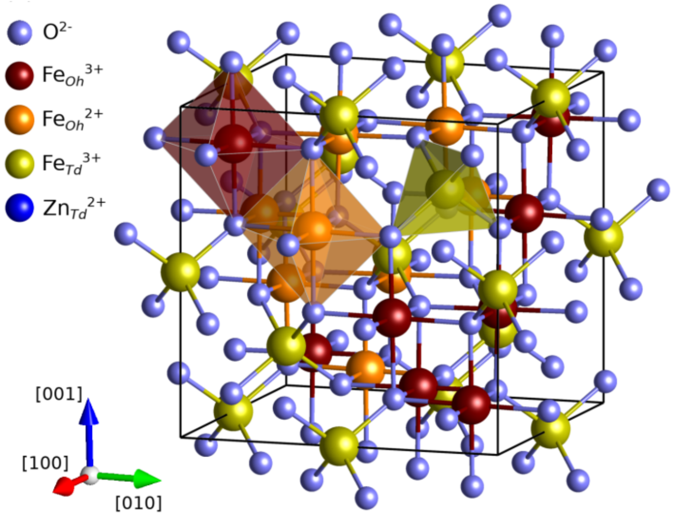

Figure 1.3: Schematic representation of: The cubic crystal structure of the inverse spinel Fe_3O_4,[18].

synthesis techniques are being developed so as to modify these properties. The metal nanoparticles show good compatibility, catalytic behavior, and surface enhanced Raman activity. Noble metal nanoparticles in general and their gold and silver analogue, in particular, attract huge research interest owing to their fabulous properties (electrical and optical) and diversity of applications including fluorescence imaging, biomedical applications and bio-engineering. Mankind has been ensnared by noble metals (gold and silver) since prehistoric times and applications of their nanoparticles have attracted attention for the last millennia, although understanding many of the phenomena at the nanoscale is very recent. Nanoscale analogues are being explored due to their unusual functional attributes quite unlike the bulk. As research in this area moves forward in nanomaterials, scientists are discovering novel application possibilities. Tunability of nanoparticle properties is possible by varying size, shape, composition or local environment present in them. By manipulating the chemical composition of materials at the nanoscale, their chemical, optical, electrical and other properties can be tailored precisely, which makes them ideal from an application point of view. Noble metal nanoparticles have large optical field enhancement resulting in strong scattering and absorption of light. The enhancement of the optical properties of noble metal nanoparticles arises due to resonant oscillations of their free electrons in the presence of light and this is known as localized surface plasmon resonance [LSPR] [19].

Noble metals of silver (Ag), gold (Au), and Copper (Cu) exhibit a special of the surface plasmon (SP) in the near ultraviolet (UV) to near infrared (NR) regions of the electromagnetic (EM) waves. SP is EM waves that are trapped on the surface because of their interaction with the free electrons of the metal. It can be either propagating called surface plasmon polaritons (SPPs) or propagating surface plasmons, in the planar bulk metal surface or localized surface Plasmon (LSP), in the case of NPs. At certainly excited photon energy, the collective oscillations of this electron interact with the incident photon; result in a maximum light absorption. This phenomenon is defined as localized surface plasmon resonance (LSPR). The property of LSPR produces the strong EM field enhancement in the vicinity of the metal nanoparticle. Therefore, there are many emerging applications utilizing these NPs, depending on the relative contribution of extinction, absorption, and scattering. For example in biomedical application, the LSPRs must be tuned to infrared region (IR) of the EM spectrum. Large scattering due to noble metal NPs can be used to increase the optical efficiency of the photovoltaic (PV) devices. Large EM field enhancement around the surface of noble metal NPs is used for surface enhanced raman spectroscopy

(SERS), and another application is plasmonic sensing. The LSPRs can be varied over the wide region of the EM spectrum; therefore, the wavelength can be tuned to obtain the required LSPR wavelength. There are several factors such as noble metal type, particle shape, particle size, the dielectric properties of the host medium, and composition of the NPs that can be optimized for obtaining this wavelength. By combining the individual metals, the LSPR can also be enhanced and tuned in a large region of the EM spectrum for a particular application [20].

Optical properties of metal NPs are especially important when specific applications are studied. In a $top-down$ approach, these properties can be described by their bulk dielectric function (ε), which may be represented as the sum of two terms: one corresponding to the contribution of free electrons based on the metal Drude model (intraband transitions) and the other corresponding to bound electrons (interband transitions (see Fig. 1.4).

As a result of the characteristics of this approach, the influence of each contribution depends on wavelength: for sufficiently large wavelengths (small photon energies), free-electron contribution dominates, while for smaller wavelengths (large photon energies), bound-electron contribution is more important. It is well known that the Drude model assumes that an incoming electromagnetic wave of frequency ω forces damped oscillations of the essentially free metal electrons, with a damping constant γ_{free}. The model involves a typical frequency (plasma frequency ω_p) above which the metal reflectivity decreases. To get an approximate expression for the Drude dielectric function, the condition $\omega \gg \gamma_{free}$ is often used. The size-dependent dielectric function is analyzed in the $50 - 3$ nm NPs size range, comparing the real and imaginary parts of the experimental dielectric function with the calculated values. Below 3 nm

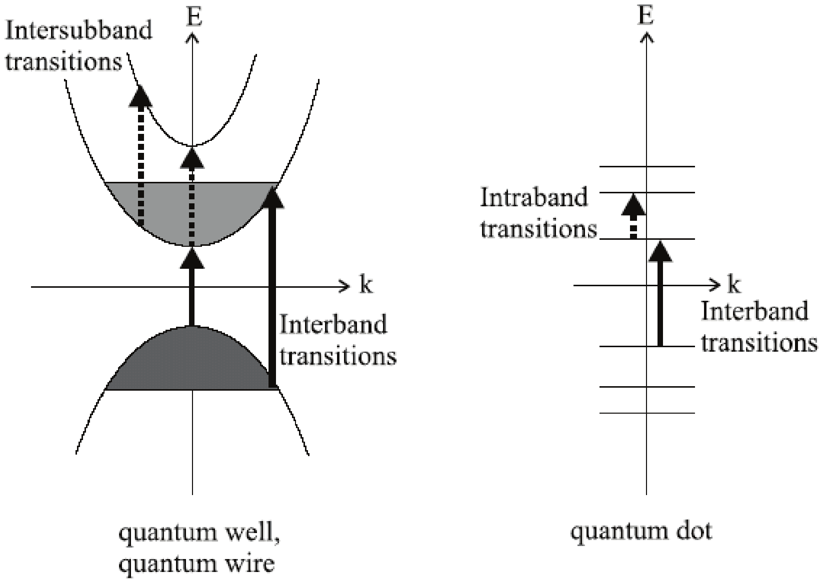

Figure 1.4: Interband and intraband transitions for quantum wells, quantum wires (left) and quantum dots (right). The diagrams show a scheme of the band/level structure [21].

size, the influence of bound electron contribution on the complex dielectric function is analyzed [22].

The unique characteristics of noble metal NPs, such as high surface-to-volume ratio, broad optical properties, ease of synthesis, and facile surface chemistry and functionalization hold pledge in the clinical field for cancer therapeutics. Noble metal NPs (e.g., gold, silver, or a combination of both) present highly tunable optical properties, which can be easily tuned to desirable wavelengths according to their shape (e.g., nanoparticles, nanoshells, nanorods, etc.), size (e.g., 1 to 100 nm), and composition (e.g., core/shell or alloy noble metals), enabling their imaging and photothermal applications under native tissue. Moreover, they can efficiently convert light or radiofrequencies into heat, thus enabling thermal ablation of targeted cancer cells [23].

Combining multiple materials in single nanoparticles has gained much attention in recent years due to the additional functionalities not exhibited in particles of individual materials. The combination of different materials allows to make completely new composite materials with a wide range of functional properties: mechanical, chemical, electrical, magnetic, optical and many others. Spherical nanoparticles fabricated from noble metals, such as silver (Ag), gold (Au), and semiconductor materials are a few examples of such composite NPs. They can exhibit extraordinary physical and chemical properties, which find a wide range of applications in nanotechnology. Alternatively, noble metals NPs embedded in a dielectric matrix exhibit extraordinary optical resonance, called localized surface plasmon resonance (LSPR). This is due to the collective oscillations of their free electrons with respect to a fixed lattice of positive ions when impinged upon by a light wave. However, these pure metals have some limitations related to high dissipative losses, leading to a large absorption and unwanted heating effects. The interplay between fluorescence and the plasmonic effect reportedly have significant potential for enhancement of solar cell efficiency. In biomedicine, this system can be used for drug delivery and cancer therapy [24].

The core-shell nanomaterials and nanostructures have become an important research area since few decades due to their potential applications in various fields like catalysts, industrial and biomedical applications, like molecular bioimaging, drug delivery, cancer therapy and so forth. The core-shell nanocomposites and nanostructure may be with different sizes and different shapes of core and shell thickness with different surface morphology. They may be spherical (see Fig. 1.5), centric, eccentric, star-like, or tubular in shape. Depending on the size and shape, their properties tune from material to another. Whenever the surface of the nanoparticles is modified by functional groups or molecules or coated with a thin layer of other materials (with different constituents), they show enhanced properties compared to the non-functionalized uncoated particles. There are different types of core-shell structure, like metal-core and different metal shell, metal-core and nonmetal shell, metal-core and polymer shell, nonmetal-core and nonmetal shell, polymer-core and nonmetal shell and polymer-core and polymer shell where the two polymers are different. For these six categories, the core and the shell materials may be reversed. Below is the schematic of core-shell nanoparticles. Recently, much attention has been focused on core shell metal nanoparticles based on gold, platinum, and palladium because their properties markedly differ from their bulk. These metal core-shell nanoparticles exhibit size induced quantum-size effects (i.e., electron confinement and surface effect) and can be exploited for a number of advanced functional applications as sensors, electronics, optoelectronics and catalysis. [25].

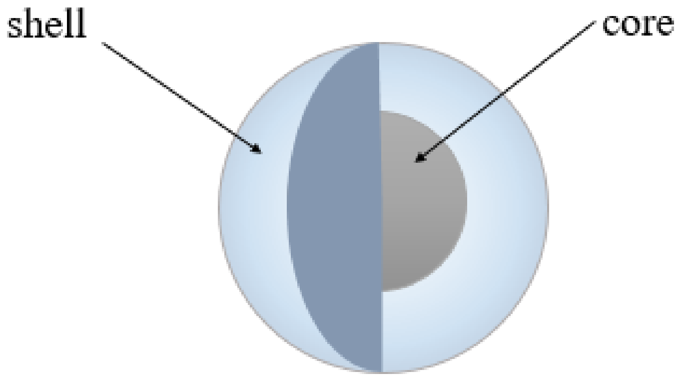

Figure 1.5: Schematic of a core-shell nanoparticle.

Magneto plasmonic nanomaterials like magnetite and silver attracts our attention towards their unique, unusual, interesting and extraordinary physical, optical, magnetic and optoelectronic properties that can differ significantly from the properties exhibited by the same bulk material. By carefully controlling the size, shape and surface functionality of nanoparticles, a wide range of optical, properties can be generated with many useful applications. An optical response in a nanomaterial can be created through several different mechanisms, depending on the nanomaterial size, composition and arrangement.

Metallic nanoparticles exhibiting localized surface plasmon resonances can show strong optical resonance for visible and near-infrared (NIR) wavelengths. Noble metal NPs have received considerable interest during the last few decades in the field of plasmonic, material sciences and biomedicine, due to their unique and intense optical, electronic, catalytic and tunable plasmonic properties. Noble metals like Au and

Ag can be treated as free-electron systems whose electronic and optical properties are determined by the conduction electrons alone. The collective oscillations of free conduction electrons of metallic NPs are observed when illuminated with the light of plasmon wavelength and is called localized surface plasmon resonance (LSPR).

Magnetic nanoparticles (MNPs) have lesser free electron contribution to the optical properties as compared to plasmonic NPs, due to which they do not exhibit LSPR, but these MNPs possess spontaneous magnetization. Magnetic nanoparticles provide target ability or control over a motion which makes their use in a biosensor, magnetic fluids, information storage, magnetic bioseparation, and catalysis. Magnetic nanostructures used in biomedical applications are usually composed of iron oxides, such as magnetite or maghemite because these materials combine high magnetic susceptibilities with very low toxicity.

Core-shell nanomaterials based on semiconductor cores coated by noble metallic shell are very interesting especially for biological and industrial applications. Magnetic-plasmonic core-shell nanoparticles, combining magnetic and plasmonic components, are promising structures for use in life sciences. Both plasmonic and magnetic nanomaterials are currently under intensive investigation for use in biomedical applications, and many findings have already been commercially exploited. In addition, Fe_3O_4 and Ag are relatively abundant, non-toxic, affordable, chemically stable, and simple to create as nanostructures with distinct morphologies and characteristics. However, the absorption efficiency of visible light is low and the band gap energy is broad for these two materials. Numerous successful strategies have been developed experimentally in the last few decades to address the limitations and improve the characteristics of magneto-plasmonics properties. Core-shell configurations are better when it comes to band gap energy and electron-hole recombination rate. In light of this, core-shell nanocomposites based on Fe_3O_4 and Ag respectively are investigated. To the best our knowledge, there have not been any reports of Fe_3O_4 based core-shell composite nanostructures theoretically and numerically investigated for the field of biomedicine.

In this dissertation, the effect of plasmonic resonance and the enhancement of optical response on magnetic/plasmonic core/shell spherical nanostructures embedded in a dielectric host matrix are investigated theoretically. The theoretical analysis is carried out based on the electrostatic approximation and Maxwell-Garnet effective medium theory to obtain the effective electric permittivity and magnetic permeability, electric polarizability, refractive index, absorbance, as well as the corresponding scattering and absorption cross-sections. These properties is based on the interfaces and oscillations of free electrons in which it possess two set of resonance peaks.

The **main objective** of this study is to investigate the enhancement of optical response and the effect of plasmonic resonance on magnetite@silver ($Fe_3O_4@Ag$) composite nanostructures.

The **specific objectives** of the study are:

- To study the enhancement of optical properties of spherical $Fe_3O_4@Ag$ core-shell nanocomposite.

- To investigate the effect of the size of nanoparticles on the optical responses of spherical $Fe_3O_4@Ag$ core-shell nanocomposite.

- To see the effects of metal fraction and dielectric function of host medium on the absorbance and electrical polarizability of spherical $Fe_3O_4@Ag$ core-shell nanocomposite.

- To study the effects of filling factor, metal fraction and dielectric function of host medium on the refractive index of spherical $Fe_3O_4@Ag$ core-shell nanocomposite.
- To investigate the effects of metal fraction and dielectric function of host medium on the absorption and extinction cross sections of spherical $Fe_3O_4@Ag$ core-shell nanocomposite.
- To analyze the plasmonic resonance response on magnetic@plasmonic spherical $Fe_3O_4@Ag$ core-shell nanocomposite.

The dissertation is organized as follows: Chapter 2: In this chapter, we present the interactions of light with a homogenous metallic nanoparticles. To study the Optical/plasmonic response of the interaction, we use Models and Their Theoretical Considerations of Spherical Homogenous Nanoparticles such as Drude free-electrons model for metallic and lorentz model for semiconductor nanoparticles. The unique properties due to its increase in the surface area to volume ratio and the quantum size effect are also addressed in this chapter.

Chapter 3: This chapter is devoted to the discussion of the Optical Responses of Metal/Dielectric Core/Shell Nanoparticles. In this chapter we present the fundamental theory for surface plasmon resonance, electrostatic approximation, effective medium approximation for metal coated core/shell nanoparticles. We will discuss electric polarizability, absorption and scattering cross-sections for metal coated core/shell structured nanoparticles.

Chapter 4: This chapter presents the derivation of the effective permittivity and permeability of the theoretically modelled magnetic-semiconductor/metal core/shell spherical NP embedded in a dielectric host matrix. The numerical results are also presented and discussed in this chapter.

Chapter 5: In this chapter, we provides the discussion of the Effect of Surface Plasmonic Resonances on Magneto-Plasmonic $Fe_3O_4@Ag$ Spherical Core-Shell Nanoparticles. Based on electrostatic approximation and the Maxwell-Garnet effective medium theory, theoretical analysis have been done to derive ε_{eff} and μ_{eff}. Using these theoretically determined values, calculations have been done on the magneto-optical parameters such, as the electric polarizability, absorption and scattering cross-sections.

Chapter 6: This chapter presents a conclusion of the the results obtained in this work and and future work remarks.

Chapter 2

Models and Theoretical Considerations on the Optical Response of Plasmonic Spherical Homogenous/Hetrogenous Nanoparticles

2.1 Spherical Homogenous Nanoparticles

2.1.1 Introduction

The interaction of a particle of size a with the electromagnetic field can be analyzed using the simple quasi-static approximation provided that $a \ll \lambda$, i.e. the particle size is much smaller than the wavelength of light in the surrounding medium. In this case, the phase of the harmonically oscillating electromagnetic field is practically constant over the particle volume, so that one can calculate the spatial field distribution by assuming the simplified problem of a particle in an electrostatic field. The harmonic time dependence can then be added to the solution once the field distributions are known. As we will show below, this lowest-order approximation of the full scattering problem describes the optical properties of nanoparticles of dimensions below 100 nm adequately for many purposes. We start with the most convenient geometry for an analytical treatment: a homogeneous, isotropic sphere of radius a located at the origin in a uniform, static electric field $E = E_0\hat{z}$ (Fig. 2.1). The surrounding medium is isotropic and non-absorbing with dielectric constant ε_m, and the field lines are parallel to the z-direction at sufficient distance from the sphere. The dielectric response of the sphere is further described by the dielectric function $\varepsilon(\omega)$, which we take for the moment as a simple complex number ε.

2.2 Models for Metals and Dielectric Materials

2.2.1 Electrostatic Approximation

For a spherical nanoparticle of radius a that is irradiated by z-polarized light of wavelength λ (where a is much smaller than the wavelength of light), the magnitude of the electric field appears static around the nanoparticle, allowing us to solve the spatial field distribution (assuming as a problem of a particle in an electrostatic field). we are interested in a solution of the Laplace equation for the potential $\nabla^2\Phi = 0$, from which we will be able to calculate the electric field $E = -\nabla\Phi$. Due to the azimuthal symmetry of the problem, the general solution is of the form [26]-[28]

$$\Phi(r,\theta) = \sum_{\ell=0}^{\infty}[A_\ell r^\ell + B_\ell r^{-(\ell+1)}]P_\ell(\cos\theta), \tag{2.2.1}$$

where $P_\ell(cos\theta)$ are the Legendre Polynomials of order ℓ and θ the angle between the position vector r at point P and the z-axis (Fig. 2.1). Due to the requirement that the potentials remain finite at the origin, the solution for the potentials Φ_{in} inside

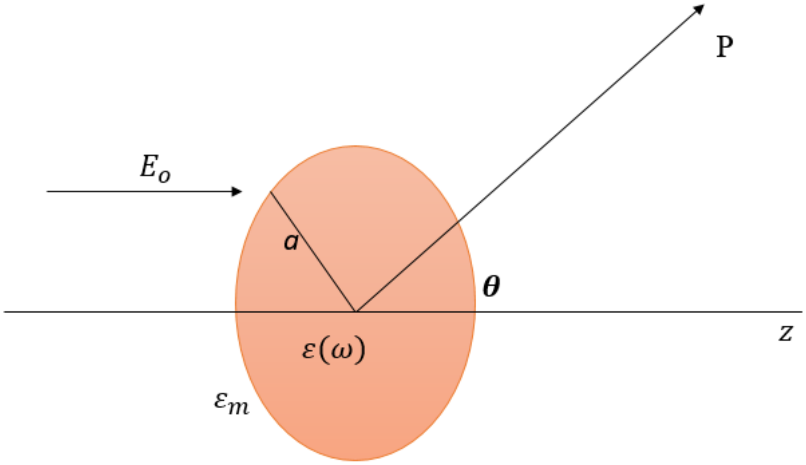

Figure 2.1: Sketch of a homogeneous sphere placed into an electrostatic field.

and Φ_{out} outside the sphere can be written as

$$\Phi_{in}(r,\theta) = \sum_{\ell=0}^{\infty} A_\ell r^\ell P_\ell(\cos\theta), \tag{2.2.2}$$

$$\Phi_{out}(r,\theta) = \sum_{\ell=0}^{\infty} [B_\ell r^\ell + C_\ell r^{-(\ell+1)}] P_\ell(\cos\theta), \tag{2.2.3}$$

The coefficients A_ℓ, B_ℓ and C_ℓ can now be determined from the boundary conditions at $r \to \infty$ and at the sphere surface $r = a$. The requirement that $\Phi_{out} \to -E_0 z = -E_0 r\cos\theta$ as $r \to \infty$ demands that $B_\ell = -E_0$ for $\ell = 1$ and $B_\ell = 0$ for $\ell \neq 1$. The remaining coefficients A_ℓ and C_ℓ are defined by the boundary conditions at $r = a$. Equality of the tangential components of the electric field demands that

$$-\frac{1}{a}\frac{\partial \Phi_{in}}{\partial \theta}|_{r=a} = -\frac{1}{a}\frac{\partial \Phi_{out}}{\partial \theta}|_{r=a}, \tag{2.2.4}$$

and the equality of the normal components of the displacement field

$$-\varepsilon_0\varepsilon\frac{\partial\Phi_{in}}{\partial r}|_{r=a} = -\varepsilon_0\varepsilon_m\frac{\partial\Phi_{out}}{\partial r}|_{r=a}, \tag{2.2.5}$$

when the series Eqns. (2.2.2) and (2.2.3) are substituted in Eqn. (2.2.5), results to Legendre functions equals to zero. Since these must vanish for all θ, the coefficient of each Legendre function must vanish separately. For the Left hand side of (2.2.5) boundary condition leads (through orthogonality of $P_\ell^1 = \partial P_\ell/\partial\theta$) to the relations

$$A_1 = -E_o + \frac{C_1}{a^3}$$

$$A_\ell = \frac{C_\ell}{a^{2\ell+1}} \quad For \ \ \ell \neq 1 \tag{2.2.6}$$

while the right hand side of Eqn. (2.2.5) gives (through orthogonality P_ℓ)

$$(\varepsilon/\varepsilon_o)A_1 = -E_o - 2\frac{C_1}{a^3}(\varepsilon/\varepsilon_o)$$

$$A_\ell = -(\ell+1)\frac{C_\ell}{a^{2\ell+1}} \quad For \ \ \ell \neq 1 \tag{2.2.7}$$

the right hand side of equations in Eqns. (2.2.6) and (2.2.7) can be satisfied simultaneously only with $A_\ell = C_\ell = 0$ for all $\ell \neq 1$. The remaining coefficients are given in terms of the applied electric field E_o.

$$A_1 = -\left(\frac{3}{2+\varepsilon/\varepsilon_o}\right)E_o$$

$$C_1 = \left(\frac{\varepsilon/\varepsilon_o - 1}{\varepsilon/\varepsilon_o + 2}\right)a^3E_o \tag{2.2.8}$$

The potential is therefore

$$\Phi_{in} = -\frac{3\varepsilon_m}{\varepsilon + 2\varepsilon_m} E_0 r \cos\theta \qquad r < a \tag{2.2.9}$$

$$\Phi_{out} = -E_0 r \cos\theta + \frac{\varepsilon - \varepsilon_m}{\varepsilon + 2\varepsilon_m} E_0 a^3 \frac{\cos\theta}{r^2} \qquad r \geq a \tag{2.2.10}$$

where Φ_{out} describes the superposition of the applied field and that of a dipole located at the particle center. We can rewrite Φ_{out} by introducing the dipole moment $\mathbf{p}$ as

$$\Phi_{out} = -E_0 r \cos\theta + \frac{\mathbf{p.r}}{4\pi\varepsilon_0\varepsilon_m r^3}, \tag{2.2.11}$$

$$\mathbf{p} = 4\pi\varepsilon_0\varepsilon_m a^3 \frac{\varepsilon - \varepsilon_m}{\varepsilon + 2\varepsilon_m} E_0. \tag{2.2.12}$$

We therefore see that the applied field induces a dipole moment inside the sphere of magnitude proportional to $|E_0|$. If we introduce the polarizability α, defined through $\mathbf{p} = \varepsilon_0\varepsilon_m \alpha E_0$, we arrive at

$$\alpha = 4\pi a^3 \frac{\varepsilon - \varepsilon_m}{\varepsilon + 2\varepsilon_m}. \tag{2.2.13}$$

Equation Eqn. (2.2.13) is the central result of this section, the (complex) polarizability of a small sphere of sub-wavelength diameter in the electrostatic approximation. We note that it shows the same functional form as the Clausius Mossotti relation. It is apparent that the polarizability experiences a resonant enhancement under the condition that $|\varepsilon + 2\varepsilon_m|$ is a minimum, which for the case of small or slowly-varying $Im[\varepsilon]$ around the resonance simplifies to

$$Re[\varepsilon(\omega)] = -2\varepsilon_m \tag{2.2.14}$$

This relationship is called the Fr$\ddot{o}$hlich [29] condition and the associated mode (in an oscillating field) the dipole surface plasmon of the metal nanoparticle. For a sphere consisting of a Drude metal with a dielectric function located in air, the Fr$\ddot{o}$hlich criterion is met at the frequency $\omega_0 = \frac{\omega_p}{\sqrt{3}}$. Eqn. (2.2.14) Further expresses the strong dependence of the resonance frequency on the dielectric environment: The resonance red-shifts as ε_m is increased. We note that the magnitude of a at resonance is limited by the incomplete vanishing of its denominator of Eqn. (2.2.14), due to $Im[\varepsilon(\omega)] \neq 0$.

The distribution of the electric field $E = -\nabla\Phi$ can be evaluated from the potentials Eqns. (2.2.9) and (2.2.10) to

$$E_{in} = \frac{3\varepsilon_m}{\varepsilon + 2\varepsilon_m} E_0, \tag{2.2.15}$$

Therefore, a spatially constant electric field of magnitude E_{in} is induced inside the sphere.

$$E_{out} = E_0 + \frac{\mathbf{3n(n.p)\text{-}p}}{4\pi\varepsilon_0\varepsilon_m}\frac{1}{r^3}, \tag{2.2.16}$$

Up to this point, we have been on the firm ground of electrostatics, which we will now leave when turning our attention to the electromagnetic fields radiated by a small particle excited at its plasmon resonance. For a small sphere with $a \ll \lambda$, its representation as an ideal dipole is valid in the quasi-static regime, i.e. allowing for time-varying fields but neglecting spatial retardation effects over the particle volume. Under plane-wave illumination with $E(r,t) = E_0 e^{-i\omega t}$, the fields induce an oscillating dipole moment $\mathbf{p}(t) = \varepsilon_0 \varepsilon_m \alpha E_0 e^{-i\omega t}$, with α given by the electrostatic result (2.2.13). The radiation of this dipole leads to scattering of the plane wave by the sphere, which can be represented as radiation by a point dipole.

These oscillating dipole fields of the well-known spherical-wave form are given by

$$\mathbf{H} = \frac{ck^2}{4\pi}\mathbf{n} \times \mathbf{p}\frac{e^{ikr}}{r} \tag{2.2.17}$$

$$\mathbf{E} = \sqrt{\frac{\mu_0}{\varepsilon_0 \varepsilon_m}}(\mathbf{H} \times \mathbf{n}) \tag{2.2.18}$$

2.2.2 The Quasi-Static Approximation

The quasi-static approximation (QSA) and Mie theory are among the well-known approaches to simulate the scattering of light in coreshell NPs. However, the QSA considerably simplifies the mathematical analysis of the scattering problem of complex geometries such as core-shell systems of dimensions below 100 nm. The QSA refers to the assumption that when a particles size is much smaller than the wavelength of the incident electromagnetic field, its electric field may be regarded as spatially uniform over the extent of the particle. Unlike the Mie approach, in QSA all multipole orders higher than the dipole are neglected, so that the electrostatic solution can be obtained by solving Laplaces equation ($\nabla^2\Phi = 0$)of the electric potential, Φ, from which we will be able to calculate the electricfield $E = -\nabla\Phi$. Here, we first calculate the potential in the different regions of the NPs, and then the polarizability and the corresponding extinctioncross-section using the QSA.

As described in the previous section, applying electrostatic theory to the problem of scattering and absorption of electromagnetic radiation by small metal spheres (radius $a \ll \lambda$) enables some understanding of the fundamental physical processes to be gained. The simplest scenario to consider a system consists of a non-magnetic ($\mu = \mu_0$) sphere surrounded by a homogeneous, linear and isotropic medium that is non-absorbing [30, 31], it is assumed that the particle initially experiences a uniformly polarised field throughout the entire volume of the sphere. Phase shifts that would exist in a non-uniform field are neglected, thus multipolar resonances predicted by Mie theory are restricted to the dipole mode [32]. The mode is induced by the movement of the electrons relative to the positively charged ion cores of the atomic nuclei under the influence of the externally applied electric field. Provided the permittivities of the sphere and the external medium are different a charge is developed at the surface resulting in a polarisation field within the particle. The external field is modified by the electromagnetic field generated by the polarisation charge [34]. Standard methods in electrostatics can be applied to derive expressions for the electric fields inside (E_1) and outside (E_2) the sphere from the scalar potentials $\phi_1(r,\theta)$ and $\phi_2(r,\theta)$ using

$$E_i = -\nabla\phi_i, \qquad i = 1, 2, \tag{2.2.19}$$

and the Laplace equation

$$\nabla\phi_i^2 = 0, \tag{2.2.20}$$

The boundary conditions at the interface (r = a) between the sphere and the medium necessitate that the potential is continuous $\phi_1 = \phi_2$ and that their radial derivatives satisfy

$$\varepsilon_1 \frac{\partial\phi_1}{\partial r} = \varepsilon_2 \frac{\phi_2}{\partial r}, \tag{2.2.21}$$

where ε_1 is the complex permittivity of the particle and ε_2 is the permittivity of the external medium. A further condition is that far from the particle the field is unperturbed by the particle

$$E_2 = E_0(r \rightarrow \infty), \tag{2.2.22}$$

$$\phi_2 = -E_0 z = -E_0 r cos(\theta), \tag{2.2.23}$$

and is equal to the incident field now defined as $E_0 = E_0 z$. Solving Eqn. (2.2.20) and applying the boundary conditions yields the following expressions for the potential inside ϕ_1 and outside ϕ_2 the sphere,

$$\phi_1 = \frac{3\varepsilon_2}{\varepsilon_1 + 2\varepsilon_2} E_0 r \cos(\theta), \tag{2.2.24}$$

$$\phi_2 = -E_0 r cos(\theta) + a^3 E_0 \frac{\varepsilon_1 - \varepsilon_2}{\varepsilon_1 + 2\varepsilon_2} \frac{\cos(\theta)}{r^2}, \tag{2.2.25}$$

Instantly one can see by comparison Eqn. (2.2.25) with Eqn. (2.2.23) that the field outside of the sphere is a superposition of the incident field and the field generated by the particle. By comparison with the equation for the potential due to an ideal dipole

$$\phi = \frac{p \cdot r}{4\pi\varepsilon_2 r^3} = \frac{p}{4\pi\varepsilon_2} \frac{\cos(\theta)}{r^2}, \tag{2.2.26}$$

where p is the dipole moment, the second term in Eq. (2.2.25) is identified as being that of an ideal dipole with moment

$$P = 4\pi a^3 \frac{\varepsilon_1 - \varepsilon_2}{\varepsilon_1 + 2\varepsilon_2} \varepsilon_2 E_0 \tag{2.2.27}$$

and polarizability α,

$$\alpha = 4\pi a^3 \frac{\varepsilon_1 - \varepsilon_2}{\varepsilon_1 + 2\varepsilon_2} \tag{2.2.28}$$

The derivation above has required a spatially constant electric field and has neglected the application of a time-varying electric field. An electromagnetic wave incident on a sphere as defined above naturally has a time-varying electric field and therefore when applying electrostatic theory to these situations is often referred to as the quasi-static approximation. This acknowledges that although spatially invariant at an instant in time, the particle experiences a field with a time dependent phase. The polarisability is related to the absorption and scattering cross-sections given by [33]

$$C_{sca} = \frac{k^4}{6\pi}|\alpha^2|, \tag{2.2.29}$$

$$C_{abs} = kIm\{\alpha\}, \tag{2.2.30}$$

yielding, upon substitution of the polarisability in equation 2.2.28

$$C_{sca} = \pi a^2 \frac{8}{3} x^4 |(\frac{\varepsilon_1 - \varepsilon_2}{\varepsilon_1 + 2\varepsilon_2})^2|, \tag{2.2.31}$$

$$C_{abs} = \pi a^2 4x Im\{\frac{\varepsilon_1 - \varepsilon_2}{\varepsilon_1 + 2\varepsilon_2}\} \tag{2.2.32}$$

where $x = ka = \frac{2\pi a n_2}{\lambda}$ is the size parameter. From these relations it is clear how the absorption, scattering and extinction from a particle small compared to the wavelength depend on the size, wavelength and relative permittivities of the particle and the external medium. For a small particle consisting of a material with a dielectric function only weakly dependent on the frequency of the incident radiation and satisfying the conditions above the absorption is proportional to $\frac{1}{\lambda}$ and the scattering intensity proportional to $\frac{1}{\lambda^4}$. This is known as Rayleigh scattering after Lord Rayleigh who used the relationship to explain the color of a clear blue sky in 1871.

2.3 Optical Response of Metallic Nanoparticles

2.3.1 Mie Theory

The exact analytical description of the optical behavior of metallic nanoparticles can be calculated by solving Maxwells equations. In 1908, Gustav Mie solved the Maxwell equations for the electromagnetic wave interacting with a small sphere. The theory shows the importance of multipole oscillations for the extinction cross section as the particle grows larger. In the Mie theory, the scattering and extinction cross sections are calculated by [35]:

$$C_{ext} = \frac{2\pi}{|k|^2} \sum_{L=1}^{\infty} (2L+1) Re(a_L + b_L), \tag{2.3.1}$$

$$C_{sca} = \frac{2\pi}{|k|^2} \sum_{L=1}^{\infty} (2L+1)(|a_L|^2 + |b_L|^2), \tag{2.3.2}$$

with

$$a_L = \frac{m\psi_L(mx)\psi'_L(x) - \psi'_L(mx)\psi_L(x)}{m\psi_L(mx)\eta'_L(x) - \psi'_L(mx)\eta_L(x)} \tag{2.3.3}$$

$$b_L = \frac{\psi_L(mx)\psi'_L(x) - m\psi'_L(mx)\psi_L(x)}{\psi_L(mx)\eta'_L(x) - m\psi'_L(mx)\eta_L(x)} \tag{2.3.4}$$

$m = n/n_m$, where n is the complex index of refraction of the metal particle, n_m is the real index of refraction of the surrounding medium, k is the wave vector, $x = |k|r$, ψ_L

and η_L are the Ricatti-Bessel cylindrical functions, L is the summation index of the partial waves ($L = 1$ corresponds to the dipole oscillation, $L = 2$ is associated with the quadrupole oscillation, and so on), and the prime indicates differentiation with respect to the argument in the parentheses.

For a sphere with volume V the dipolar contribution of extinction cross section $C_{ext} = C_{abs} + C_{sca}$ can be presented as:

$$C_{ext} = 9\frac{\omega}{c}\varepsilon_h^{3/2} V \frac{\varepsilon_m^{''}}{(\varepsilon_m' + 2\varepsilon_h)^2 + \varepsilon_m^{''2}} \tag{2.3.5}$$

where ε_h is the dielectric function of the embedding medium, and $\varepsilon_m = \varepsilon_m^{'} + i\varepsilon_m^{''}$ is the dielectric function of the particle, c is the speed of light.

For non-absorbing host matrix, the approximate resonance behavior of Eq. (2.3.5) is computed from the condition called the Frohlich condition for which the denominator of Eq. (2.3.5) is minimum, [36] i.e.,

$$(\varepsilon_m^{'} + 2\varepsilon_h)^2 + (\varepsilon_m^{''})^2 = Minimum. \tag{2.3.6}$$

For $\varepsilon^{''}$ is small or slowly-varying with ω, which is the case for noble metals, $\varepsilon_m^{'} = -2\varepsilon_h$. This condition points to the use of plasmonic metal, where ε_m can be negative; additionally, the imaginary part of ε_m should be as small as possible [37]. It turns out that this condition corresponds to the excitation of a surface plasmon in the metallic nanoparticle [38]. Substituting the resonance condition for the extinction cross section into the real part of the dielectric function for the free electron contribution yields the following approximation for the maximum of the extinction cross section in the limit where $\gamma \ll \omega$.

$$\omega_s = \frac{\omega_p}{\sqrt{\varepsilon_\infty + 2\varepsilon_h}}. \tag{2.3.7}$$

This frequency is called the local surface plasmon (LSP) frequency, Eq. (2.3.7) indicates that the LSP frequency depends on the dielectric constant of the matrix in which we place the metal nanoparticle, and the type of metal that we use for excitation of LSP resonance. Moreover, Eq. (2.3.7) shows that the plasmon peak of a metallic NP will appear at a lower energy than the bulk plasmon of the same material.

2.3.2 Lorentz Model

A plasma model is used to describe the optical properties of metals due to the free electron movement of the conduction electrons through a fixed positive, ionic background. The model was developed by H. A. Lorentz as a classical approach to describe optical properties of materials by assuming that electrons and ions of a medium are simple harmonic oscillators and neglecting material properties such as the lattice potential and electron-electron interactions. The simple oscillator model is of great use in determining optical properties of a material because it can describe a variety of optical excitations [39]-[43]. The microscopic model of a polarizable material becomes a macroscopic system of independent, isotropic, and identical harmonic oscillators which are subjected to an applied electric field, E, which acts as a driving force. The oscillation response to an applied local electric field, E_{local}, for an electron with an effective mass, m, and a charge, e, is given by

$$m\frac{d^2x}{dt^2} + m\gamma\frac{dx}{dt} + Kx = eE_{loc}; \tag{2.3.8}$$

where x is the distance displaced from equilibrium, Kx is the restoring force for an electron with a spring constant, K. The oscillation of electrons is damped as a result of collisions, which adds a damping term to the equation, $m\gamma$, where the collision frequency, $\gamma = 1/\tau$, and τ is the relaxation time for a free electron plasma which at room temperature is typically on the order of 10^{-14} making $\tau = 100$ THz. Since the electric field has a harmonic time dependence [44],

$$E(t) = E_0 e^{-i\omega t} \tag{2.3.9}$$

with a frequency, ω, and time, t, the solution to the equation for an electron becomes

$$x(t) = x_0 e^{-i\omega t}, \tag{2.3.10}$$

where phase shifts between the driving force of the electric field and the electron response is contained in the complex amplitude, x_0 [45]. The oscillatory solution to Eqn. (2.3.8) becomes:

$$x(t) = E(t)\frac{e}{m(\omega_0^2 - \omega^2 - i\gamma\omega)}, \tag{2.3.11}$$

with $\omega_0^2 = K/m$. A schematic of a Lorentz harmonic is shown in Fig. (2.2(A)). In most systems, there is a certain degree of collisions that occur which means $\gamma = 0$ and the phase of the driving field and oscillating electrons have a displacement, D,

$$D = Ae^{(i\theta)}(\frac{eE}{m}), \tag{2.3.12}$$

with phase angle, θ,

$$\theta = \tan^{-1}[\frac{\omega\gamma}{\omega_0^2 - \omega^2}], \tag{2.3.13}$$

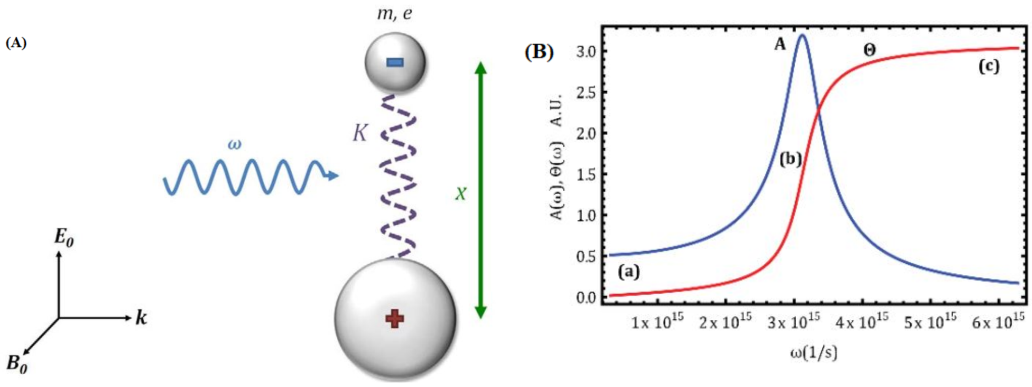

Figure 2.2: Lorentz harmonic oscillator [45, 46].

and amplitude, A,

$$A = \tan^{-1}\left[\frac{1}{[(\omega_0^2 - \omega^2)^2 + \omega^2\gamma^2]^{1/2}}\right]; \tag{2.3.14}$$

The consequence of the phase difference results in the maximum amplitude occurring when the frequencies $\omega_0 \cong \omega$. If $\gamma \ll \omega_0$, the height of the maximum amplitude is inversely proportional to γ and the full width at half maximum (FWHM) is proportional to γ. Fig.(2.2(B)) shows a plot for the amplitude and phase relation for a hypothetical oscillator. At low frequencies, the oscillator response is in phase with the driving force where $\theta \cong 0$ and $\omega \ll \omega_0$ as shown in Fig. (2.2 (B)). At the resonance frequency, the amplitude is at a maximum and the phase lag is $\theta = 90^0$. Near ω_0 a 180^0 phase change occurs. As a result, at high frequencies, $\omega \gg \omega_0$ the oscillator response and the driving force are 180^0 out of phase.

For a single oscillator, the induced dipole moment is $p = ex$. For a large number of oscillators, n, the dipole moment per unit volume becomes,

$$P = -nex; \tag{2.3.15}$$

and when combined with Eqn. 2.3.11 becomes

$$P = \frac{\omega_p^2}{\omega_0^2 - \omega^2 - i\omega\gamma} E\varepsilon_0, \tag{2.3.16}$$

where the plasma frequency, is given by

$$\omega_p^2 = \frac{ne^2}{\varepsilon_0 m}, \tag{2.3.17}$$

The optical constants for the collection of oscillators can then be derived out, where the dielectric function for the bulk material is given by

$$\varepsilon(\omega) = 1 + \chi = 1 + \frac{\omega_p^2}{\omega_0^2 - \omega^2 - i\omega\gamma}, \tag{2.3.18}$$

which can be decomposed into the real, ε_1, and imaginary, ε_2, components of the complex dielectric function, $\varepsilon(\omega) = \varepsilon_1(\omega) + i\varepsilon_2(\omega)$ as

$$\varepsilon_1(\omega) = 1 + \chi^{'} = 1 + \frac{\omega_p^2(\omega_0^2 - \omega^2)}{(\omega_0^2 - \omega^2)^2 + \omega^2\gamma^2}, \tag{2.3.19}$$

$$\varepsilon_2(\omega) = \chi^{''} = \frac{\omega_p^2\omega\gamma}{(\omega_0^2 - \omega^2)^2 + \omega^2\gamma^2}, \tag{2.3.20}$$

At the natural frequency ω_0, the imaginary part of the dielectric constant is at a maximum as shown in Fig. 2.3 for silver

2.3.3 Drude Model

Consider a system where the conduction electrons of metals are treated as a gas of free electrons, the conduction and valence band overlap allowing for electrons near the Fermi level to be excited to different energy and momentum states by the absorption of photons with very little energy [35], [36], [47]. These intraband transitions give rise to free electrons which can be taken into account by modification of the Lorentz model. When the spring constant in Eq.(2.3.8) is set to zero, it essentially clips the springs of the harmonic oscillators with $K = 0$ and $\omega_0 = 0$ to transform Eq.(2.3.11) into

$$x(t) = E(t)\frac{e}{m(\omega^2 + i\gamma\omega)}, \tag{2.3.21}$$

When the polarization in Eqn. (2.3.15) is combined with equation Eqn. (2.3.21), it

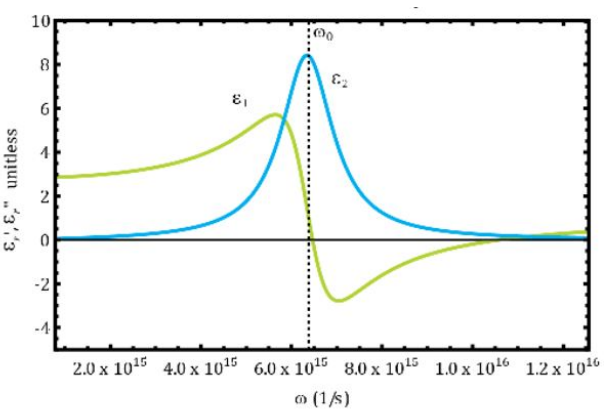

Figure 2.3: Frequency dependence of the real and imaginary parts of the dielectric constant of silver [46].

becomes

$$P = -n\frac{e^2}{m(\omega^2 + i\omega\gamma)}E, \tag{2.3.22}$$

gives the relation between D and E in terms of frequency and electric permittivity as

$$D = \varepsilon_0(1 - \frac{\omega_p^2}{\omega^2 + i\gamma\omega})E, \tag{2.3.23}$$

The new dielectric function for the free electrons becomes

$$\varepsilon(\omega) = 1 - \frac{\omega_p^2}{\omega^2 + i\gamma\omega}, \tag{2.3.24}$$

which can be decomposed into the real, ε_1, and imaginary, ε_2 of the complex dielectric function as

$$\varepsilon_1(\omega) = 1 - \frac{\omega_p^2}{\omega^2 + \gamma^2}, \tag{2.3.25}$$

$$\varepsilon_2(\omega) = \frac{\omega_p^2\gamma}{\omega(\omega^2 + \gamma^2)}, \tag{2.3.26}$$

Eqn. (2.3.24) demonstrates that the dielectric constant can become zero near the plasma frequency where the material can support collective modes of oscillating electrons in phase with each other. By tuning the geometry of the structure, the oscillation can occur at negative values of the dielectric constant.

2.3.4 Size Effects

Nanomaterials have unique properties due to its increase in the surface area to volume ratio and the quantum size effect. If the size of nanocomposite materials is smaller than their De-Broglie wavelength of electrons and holes are spatially confined, creating electric dipoles. Nano-sized materials have a probability of significant interface interaction, which strongly determines the properties like electrical resistivity, chemical reactivity, adhesion, and catalytic activity. For instance, for very small metallic nanoparticles, the plasmonic properties are dependent on the radius r. From Drude-Sommerfeld Theory, the bulk plasmon frequency, ω_p, is defined as, $\omega_p = \sqrt{ne^2/\varepsilon_0 m_e}$ with e, m_e, and n being the charge, mass and total number of conduction electrons in the metal, respectively and ε_0 is the permittivity of free space. To incorporate both, size dependent conduction electron processes and interband transitions to the polarizability, ε_m can be described by introducing the high frequency dielectric function ε_∞.

$$\varepsilon_m(\omega) = \varepsilon_\infty - \frac{\omega_p^2}{\omega(\omega + i\gamma)} \tag{2.3.27}$$

The dielectric function Eq. (2.3.27) is dependent on the size of the material, and defined as [35, 48];

$$\varepsilon(\omega, r) = \varepsilon_\infty - \frac{\omega_p^2}{\omega(\omega + i\gamma(r))}. \tag{2.3.28}$$

The size dependent damping parameter can be expressed as;

$$\gamma(r) = \gamma_0 + A\frac{V_f}{r}, \tag{2.3.29}$$

where γ_0 is the bulk damping constant, V_f is the speed of electrons at Fermi energy surface and A is a parameter that depends on the specifics of the scattering process. The size dependent damping parameter highly determine the sharpness and broadness of optical absorbance of metallic nanoparticles as well as nanocomposite.

2.4 The Optical Response of Metal/Dielectric (Heterogenous) Core/Shell Nanoparticles

In this section, we present the fundamental theory for surface plasmon resonance, localized surface plasmon resonance (LSPR), Electrostatic Approximation, Effective medium Approximation for metal coated core/shell nanoparticles. In addition, we will derive the equations of electric potential inside and outside of the naoparticles which have spherical symmetry, as well as the electric field distribution inside the core/shell nanoparticles. Then, employing the calculated parameters, we will discuss electric Polarizability, refractive index, absorbance and extinctioon cross-sections for metal coated core/shell structured nanoparticles.

2.5 Plasmon Resonance in Noble Metal Nanostructures

Plasmons arise from the collective oscillations of free electrons in metallic materials. Under the irradiation of an electromagnetic wave, the free electrons are driven by the electric field to coherently oscillate at a plasmon frequency of ω_B relative to the lattice of positive ions. For a bulk metal with infinite sizes in three dimensions in vacuum, ω_B can be expressed as

$$\omega_B = \sqrt{\frac{4\pi e^2 n}{m_e}}; \tag{2.5.1}$$

where n is the number density of electrons and e and me are the charge and effective mass of electrons, respectively.

However, in reality, we have to deal with metallic structures of finite dimensions

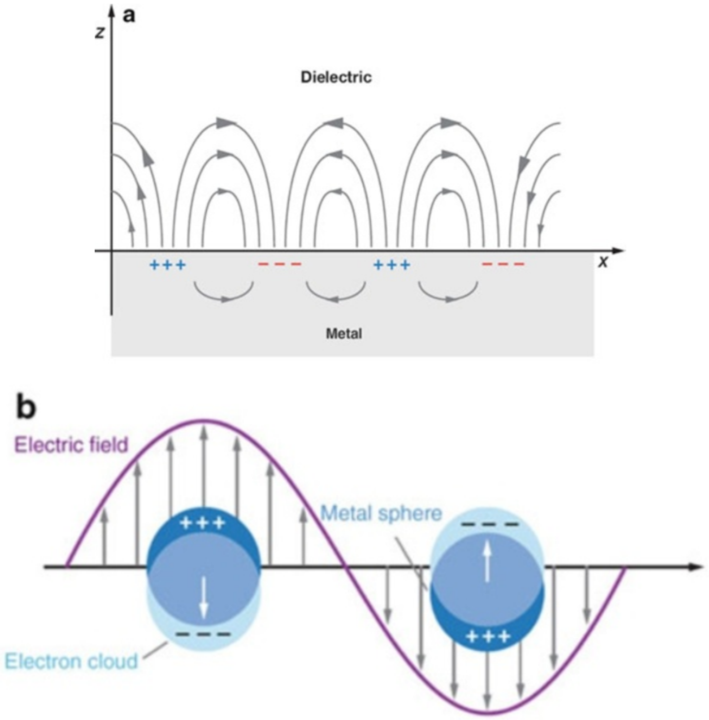

Figure 2.4: Schematic illustrations of (a) a propagating plasmon at metaldielectric interface and (b) a LSPR of a metal nanosphere,[49].

that are surrounded by materials with different dielectric properties. Since an electromagnetic wave impinging on a metal surface only has a certain penetration depth (~ 50 nm for Ag and Au), only the electrons on the surface are the most significant. Therefore, their collective oscillations are properly termed as surface plasmons. At a metalvacuum interface, application of the boundary conditions results in a surface plasmon mode with a frequency $\omega_{surf} = \frac{\omega_B}{\sqrt{2}}$. As is shown in Fig.2.4, such a surface plasmon mode represents a longitudinal charge density wave that travels across the surface, also widely known as a propagating plasmon. A surface plasmon mode can be excited through a resonance mechanism by passing an electron through a thin metallic film or by reflecting an electron or a photon from the surface of a metallic film when the frequency and wave vectors of both the incident light and the surface plasmon match each other. In metallic nanoparticle systems, the collective oscillations of free electrons are confined to a finite volume defined by the particle dimensions. Since the plasmons of nanoparticles are localized rather than propagating, they are known as localized surface plasmon resonances (LSPRs). When the free electrons in a metallic nanostructure are driven by the incident electric field to collectively oscillate at a certain resonant frequency, the incident light is absorbed by the nanoparticles. Some of these photons will be released with the same frequency and energy in all directions which is known as the process of scattering. Meanwhile, some of these photons will be converted into phonons or vibrations of the lattice, which is referred to as absorption. Therefore, LSPRs manifest themselves as a combined effect of scattering and absorption in the optical extinction spectra [49].

The excitation of surface plasmons at rough noble-metal surfaces is responsible for the enhancement of several optical phenomena observed for nanoparticles adjacent to these surfaces, metal nanoparticles were considered as surface plasmon-assisted field amplifiers. However, these particles can also be exploited as intrinsic refractive index sensors. The physical basis of this application is the light extinction (absorption and scattering), which is heavily dependent on the nanoparticles dielectric constant, size and geometry and also on the dielectric constant of the surrounding medium [50].

The interesting optical attributes of metal nanoparticles, as reflected in their bright intense colors, are due to their unique interaction with light. In the presence of the oscillating electromagnetic field of the light, the free electrons of the metal nanoparticle undergo a collective coherent oscillation with respect to the positive metallic lattice. This process is resonant at a particular frequency of the light and is termed the localized surface plasmon resonance (LSPR) oscillation. This electronic oscillation can be simply visualized as a photon confined to the small size of the nanostructure, constituting an intense electric field around the particle. The surface plasmon oscillation decays by radiating its energy resulting in light scattering or decays nonradiatively as a result of conversion of absorbed light to heat. The electric field intensity and the scattering and absorption cross-sections are all strongly enhanced at the LSPR frequency, which for gold, silver, and copper lies in the visible region. Since copper is easily oxidized, gold and silver nanostructures are most attractive for optical applications. Nanosized dimensions of the nanoparticle probes make it easy to incorporate them into biological systems, which are on the same size scale [51]. The localized surface plasmon resonance is the result of the confinement of surface plasmon in the nanoparticle of a size comparable to or smaller than the wavelength of light used to excite the plasmon. Localized surface plasmon has two effects, i) the electric fields near the particle surface are greatly enhanced, which falls-off quickly with distance from the surface. ii) The optical extinction of nanoparticles is the maximum at the surface plasmon resonant frequency and this occurs at a visible wavelength for the noble metal nanoparticles, which enhances their applications in various fields. Plasmon resonant frequency is highly sensitive to the index of refraction of the environment. This allows nanoparticles possessing localized surface plasmon to be used for nanoscale sensing application. Nanostructures exhibiting localized surface plasmon resonances are used to enhance the optical signals in modern analytical techniques based on spectroscopy. The plasmon resonance can either radiate (Mie scattering) light, which is useful in optical and imaging fields or is converted into heat(absorption) which has opened up applications in several areas. Nanoparticles with SPR has the ability to integrate metal nanoparticles into the biological systems to have live fluorescence imaging and thus contributes much into the area of biology and biomedicine [19]. Metal nanoparticles can be conjugated with small molecule or biomolecular targeting or recognition ligands for achieving molecular specificity. While the use of photo absorbing and fluorescent dyes as biological labels and stains has been common over the last few decades, metal nanoparticles are fast replacing them as optical labels and probes. Because of surface plasmon enhancement, optical cross-sections of metal nanoparticles ($10 - 100$ nm) are 5 orders of magnitude or more larger than those of dye molecules. Each metal nanoparticle can be considered an optical probe equivalent to up to a million dye molecules. This provides a large margin for enhancing the probing sensitivity. Unlike dyes, metal nanoparticles are photostable and do not undergo photo bleaching, allowing higher light excitation energies and longer probing times. There is a range of enhanced radiative and nonradiative attributes associated with the LSPR. The optical probing strategy can thus be chosen depending on the specific biological application. Different strategies may also be combined. Another unique property of LSPR is that it can be tuned by changing the nanostructure size, shape, composition, or environment, in order to suit the bio-application [51].

In the last two decades, surface plasmon resonance (SPR) has evolved from a fairly esoteric physical phenomenon to an optical tool that is widely used in physical, chemical and biological investigations where the characterization of an interface is of interest. Recently, the field of SPR nano-optics has been added where metallic structures on a nanoscale can be designed such that they can perform certain optical functions. Essential for the generation of surface plasmons (SPs) is the presence of free electrons at the interface of two materials in practice this almost always implies that one of these materials is a metal where free conduction electrons are abundant. This condition follows naturally from the analysis of a metal/dielectric interface by Maxwells equations. From this analysis, the picture emerges that surface plasmons can be considered as propagating electron density waves occurring at the interface between metal and dielectric. Alternatively, surface plasmons can be viewed as electromagnetic waves strongly bound to this interface; it is found that the surface plasmon field intensity at the interface can be made very high, which is the main reason why SPR is such a powerful tool for many types of interface studies. Surface plasmon resonance (SPR) typically arises in nanostructures of noble metals. Their unique properties such as strong field confinement, resonant behavior and local field enhancement effects make them ideal candidates to control the emission of luminescent nanoparticles (NPs). Among these NPs, quantum dots (QDs) are highly versatile and suitable for a wide range of applications, due to their single optical properties and tunable emission, as well as high quantum yield (QY) and photostability, making them good energy donors and acceptors [52]-[54]. The interaction of light with a metal surface results in the collective oscillation of the surface free electrons. This phenomenon is called surface plasmon resonance (SPR). The noble metal components of nanoalloys have been widely used as efficient probes for localized surface plasmon resonance (LSPR), due to their strongly enhanced resonance at optical frequencies, making them excellent scatterers and absorbers in the visible spectral range. Their surface chemistry provides possibilities for functionalising with biomolecules, whilst retaining their bioactivity, which is particularly attractive for plasmonic sensing. The optical properties arise from different characteristics; higher scattering and extinction cross-sections, than the alternative semiconductor quantum dots or organic fluorophores. They have the advantages that they do not photobleach or blink, and that the surface plasmon resonance wavelength (λ_{spr}) is highly sensitive to the local dielectric environment. The physical requirements for good plasmonic responses and in particular, narrow resonance bands in bimetallic systems include the formation of a monodisperse collection of particles with a plasmonic layer of even thickness or the formation of sub-domains of the same size [55].

The quantitative understanding of the plasmonic nature of metallic nanostructures has led to the design of highly sensitive nano-antennas by the proper selection of materials along with the optimization of size, shape anisotropy and surface chemistry of the structures. However, their performance relies on the excitation of the localized surface plasmon resonance (LSPR) that is able to alter, confine, and reinforce light-matter interaction. Plasmonic nanostructures have met with tremendous successes in nanoelectronic, chemistry biology, catalysis and electro-catalysis and in biomedical fields. Then, metal dielectric coreshell structures had been successfully introduced to passivate the surface and to tune the surface plasmon resonance wavelength. More recently, bimetal coreshell structures have also attracted attention. The appeal of bimetal coreshell structures is mainly due to the evolution of new optical and physical properties including new plasmonic resonances. In particular, these nanoparticles exhibit a remarkable sensitivity of the resonance wavelength as a function of ambient refractive index, a prerequisite for high tunability. This was well reviewed elsewhere for a silver core and a gold shell geometry. The properties of surface plasmon depends on the overall geometry including the thickness of the shell, the shape anisotropy and the distance of separation between a dimer of coreshell nanospheres. The separation also considered for aggregated or overlapping nanospheres, which are nothing but negative separation distance. Gold and silver remain the strongest contenders for LSPR experiments as they provide a high density of electrons and low losses in the relevant spectral range of interest. The local electromagnetic field near the surface of a plasmonic nanostructure (nanoantenna) can exceed that of the incoming field by several orders of magnitude. The field enhancement has been proven critical in a wide range of applications like in surface enhanced Raman scattering or tip-enhanced Raman spectroscopy. On the theoretical side, better understanding and prediction of properties, whereas on the experimental side custom made exact geometry by improving the growth control and size dispersion of these nanospheres. This study therefore discusses the sensitivity of certain optical parameters, in particular the sensitivity of the plasmon resonance wavelength on the coreshell geometry and ambient refractive index. Therefore, we suggest a model of separated and overlapping Ag cores/Au shells to investigate absorption cross-section, LSPR sensitivity and tunability, the impact of shell thickness on the optical tunability by the variation of shell thickness for constant external radius and a constant shell thickness with variable external radius of the nanoparticles [56].

An electromagnetic wave propagating through different media is affected by interactions with each medium as it traverses across the boundary between one medium and another. The two main interactions between incident light and a discrete particle are absorption and scattering. Scattering can be inelastic, where the wavelength of the scattered radiation is different from the incident wavelength, or elastic, where the scattered radiation has the same wavelength as the incident light. Examples of elastic scattering are Rayleigh scattering from small, dielectric (nonabsorbing) spherical particles and Mie scattering from spherical particles with no limitations on size or dielectric properties [57]-[63]. The discussion on electromagnetic waves has been limited to the propagation of waves and interactions with simple structures composed of arbitrary media. In the following section, two different models for describing metals will be discussed: the Lorentz model and the Drude model. Both models approximately describe the optical properties of metallic structures and the plasmonic properties that arise when the structures have dimensions on the order of nanometers. Specifically, the manifestation of surface plasmons in bulk metals, discrete particles, and metal/dielectric will be discussed. The section will conclude with a brief description of different models and theories of light scattering and absorption [64]-[69].

2.6 Spherical Core/Shell Nanoparticle

Metal coated NPs with sizes much smaller than the wavelength of light show strong dipolar excitations in the form of localized surface plasmon resonances (LSPR). The term local surface plasmon resonance is used to demonstrate the resonance in a coherent oscillation of the surface conduction electrons of particles much smaller than the incident wavelength of electromagnetic radiation. The collective charge oscillation causes a large resonant enhancement of the local field inside and near the NP. For gold and silver NPs, the resonance falls into the visible region of the electromagnetic spectrum.

The analytical solution for electromagnetic response of core/shell NPs whose sizes are much smaller than the wavelength of radiation in relation to the local field distribution can be found by solving the Laplace equation. Efforts have been made to improve the applicability and stability of composite systems, by combining different types of NPs.

Consider a spherical core/shell NP coated with metal having radius r_2 subjected to an EM radiation. In electrostatic approximation at which the wavelength of radiation is much larger than the size of NP, the analytical solution for electrostatic potential ϕ inside and outside the sphere is obtained by solving the Laplace equation for spherical symmetry, i.e.,$\nabla^2\phi = 0$. As it has been reported by [70], the resulting general solution for the EM field inside and outside the core sell nanoparticle (see Fig 2.5) is in the same analogy of Eqns. (2.2.1, 2.2.2 and 2.2.3). Eqn. (2.2.1) provides a very good estimate for the optical response of small particles. However, as the particles size becomes larger, higher order responses like the quadruple response becomes significant and have to be incorporated into the calculations for the electrostatic potential. Linear combinations of the functions in the first and the second term of Eqn. (2.2.1) may have to be chosen according to the particular problem to avoid infinities at the origin or at infinite distance. Writing the complex dielectric function of the metal coat as $\varepsilon_m = \varepsilon_m^{'} + i\varepsilon_m^{''}$, where $\varepsilon_m^{'}$ and $\varepsilon_m^{''}$ are its real and imaginary parts of the dielectric function.

2.7 Effective-Medium Approximation

Heterogeneous materials offer versatile optical properties that are of use in many applications. Heterogeneous materials containing nanoscatterers (e.g., nanoparticles) as constituents have found applications in antireflection coatings, thermal metamaterials

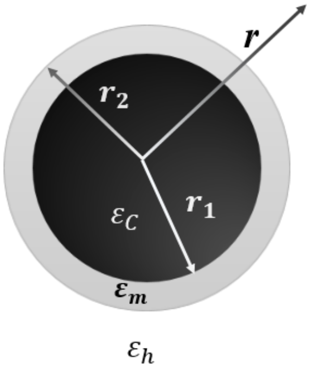

Figure 2.5: Schematic of a core-shell spherical NPs embedded in a matrix.

, all-dielectric metamaterials, among others. The optical properties of such materials can be tuned by changing the size, shape, and optical parameters of the constituent nanoparticles. This versatility also poses a design challenge in predicting the behavior of the material from the optical properties of the constituents. One way of performing such a prediction is the direct solution of the Maxwell equation as a many body problem. On the other hand, effective medium approximations (EMAs) offer a simpler path. While the former offers accuracy at a great computational expense, EMAs often offer greater physical insight. EMAs treat the heterogeneous medium as a homogeneous medium with effective optical properties that are functions of the constituent properties. Among the various linear EMAs are the series model and the parallel model, which predict effective optical parameters as series and parallel combinations of the constituent materials, respectively. A more rigorous EMA is achieved by applying the volume averaging theory to the Maxwell equation. The Maxwell-Garnett (MG) theory models the effective dielectric constant of a medium consisting of noninteracting spheres in a matrix. Bruggeman proposed another EMA that produces the same effective parameter regardless of which constituents are assumed to the matrix and inclusion, respectively. MG theory has been used most often to estimate effective optical parameters of heterogeneous materials due to its simplicity, even though the MG formula cannot account for finite-sized inclusions and interactions between them. Attempts have been made to address some of these shortcomings using the Mie solution without accounting for interactions between the inhomogeneous inclusions. Analytical treatments can be found for specific periodic cases by expanding the refractive index into a power series. Analytical formulas have been derived using the coherent scattering approach and by calculating the electrodynamic response. However, a simple analytical EMA formula capable of accounting for finite-sized, randomly arranged inclusions and the interactions between them has not been found. In this work, we have derived a simplified and fully analytical EMA that accounts for the Rayleigh scattering using the Mie solutions. The simplification is achieved by treating the Rayleigh scattering as a special case of the Mie scattering. The interaction between inclusions has been incorporated using net polarizability. The derived EMAs are compared with other EMAs as well as experimental results [71].

The effective-medium approximation (EMA) is a method of treating a macroscopically inhomogeneous medium, i.e., a medium in which quantities such as the conductivity, dielectric function, or elastic modulus vary in space. Many materials fall into this broad category [72]-[74]. One example is a metal/dielectric composite, consisting of a collection of metallic and dielectric grains arranged in some ordered or random fashion. Another example is a porous rock. If that rock is filled with salt water, then it is also a composite of an electrical insulator (the rock matrix) and an electrical conductor (the salt water). An anisotropic material sample in polycrystalline form is a third example. With a distinct conductivity or dielectric tensor, every grain within that polycrystal is essentially a new material. Since each grain has a unique fourth rank tensor, the identical problem is more complex with polycrystalline elastic materials. Since the early 1800s, there has been discussion on quantitative models for heterogeneous material qualities. As discussed in multiple studies, this sustained attention has resulted in the presentation of a multitude of successful medium formulations, either merely phenomenological or grounded in reasonably strong theories. Because metal-dielectric combinations are crucial for the effective photothermal conversion of solar energy, there has been a sharp increase in interest in their optical properties in recent years. Two effective medium theories have become particularly popular; these are usually ascribed to Garnett (known as the Maxwell-Garnett theory) and to Bruggeman [75]-[77]. The differences between the mathematical structures of the two theories have been known for some years, but a more intuitive physical understanding for the circumstances under which the two formulations apply is only presently emerging. All these EMA calculations are particularly appropriate for composites and polycrystals in which the grains of the various components are randomly and symmetrically distributed, so that none of the components is identifiable as a host in which the others are preferentially embedded [69, 78].

2.7.1 Maxwell-Garnet Theory

Maxwell Garnett EMT allows the calculation of the effective dielectric function of the host matrix with metal-semiconductor NPs inclusions taking as inputs the dielectric function of both the host and the inclusions. The new proposed approach is used to calculate the effective dielectric function of the core-shell inclusions ε_{CS} as illustrated in Figure 2.6. Then, the problem is reduced to the one of a matrix with spherical inclusions randomly distributed. This system is commonly solved by applying Maxwell Garnett EMT or equivalent EMTs; taking as input the effective dielectric function of the core-shell ε_{CS} and the host matrix ε_h, the effective dielectric function of the whole system ε_{eff} is calculated. Therefore, the initial system (i.e., host material with core-shell inclusions) is reduced to a homogeneous medium with dielectric function ε_{eff} [79]. The Maxwell Garnett theory considers the case of inclusions randomly spread in a continuous matrix. This theory is based on the Clausius Mossotti relation, which relates the polarizability (α) with the dielectric function (ε). The effective dielectric

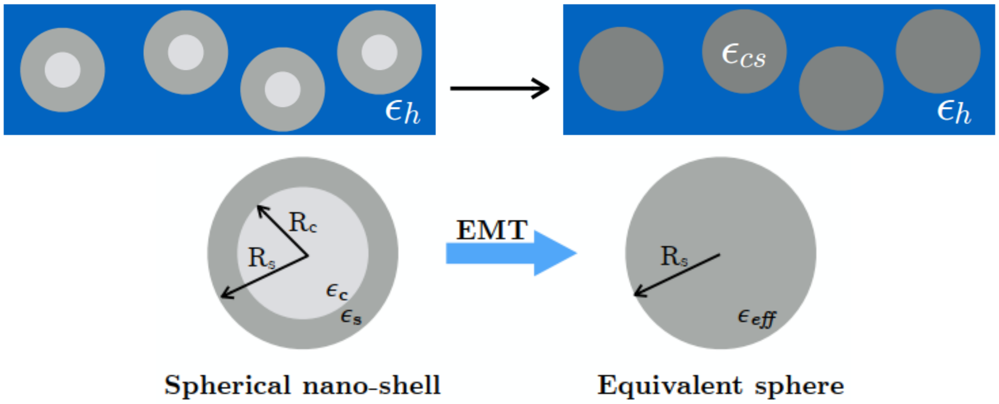

Figure 2.6: Scheme of the effective medium of composite with spherical core-shell type inclusions: the system formed by a composite with core-shell inclusions can be reduced to that of a composite with homogeneous spheres with effective dielectric function ε_{CS}. The value of ε_{CS} is obtained by applying an effective medium theory on the core-shell inclusion, to calculate its effective dielectric function ε_{eff}[79].

function of a suspension of small spheres in a host material is given by

$$\frac{\varepsilon_{eff} - \varepsilon_h}{\varepsilon_{eff} + 2\varepsilon_h} = f\frac{\varepsilon_I - \varepsilon_h}{\varepsilon_I + 2\varepsilon_h}. \tag{2.7.1}$$

where ε_h and ε_I are the dielectric functions of host and inclusions materials, and f is the volume fraction of the embedded particles. Because a core-shell nanoparticle can be considered as an inclusion (core with dielectric function ε_C) in a host medium (shell with dielectric function ε_S) where $\varepsilon_I = \varepsilon_C$ and $\varepsilon_h = \varepsilon_S$, its effective dielectric function can be expressed as

$$\varepsilon_{eff} = \varepsilon_C\frac{(\varepsilon_C + 2\varepsilon_S) + 2f(\varepsilon_C - \varepsilon_S)}{(\varepsilon_C + 2\varepsilon_S) - f(\varepsilon_C - \varepsilon_S)}. \tag{2.7.2}$$

Again, f is the filling factor that in the case of a spherical nano-shell is given by $f = R_c^3/R_S^3$. Notice that when $f = 1$ (core-material particle) $\varepsilon_{eff} = \varepsilon_C$. On the contrary, when $f = 0$ (shell-material particle) $\varepsilon_{eff} = \varepsilon_S$. Many authors have used this EMT to model the response of core-shell NPs.

According to the concept of internal homogenization, a more complex approach was introduced. The polarizability of the equivalent sphere is equated to that of a core-shell in the electrostatic approximation. According to this, the effective dielectric function for a core-shell NP in vacuum is given by [79]

$$\frac{\varepsilon_{eff} - 1}{\varepsilon_{eff} + 2} = \frac{(\varepsilon_S - 1)(\varepsilon_C + 2\varepsilon_S)f(\varepsilon_C - \varepsilon_S)(1 + 2\varepsilon_S)}{(\varepsilon_S + 2)(\varepsilon_C + 2\varepsilon_S) + 2f(\varepsilon_C - 1)(\varepsilon_C - \varepsilon_S)}, \tag{2.7.3}$$

where f is the previously defined filling factor. By rearranging Equation (2.7.3), the effective dielectric function can be expressed as the one given by an MG EMT, Equation (2.7.2), assuming a core embedded in a shell material medium with a filling factor of f . This equation that is independent of the particle size is only valid in the regime in which the size of the particle is much smaller than the incident wavelength (electrostatic approximation)[79].

The Maxwell Garnett(MG) approximation, also known as the Clausius-Mossotti approximation, is one of the most widely used methods for calculating the bulk dielectric properties of inhomogeneous materials [80, 81]. It is useful when one of the components can be considered as a host in which inclusions of the other components are embedded. It involves an exact calculation of the field induced in the uniform host by a single spherical or ellipsoidal inclusion and an approximate treatment of its distortion by the electrostatic interaction between the different inclusions. This distortion is caused by the charge dipoles and higher multipoles induced in the other inclusions. The induced dipole moments cause the longest range distortions and their average effect is included in the MG approximation which results in a uniform field inside all the inclusions. This approach has been extensively used for studying the properties of two-component mixtures in which both the host and the inclusions are isotropic materials with scalar dielectric coefficients. It has also been applied in the study of the Hall effect in inhomogeneous materials, where the components have tensor electrical conductivities under applied magnetic field. There are many possible locally anisotropic inhomogeneous materials in which the local dielectric coefficient is a tensor. Many studies use the effective-medium approximation [82]. This approximation is based on a self consistent procedure in which a grain of one of the components is assumed to have a convenient shape (usually spherical or ellipsoidal) and to be embedded in an effective medium whose properties are determined self-consistently.

2.8 The Optical Responses of the Dielectric/Metal Core/Shell Nanoparticles

The MG theory assumes that the field across the spherical inclusions in the matrix is uniform. This assumption allows the calculation of polarizability of each spherical inclusion. Let us consider a heterogeneous medium where the matrix material has relative permittivity ε_{mat} and the spherical nanoparticle inclusions have relative permittivity of ε_{inc}. We can deduce the dipole polarizability of the nanoparticles as

$$\alpha = 4\pi a^3 \frac{\varepsilon_{inc} - \varepsilon_{mat}}{\varepsilon_{inc} + 2\varepsilon_{mat}}, \tag{2.8.1}$$

where α is the dipole polarizability of each nanoparticle, and a is the radius of the nanoparticle. The effective relative permittivity (ε_{eff}) of the ensemble can be evaluated from the Clausius Mossotti (CM) equation. We have

$$\varepsilon_{eff} = \varepsilon_{mat}[(1 + \frac{\frac{f}{\nu}\alpha}{1 - \frac{f\alpha}{3\nu}})] \tag{2.8.2}$$

Here, f is the volume filling fraction of the ensemble and ν is the volume of the nanoparticle. The MG theory models the individual inclusions as dipoles only and the overall polarizability of the medium is modeled as an average of the individual dipole polarizabilities of the inclusions [71].

The electric field of a dipole embedded in a uniform unbounded medium with permittivity ε_h is given by [83]

$$E_{dip} = \frac{1}{4\pi\varepsilon_h r^3}[3(p \cdot \hat{e}_r)\hat{e}_r - p], \tag{2.8.3}$$

where $p = qd$ is a dipole moment, $\hat{e}_r$ is the unit radial vector, and r is the radial distance from the center of the dipole.

The polarizability of dielectric core/metal shell geometry is given by:

$$\alpha = V\frac{(\varepsilon_m - \varepsilon_d)(\varepsilon_c + 2\varepsilon_m) + f(\varepsilon_c - \varepsilon_m)(\varepsilon_d + 2\varepsilon_m)}{(\varepsilon_m + 2\varepsilon_d)(\varepsilon_c + 2\varepsilon_m) + 2f(\varepsilon_m - \varepsilon_d)(\varepsilon_c - 2\varepsilon_m)}, \tag{2.8.4}$$

where $\varepsilon_c, \varepsilon_m$ and ε_d are the dielectric functions of the core, metal and surrounding dielectric respectively. The fill fraction, *f*, is the fraction of the volume occupied by the core, $f = (\frac{r_c}{r_m})^3$. As the fraction approaches one, the resonance condition in terms of ε_m moves to more negative values, and the LSPR red-shifted2.7[84].

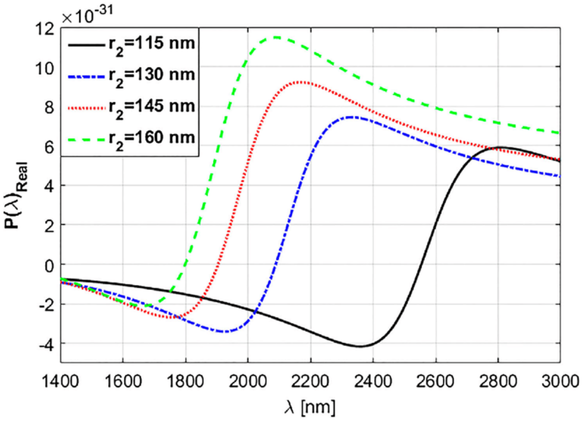

Figure 2.7: The real part of the polarizability of core-shell nanoparticle with fixed shell radius as $r_2 = 160nm$.

The plasmon resonance frequency depends on the dielectric function of the surrounding environment, the dielectric function and size of the core semiconductor and the coated metal. The effect of coating a core/shell QDs with a plasmonic metals is to shift the SP frequency in the desired region of EM spectrum.

2.9 The Refractive Index and Energy Gap of Semiconductors

The refractive index and energy gap of semiconductors represent two fundamental physical aspects that characterize their optical and electronic properties. The applications of semiconductors as electronic, optical and optoelectronic devices are very much determined by the nature and magnitude of these two elementary material properties. These properties also aid in the performance assessment of band gap engineered structures for continuous and optimal absorption of broad band spectral sources. In addition, devices such as photonic crystals, wave guides, solar cells and detectors require a pre-knowledge of the refractive index and energy gap. Application specific coating technologies ($ASPECT^{TM}$) including antireflection coatings and optical filters rely on the spectral properties of materials. The energy gap determines the threshold for absorption of photons in semiconductors. The refractive index in the semiconductor is a measure of its transparency to incident spectral radiation. A correlation between these two fundamental properties has significant bearing on the band structure of semiconductors. Recently it reported that, the absorption of an optical quantum will raise an electron in alkali halides to an excited state rather than freeing it from the center[85]. Thermal energy then moves this electron to the conduction band from the lattice. Such a photo effect takes place in imperfections at certain lattice points, and thus, the electron behaves similar to an electron in an isolated atom with a dielectric constant of the bulk material. As a result of this effective dielectric constant, ε_{eff}, the energy levels of the electron are scaled down by a factor of $1/\varepsilon_{eff}^2$ which approximately corresponds to the square of the refractive index, n. This factor, thus, should be proportional to the energy required to raise an electron in the lattice to an excited state as given by the Bohr formula for the ionization energy, E, of the hydrogen atom, $E = 2\pi^2 m^* e^4/e^2 h^2$ [86], where, m^* is the electron effective mass, e is the electronic charge, e is the relative permittivity and h is the Plank constant. This minimum energy determines the threshold wavelength, λ_e, which then varies as the fourth power of the refractive index. Experimental data on different photoconductive compounds show that the values of n^4/λ_e were close to throughout a range of refractive indices. The similarities in the quotient show that the photoelectrons stem from the same type of lattice imperfections, or alternatively, the binding energies to the different types of hydrogen-like centers are similar [86].

2.10 Optical Absorbance

An important parameter that is used to characterize the optical properties of a sample is the absorbance. Assuming that the incident electromagnetic wave is polarized along the positive z-axis, the intensity, $I(z)$, of light that passes through a thickness z of a sample is given by [87]

$$I(z) = I(0)e^{-\alpha z}, \tag{2.10.1}$$

where $I(0)$ is the intensity of light before passing through the sample (at $z = 0$) and α is the absorption coefficient defined by

$$\alpha = \frac{4\pi n_2}{\lambda}. \tag{2.10.2}$$

Here λ is the wavelength of the incident radiation and n_2 is the imaginary part of the refractive index.

The absorbance of the system is defined as $A = \ln[I(z)/I(0)]$. In our case, setting

$z = t_{Ag}$ in Eq. (2.10.1), we find that the absorbance to be:

$$A(\lambda) = \frac{4\pi n_2}{\lambda} t_{Ag}, \tag{2.10.3}$$

where $t_{Ag} = r_2 - r_1$ is the thickness of the silver shell.

Optical properties and enhanced optical-tunability of core/ shell nanoparticles (NPs) are determined by shape, size, permittivity, and geometrical arrangement of building blocks. However, the properties of magnetite core particles such as reactivity, thermal stability, and optical properties could be investigated in order to achieve overall stability of particles and the dispersibility of core particles.

2.11 Scattering and Absorption Cross-Sections

The scattering and absorption cross sections of a composite nanoparticle can be related to its polarizability. Within the quasi-static approximation, the corresponding cross-sections are given by [70]

$$C_{abs} = kIm\alpha, \quad C_{sca} = \frac{k^4}{6\pi}|\alpha|^2, \tag{2.11.1}$$

where the wave vector $k = 2\pi\sqrt{\frac{\varepsilon_h}{\lambda}}$ with λ and ε_h being the wavelength of light and permittivity of the surrounding medium, respectively. As the polarizability is proportional to the volume, we can see that C_{sca} depends on the square of the volume while C_{abs} scales only linearly with volume. Therefore, small particles prevalently absorb light, while the scattering process is dominant in large particles [88].

The sum of the scattering and absorption cross sections give the extinction cross section C_{ext}. C_{ext} is a measure of the total effective area that the EM fields perceive when interacting with the particle [89]. Thus,

$$C_{ext} = C_{abs} + C_{sca}. \tag{2.11.2}$$

The absorption, scattering, and extinction cross sections of the metallic NPs are often normalized to the particles geometrical cross-sectional area projected on to a plane perpendicular to the incident beam and expressed as [70, 90]

$$Q_{abs} = \frac{C_{abs}}{G}, Q_{sca} = \frac{C_{sca}}{G}, Q_{ext} = \frac{C_{ext}}{G}, \qquad (2.11.3)$$

where Q_{abs}, Q_{sca} and Q_{ext} are the absorption, scattering and extinction efficiencies of the particle, respectively. G is the geometrical cross-sectional area projected on to a plane perpendicular to the incident beam. For sufficiently small particles the absorption and scattering efficiencies varies as [70]:

$$Q_{abs} \propto \frac{1}{\lambda}, \quad Qsca \propto \frac{1}{\lambda^4}. \qquad (2.11.4)$$

Equation (2.11.4) indicate that absorption is dominant relative to scattering in long wavelength limits. In this limit, all the EM energy removed from the impinging radiation transform in to work done to induce the dipole moment on the NP [91]. For nanoparticles that are much smaller than the wavelength of light $(R < 10)$ nm, only the dipole oscillations contribute significantly to the extinction cross section [91]. In view of Eq. (2.11.4), in the very small particle limit [92, 93]

$$Q_{ext} = Q_{abs}. \qquad (2.11.5)$$

Chapter 3

Enhancement of the Optical Response of $Fe_3O_4@Ag$ Core-Shell Nanoparticles

3.1 Introduction

Nanoscience and nanotechnology are recent revolutionary developments of science and technology that are evolving at a very fast pace in the last few decades. Materials in the nanometer size regime show behavior which are intermediate between that of a macroscopic solid and an atomic or molecular system because of high surface to volume ratio, quantum size effect, and electrodynamical interactions [94]. Nanoparticles (NPs) made of noble metals like Au and Ag exhibit surface plasmonic resonance (SPR) [95, 96]. Plasmonic effects enhance absorbance and scattering in the vicinity of the plasmon resonances. Moreover, the intensity and position of plasmon resonance in absorption spectra depend on the shape, size, and the embedding medium. SPR has been used for biosensing, photothermal therapy applications [97, 98].

Core-shell nanoparticles are heterogeneous NPs composed of two or more materials [99]. A wide range of organic and inorganic nanomaterial can be used for forming both, the core and the shell comprising core-shell NP [100]. Core/shell composite nanostructures (NSs) have attracted much attention in recent years [101], which exhibit diverse unique material properties [102], not shown by the core or the shell materials alone, including monodispersion, core/shell operability, stability, and self-assembly. Moreover, because of the strong exciton coupling effect between the surface plasmon resonance (SPR) of the noble metal and the excitons of semiconductors [103], [104] the noble metal/semiconductor core/shell composite nanostructure has been one of the most promising composite for various applications.

Among the various inorganic semiconductor nanomaterials, magnetite (Fe_3O_4) nanoparticles have attracted great attention due to the promising combination of size-dependent electronic, optical, photochemical, and luminescent properties combined with the availability, a great variety of attainable geometries of nano assemblies, low toxicity [105, 106]. The broad spectrum of applications of Fe_3O_4 NPs, such as sensors, solar cells, bioimaging, photocatalysis, UV-shielding, LEDs put forth rigorous requirements for chemical, thermal, and photochemical stability of Fe_3O_4 NPs, versatility of surface chemistry, control of the Fe_3O_4 NP size and compatibility of Fe_3O_4 NPs with water based bio-environments. Many of these issues can be successfully addressed by combining magnetite with noble metals in the form of host composites and core/shell NPs. Indeed, magnetite/noble-metal core/shell nanocomposites find broad potential applications because they cannot only combine the unique properties of metals and semiconductors, but also generate novel electrical, optical, and, catalytic properties due to the synergetic interaction between the metal and the semiconductor components [107, 108]. Due to its high optoelectronic efficiency relative to the indirect band gap group-IV crystals, it is considered as a reliable material for visible and near-ultraviolet applications.

Silver-coated Fe_3O_4 nanohybrids have been used in a broad range of applications including chemical and biological sensing [109], drug delivery [110, 111] catalytic reduction and are promising for water treatment(cleaning) and food preservation [112]. In addition, the as-prepared $Fe_3O_4@Ag$ nanocomposites exhibit a self-sterilizing property that avoids the formation of biofilms which are the most dangerous source capable of spreading toxic bacteria into the environment [113], and hence has great application in catalysis and agriculture [114], improving contrast of IMR in cancer detection [115], for biosensor and ultra-high Raman spectroscopy [116, 117], in diagnostic and therapeutic applications [118].

Many works have been attempted to combine Fe_3O_4 and Ag challenges on the core/shell $Fe_3O_4@Ag$ due to Surface Enhanced Raman Scattering (SERS) effect, Localized Surface Plasmon Resonance (LSPR), where collective oscillations of free conduction electrons in restricted curvature of metallic nanoparticles (MNPs) when illuminated with incident light cause strong optical responses at the plasmon resonance wavelength of MNPs as a non-propagating plasmon. An effective approach for controlling and understanding the phenomena is as follows: shell thickness, core diameter, electronic properties of shell and surrounding environment at two different interfaces (outer interface between the surface and incident light, and inner interface between metal and semiconductor), affect the plasmon resonance wavelength, light scattering, absorption and extinction cross section of core/shell. LSPR causes some suitable characteristics such as enhancement of electric field, localization of energy at nanometer scale, and strongly enhanced absorption and scattering [119].

Analysis of the optical response of nanoparticles thus requires measuring the effective permittivity, ϵ_{eff}, and permeability, μ_{eff} [121]. In this chapter, we studied the optical response of the theoretically modeled $Fe_3O_4@Ag$ core-shell nanoparticles. Silver nanoparticle was selected as a shell on magnetite nanospheres, due to its nontoxic, strong absorption in the UV and visible spectrum [122] and surface plasmon resonance (SPR) which plays a great role in determining the optical response of nanoparticles.

The chapter is organized as follows: The effective permittivity and permeability of the theoretically modelled magnetic-semiconductor/metal core/shell spherical NP embedded in a dielectric host matrix are derived. Firstly, the equations for the effective polarizabilities, and the refractive index are derived. Then, the numerical results are presented and discussed. Specifically, we analyzed the optical responses of $Fe_3O_4@Ag$ core/shell NPs, namely the dielectric function, permeability, polarizability, refractive index, and absorbance. Finally, concluding remarks are presented.

3.2 The Model

In this study, we considered a system of core-shell spherical nanoparticle composed of a magnetic semiconducting core (Fe_3O_4) of radius r_1 and an outer metallic (Ag) shell of radius r_2 embedded in a dielectric host matrix as shown in Fig. 3.1. Because of the magnetite (Fe_3O_4) core with permeability, $\mu \gg 1$, a complete description of the optical properties of the system requires the accurate determination of its effective permittivity ε_{eff} and permeability μ_{eff}. Accordingly, theoretical analysis is carried out based on electrostatic approximation and the Maxwell-Garnet effective medium theory to obtain ε_{eff} and μ_{eff}. Moreover, using these theoretically determined values, we calculated the relevant optical parameters such as the refractive index, the electric and magnetic polarizability, and the absorbance of the modelled core-shell NPs.

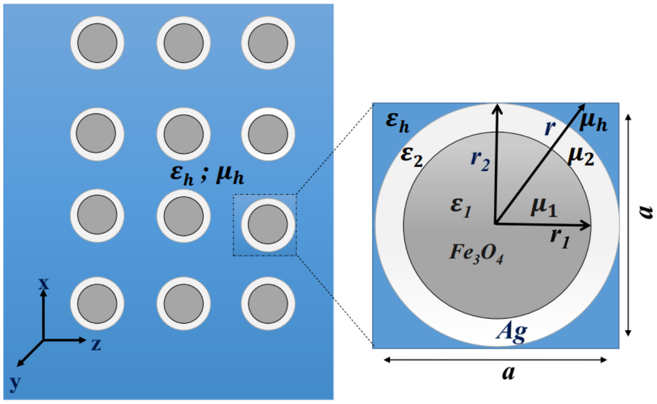

Figure 3.1: Schematic of a core-shell spherical NPs embedded in a matrix. The permittivities and permeabilities are ε_1, μ_1 for the core, ε_2, μ_2 for the shell, and, ε_h, μ_h for the host matrix, respectively. Also, r_1, r_2 are the radii of the core and the shell, and r is the distance from the center of the NP to an observation point.

3.2.1 Permittivity

When the composite core-shell NP is irradiated with an electromagnetic radiation, electric field is induced in the system due to polarization. The distribution of the electrostatic potential Φ associated with the induced field inside and outside of the NP can be obtained by solving the Laplace equation, $\nabla^2\Phi = 0$ in spherical coordinates. Assume that the incident radiation is polarized along the positive z-axis and there is an azimutual symmetry. Then, in the electrostatic approximation, i.e., the wavelength of the incident electromagnetic wave is much greater than a typical size of the NPs, the distribution of the electric potential in the system may be described by the following expressions:

$$\Phi_1(r,\theta) = -E_h A r\cos\theta, \qquad\qquad r < r_1, \tag{3.2.1}$$

$$\Phi_2(r,\theta) = -E_h\left(B - \frac{C}{r^3}\right) r\cos\theta, \qquad r_1 < r < r_2, \tag{3.2.2}$$

$$\Phi_h(r,\theta) = -E_h\left(D - \frac{F}{r^3}\right) r\cos\theta. \qquad r > r_2. \tag{3.2.3}$$

Here Φ_1, Φ_2, and Φ_h are the electric potentials in the core, metal shell, and the host matrix, respectively. E_h is the magnitude of the applied field directed along the z-axis, θ is the zenith angle, and r is the distance from the center of the NP to an observation point. Also, the coefficients A, B, C, D and F are unknown constants that can be determined using appropriate boundary conditions at the core/shell and shell/host interfaces. At this point it is worth noting that the second term on the right-side of Eq. (3.2.3) represents the induced potential outside the core-shell NP. The total induced field outside the concentric spheres represents the optical response of the system. Equivalently, the induced potential outside the concentric spheres is given by

$$\Phi_{ind} = \frac{F E_h}{r^2}\cos\theta, \tag{3.2.4}$$

where the coefficient, F, determined using the boundary condition is found to be(See Appendix):

$$F = \left[\frac{(\varepsilon_1 + 2\varepsilon_2)(\varepsilon_2 - \varepsilon_h) + \nu_f(\varepsilon_1 - \varepsilon_2)(2\varepsilon_2 + \varepsilon_h)}{(\varepsilon_1 + 2\varepsilon_2)(\varepsilon_2 + 2\varepsilon_h) + 2\nu_f(\varepsilon_1 - \varepsilon_2)(\varepsilon_2 - \varepsilon_h)}\right] D r_2^3, \tag{3.2.5}$$

where $\nu_f = (r_1/r_2)^3$.

Note that Φ_{ind} describes the superposition of the applied field and that of a dipole located at the center of the NP. Introducing the dipole moment $\vec{p}$, we may rewrite

Φ_{ind} as

$$\Phi_{ind} = \frac{p\cos\theta}{4\pi\varepsilon_h r^2}, \tag{3.2.6}$$

where p is the magnitude of the electric dipole moment. Using Eqs. (3.2.4) and (3.2.6), we find that the dipole moment of the system to be $\vec{p} = 4\pi\varepsilon_h F\vec{E}_h$, or

$$\vec{p} = \varepsilon_h \alpha D\vec{E}_h, \tag{3.2.7}$$

where α is the polarizability of the core-shell plus host matrix composite system given by

$$\alpha = 4\pi\left[\frac{(\varepsilon_1 + 2\varepsilon_2)(\varepsilon_2 - \varepsilon_h) + \nu_f(\varepsilon_1 - \varepsilon_2)(2\varepsilon_2 + \varepsilon_h)}{(\varepsilon_1 + 2\varepsilon_2)(\varepsilon_2 + 2\varepsilon_h) + 2\nu_f(\varepsilon_1 - \varepsilon_2)(\varepsilon_2 - \varepsilon_h)}\right]r_2^3. \tag{3.2.8}$$

Note that here we are using the concept of internal homogenization of which the polarizability of the equivalent sphere is equated to that of a core-shell in the electrostatic approximation. Accordingly, the effective dielectric function ε_{cs} for a core-shell NP embedded in a host matrix of dielectric function ε_h is related to its polarizability α by the Clausius-Mossotti relation as [123]-[125]

$$\alpha = 4\pi r_2^3 \frac{\varepsilon_{cs} - \varepsilon_h}{\varepsilon_{cs} + 2\varepsilon_h}. \tag{3.2.9}$$

In view of Eqs. (3.2.8) and (3.2.9), we note that the effective permittivity (the effective dielectric function) of the core-shell spherical nanoinclusion is given by

$$\varepsilon_{cs} = \varepsilon_2 \frac{(\varepsilon_1 + 2\varepsilon_2)r_2^3 + 2(\varepsilon_1 - \varepsilon_2)r_1^3}{(\varepsilon_1 + 2\varepsilon_2)r_2^3 - (\varepsilon_1 - \varepsilon_2)r_1^3}. \tag{3.2.10}$$

Furthermore, introducing the volume fraction, β, of the metal coated spherical core-shell nanoparticle as

$$\beta = 1 - \nu_f, \tag{3.2.11}$$

Eq. (3.2.10) for the effective dielectric function of the core-shell composite material takes the form:

$$\varepsilon_{cs} = \varepsilon_2 \frac{\varepsilon_1(3/\beta - 2) + 2\varepsilon_2}{\varepsilon_1 + \varepsilon_2(3/\beta - 1)}. \tag{3.2.12}$$

Now, consider the system composed of a finite number of core-shell NPs uniformly dispersed in a host matrix as shown in Fig. 3.1. Suppose N is the density number of the inclusions (NPs) in the system. Then, the polarizability and the effective permittivity of the system can be described by using the Clausius-Mossotti relation together with the Maxwell-Garnet mixing theory. Accordingly, the electric polarizability and the effective permittivity are related by [126]

$$\frac{N\alpha}{3} = \frac{\varepsilon_{eff} - \varepsilon_h}{\varepsilon_{eff} + 2\varepsilon_h}, \tag{3.2.13}$$

where ε_{eff} is the effective dielectric function of the system and α is the polarizability defined by Eq. (3.2.9). Further, substituting Eq. (3.2.8) into (3.2.13) and manipulating, we get

$$\varepsilon_{eff} = \varepsilon_h \left(\frac{1 + 2f\alpha_{eff}}{1 - f\alpha_{eff}} \right), \tag{3.2.14}$$

where f is the filling factor (the volume fraction of inclusions in the composite) of the core-shell NPs defined by

$$f = \frac{4\pi r_2^3}{3} N, \tag{3.2.15}$$

and $\alpha_{eff} = \alpha/(4\pi r_2^3)$ is the dimensionless effective electric polarizability of the inclusion given by

$$\alpha_{eff} = \frac{\varepsilon_{cs} - \varepsilon_h}{\varepsilon_{cs} + 2\varepsilon_h}. \tag{3.2.16}$$

3.2.2 Permeability

From magnetostatics, we have $\nabla \times \vec{H} = \vec{J}$, where $\vec{H}$ is the field strength and $\vec{J}$ is the current density. If $\vec{J} = 0$, then $\nabla \times \vec{H} = 0$, so that we may introduce a magnetic scalar potential Φ_M such that $\vec{H} = -\nabla\Phi_M$, similar to that in electrostatics. Further, if μ is spatial independent, then $\nabla \cdot \vec{B} = 0$ results to

$$\nabla^2\Phi_m = 0. \tag{3.2.17}$$

That means that the magnetic scalar potential Φ_M satisfies the Laplace equation.

Now, consider the system of core-shell spherical NPs with a magnetic core and a nobel metal shell uniformly dispersed in a dielectric host matrix (see Fig. 3.1). For such systems, an electromagnetic wave incident on the system induces not only an electric polarization but also magnetization. Then, similar to that employed for the electrostatic fields the solution of the Laplace equation for the scalar potential, Φ_m, in the various regions may be assumed to be given by the following equations [127]:

$$\Phi_{m1}(r, \phi) = -H_y A_{1m} r \cos\phi, \qquad r < r_1 \tag{3.2.18}$$

$$\Phi_{m2}(r, \phi) = -H_y \left(A_{2m} - \frac{B_{1m}}{r^3} \right) r \cos\phi, \quad r_1 < r < r_2, \tag{3.2.19}$$

$$\Phi_{mh}(r, \phi) = -H_y \left(A_{3m} - \frac{B_{2m}}{r^3} \right) r \cos\phi, \qquad r > r_2 \tag{3.2.20}$$

where Φ_{m1}, Φ_{m2}, and Φ_{mh} are the magnetic potentials in the magnetic semiconductor core, the metallic shell, and the host matrix, respectively. H_y is the magnitude of the applied field (with $\mathbf{H}_y$ directed along the positive y-axis), ϕ is an 'azimuthal' angle measured with respect to the $+y$-axis, r is the distance from the center of the NP to an observation point. A_{1m}, A_{2m}, A_{3m}, B_{1m}, and B_{2m} are unknown coefficients that need to be determined using the boundary conditions for the $\mathbf{H}$-field. Note that the second term on the right-side of Eq. (3.2.20) represents the magnetic scalar potential outside the core-shell NP due to the induced magnetic dipole. Note that the system's response due to the magnetic component of the applied field is described by the induced field outside the concentric spheres. Hence, we need to find only the coefficient B_{2m}, i.e., imposing the appropriate boundary condition, it is found to have the form:

$$B_{2m} = \left[\frac{(\mu_1 + 2\mu_2)\mu_{2h} + \nu_f(2\mu_2 + \mu_h)\mu_{12}}{(\mu_1 + 2\mu_2)(\mu_2 + 2\mu_h) + 2\nu_f\mu_{12}\mu_{2h}}\right] A_{3m}\, r_2^3, \tag{3.2.21}$$

where $\nu_f = (r_1/r_2)^3$, and introduced the following notations $\mu_{12} = \mu_1 - \mu_2$, and $\mu_{2h} = \mu_2 - \mu_h$.

Hence, the induced magnetic scalar field, Φ_{mi}, outside the core-shell NP becomes

$$\Phi_{mi} = \frac{H_y B_{2m}}{r^2}\cos\phi, \tag{3.2.22}$$

where the coefficient, B_{2m} is given by Eq. (3.2.21).

Note that Φ_{mi} describes the superposition of the applied field and that of a magnetic dipole located at the center of the NP. But, the scalar potential outside the NP may be given by [127]

$$\Phi_{mi} = \frac{m}{4\pi r^2}\cos\phi, \tag{3.2.23}$$

where m is the magnitude of the magnetic dipole moment, $\vec{m}$. Then, combining Eqs. (3.2.22) and (3.2.23), we get $\vec{m} = 4\pi B_{2m} H_y \hat{y}$, or

$$\vec{m} = \kappa_m A_{3m} H_y \hat{y}, \tag{3.2.24}$$

where κ_m is the magnetic susceptibility of the core-shell NP embedded in the host with permeability μ_h given by

$$\kappa_m = 4\pi\left[\frac{(\mu_1 + 2\mu_2)\mu_{2h} + \nu_f(2\mu_2 + \mu_h)\mu_{12}}{(\mu_1 + 2\mu_2)(\mu_2 + 2\mu_h) + 2\nu_f\mu_{12}\mu_{2h}}\right] r_2^3. \tag{3.2.25}$$

The effective permeability μ_{cs} for a core-shell NP embedded in the host matrix of permeability μ_h may be related to its susceptibility κ_m by the Clausius-Mossotti relation as

$$\kappa_m = 4\pi r_2^3 \frac{\mu_{cs} - \mu_h}{\mu_{cs} + 2\mu_h}, \tag{3.2.26}$$

Substituting Eq. (3.2.25) into (3.2.26) and simplifying, we obtain the effective permeability of the core-shell spherical NP to be

$$\mu_{cs} = \mu_2 \left[\frac{(\mu_1 + 2\mu_2) + 2\nu_f(\mu_1 - \mu_2)}{(\mu_1 + 2\mu_2) + \nu_f(\mu_2 - \mu_1)} \right]. \tag{3.2.27}$$

Further, using $\beta = 1 - \nu_f$ which is the volume fraction of the metal coated spherical core-shell NP defined by Eq. (3.2.11), Eq. (3.2.27) for the effective magnetic permeability of the composite material becomes

$$\mu_{cs} = \mu_2 \left[\frac{\mu_1(3/\beta - 2) + 2\mu_2}{\mu_1 + \mu_2(3/\beta - 1)} \right]. \tag{3.2.28}$$

Now, consider the ensemble that is composed of the core-shell NPs homogeneously embedded in the host matrix (see Fig. 3.1). Suppose N is the density number the inclusions (NPs) in the system. Then, using the Clausius-Mossotti relation and the Maxwell-Garnet mixing theory, the magnetic polarizability and permeability are related by [126]-[128]

$$\frac{N\kappa_m}{3} = \frac{\mu_{eff} - \mu_h}{\mu_{eff} + 2\mu_h}, \tag{3.2.29}$$

where μ_{eff} is the effective magnetic permeability of the ensemble and κ_m is the magnetic polarizability defined by Eq. (3.2.26).

Further, substituting Eq. (3.2.26) into (3.2.29) and manipulating, we get

$$\mu_{eff} = \mu_h \left(\frac{1 + 2f\kappa_{eff}}{1 - f\kappa_{eff}} \right), \tag{3.2.30}$$

where $f = 4\pi N r_2^3/3$ is the filling factor (the volume fraction of inclusions in the composite) of the core-shell NPs defined by Eq. (3.2.15) and $\kappa_{eff} = \kappa_m/(4\pi r_2^3)$ is the dimensionless magnetic polarizability which is given by

$$\kappa_{eff} = \frac{\mu_{cs} - \mu_h}{\mu_{cs} + 2\mu_h}. \tag{3.2.31}$$

3.3 Optical Properties of $Fe_3O_4@Ag$ NPs

In this section, we derive the equations for the optical parameters, i.e., the refractive index and the polarizability of a system composed of $Fe_3O_4@Ag$ core-shell NPs embedded in a liquid/water. Hence, in order to get an explicit expression for the refractive index (n), we must fix the permittivities and permeabilities of the constituents (i.e., the magnetic core, metallic shell, and host matrix).

Now we consider the 'bare' metallic (Ag) shell. Note that its response to incident electromagnetic wave (EMW) is solely described by the dielectric function (permittivity) with the permeability being equal to unity ($\mu_2 = 1$). Therefore, we choose the frequency dependent complex dielectric function of the metallic (Ag) to have the Drude form given by

$$\varepsilon_2(\omega) = \varepsilon_\infty - \frac{\omega_p^2}{\omega(\omega + i\gamma)}, \tag{3.3.1}$$

where the constant ε_∞ is the permittivity at high frequencies, ω_p is the plasma frequency, γ is the damping parameter, and ω is the frequency of the incident radiation. Further, separating the real and imaginary parts of Eq. (3.3.1), i.e., $\varepsilon_2 = \varepsilon_2^{'} + i\varepsilon_2^{''}$, we obtain the following:

$$\varepsilon_2^{'}(\omega) = \varepsilon_\infty - \frac{\omega_p^2}{\omega^2 + \gamma^2}, \tag{3.3.2}$$

and

$$\varepsilon_2^{''}(\omega) = \frac{\gamma\omega_p^2}{\omega(\omega^2+\gamma^2)}, \tag{3.3.3}$$

where $\varepsilon_2^{'}(\omega)$ and $\varepsilon_2^{''}(\omega)$, respectively, are the real and imaginary parts of ε_2.

It is worth noting that the dielectric function of metals, in particular the noble and alkali metals, vary significantly as a function of the frequency of the incident light in the visible spectral region. However, in the same spectral region the dielectric function for magnetite varies very little with frequency compared with that of the metal. Hence, without loss of generality we assumed both the permittivity (ε_1) and permeability (μ_1) of magnetite as well as the permittivity of the host (ε_h) to be real constants independent of frequency.

3.3.1 Effective Electric and Magnetic Polarizabilities

The effective electric polarizability of the system may be obtained by substituting Eq. (3.2.12) into (3.2.16), i.e.,

$$\alpha_{eff} = 1 - \frac{3}{2}\left[\frac{\varepsilon_1\varepsilon_h + \varepsilon_2\varepsilon_h(3/\beta-1)}{\varepsilon_1\varepsilon_h + \varepsilon_2\varepsilon_h(3/\beta-1) + \varepsilon_1\varepsilon_2[3/(2\beta)-1] + \varepsilon_2^2}\right]. \tag{3.3.4}$$

Because ε_{eff} for the system is complex, the effective electric polarizability α_{eff}, defined by Eq. (3.3.4) is also complex, which may be written as

$$\alpha_{eff} = \alpha_{eff}^{'} + i\alpha_{eff}^{''}, \tag{3.3.5}$$

where $\alpha_{eff}^{'}$ and $\alpha_{eff}^{''}$ are its real and imaginary parts, respectively. Substituting $\varepsilon_2 = \varepsilon_2^{'} + i\varepsilon_2^{''}$ into (3.3.4), we get

$$\alpha_{eff}^{'} = 1 - \frac{3}{2}\left[\frac{(\varepsilon_2^{'}\phi' + \varepsilon_1\varepsilon_h)\varphi' + (\varepsilon_2^{''}\phi')\psi}{\varphi'^2 + \psi^2}\right], \tag{3.3.6}$$

and

$$\alpha_{eff}^{''} = \frac{3}{2}\left[\frac{(\varepsilon_2^{'}\phi' + \varepsilon_1\varepsilon_h)\psi - (\varepsilon_2^{''}\phi')\varphi'}{(\varphi')^2 + \psi^2}\right], \tag{3.3.7}$$

where

$$\phi' = \varepsilon_h\left(\frac{3}{\beta} - 1\right),$$

$$\eta = \phi' + \varepsilon_1\left(\frac{3}{2\beta} - 1\right),$$

$$\varphi' = (\varepsilon_2^{'})^2 - (\varepsilon_2^{''})^2 + \varepsilon_2^{'}\eta + \varepsilon_1\varepsilon_h,$$

$$\psi = 2\varepsilon_2^{'}\varepsilon_2^{''} + \varepsilon_2^{''}\eta.$$

Similarly, substituting Eq. (3.2.28) into (3.2.31), we find the effective magnetic polarizability to be:

$$\kappa_{eff} = 1 - \frac{3}{2}\left(\frac{\mu_1\mu_h + \mu_2\Delta}{\mu_1\mu_h + \mu_2\Delta + \mu_1\phi + \mu_2^2}\right). \tag{3.3.8}$$

where

$$\Delta = \mu_h\left(\frac{3}{\beta} - 1\right),$$

$$\phi = \mu_2\left(\frac{3}{2\beta} - 1\right),$$

In particular, for the case where μ_1 is a real constant and $\mu_2 = \mu_h = 1.0$ (nonmagnetic), we find that Eq. (3.3.8) reduces to:

$$\kappa_{eff} = 1 - \left[\frac{3 + \beta(\mu_1 - 1)}{\mu_1 + 2}\right], \tag{3.3.9}$$

and the corresponding effective permeability, Eq. (3.2.30), becomes

$$\mu_{eff} = 1 - \frac{3f(\beta - 1)(\mu_1 - 1)}{(\mu_1 + 2) + f(\beta - 1)(\mu_1 - 1)}. \tag{3.3.10}$$

Note that both κ_{eff} and μ_{eff} of Eqs. (3.3.9) and (3.3.10) are real constants.

3.3.2 Effective Refractive Index

The complex refractive index $\tilde{n}$ of the the system consisting of spherical core-shell composite NSs embedded in a matrix may be defined as

$$\tilde{n}(\omega) = \sqrt{\varepsilon_{eff}\mu_{eff}}, \tag{3.3.11}$$

where ε_{eff} and μ_{eff} are the effective permittivity and permeability of the system given by Eqs. (3.2.14) and (3.2.30), respectively. Now, using $\varepsilon_{eff} = \varepsilon^{'}_{eff} + i\varepsilon^{''}_{eff}$ and $\mu_{eff} = const$, Eq. (3.3.11) may be written as

$$\tilde{n} = \sqrt{(\varepsilon^{'}_{eff}\mu_{eff}) + i(\varepsilon^{''}_{eff}\mu_{eff})}, \tag{3.3.12}$$

Further, introducing

$$\tilde{n} = n_1 + in_2, \tag{3.3.13}$$

where n_1 and n_2 are the real and imaginary parts, respectively. Then, squaring Eq. (3.3.13), we get

$$\tilde{n}^2 = (n_1^2 - n_2^2) + i(2n_1n_2). \tag{3.3.14}$$

Also, squaring Eq. (3.3.12), equating with Eq. (3.3.14), and manipulating, we find that the real and imaginary parts of the refractive index takes the form

$$n_1 = \frac{1}{\sqrt{2}}\big[\mu_{eff}(\varepsilon^{'2}_{eff} + \varepsilon^{''2}_{eff})^{1/2} + \varepsilon^{'}_{eff}\mu_{eff}\big]^{1/2}, \tag{3.3.15}$$

and

$$n_2 = \frac{1}{\sqrt{2}}\big[\mu_{eff}(\varepsilon^{'2}_{eff} + \varepsilon^{''2}_{eff})^{1/2} - \varepsilon^{'}_{eff}\mu_{eff}\big]^{1/2}. \tag{3.3.16}$$

It is worth noting that the phase velocity of the wave propagating in the medium is described by real part of refractive index, n_1, and the attenuation of the wave as it propagates through the medium is determined by its imaginary part, n_2. [127]

3.4 Numerical Analysis

In this section, we present the numerical analysis performed to characterize the optical response of the theoretically modeled spherical $Fe_3O_4@Ag$ core-shell NPs embedded in a dielectric host matrix. We used Wolfram Mathematica (9 and 10) Software codes for numerical evaluation, optimization and visualization of a very wide range of numerical functions. In particular, the electric and magnetic polarizabilities, the refractive index, and the absorbance under different conditions (i.e., varying β, f and ε_h) will be simulated. The parameter values used are $\varepsilon_\infty = 4.5$, $\omega_p = 1.46\times10^{16}\ rad/s$ and $\gamma = 1.67\times10^{13}\ rad/s$ for the silver shell; and $\varepsilon_1 = 5.85$ and $\mu_1 = 9.0$ for magnetite.

3.4.1 Electric Polarizability

The real and imaginary parts of the dimensionless electric polarizabilities (α'_{eff} and α''_{eff}, respectively) of the spherical $Fe_3O_4@Ag$ nanoinclusions as a function of the wavelength of the incident radiation for different values of the metal fraction (the volume fraction of the metal coated β), and constant values of $\varepsilon_h = 1.77$ and NPs size $r_2 = 30\ nm$ are depicted in Fig. 3.2. Both the graphs of α'_{eff} and α''_{eff} shows that, it possess two set of resonance peaks - the first in the UV region in the vicinity of the wavelength $\lambda = 300\ nm$ and the second peaks in the visible spectral region above the wavelength of $\lambda = 420\ nm$. The first and second sets of peaks arise due to the coupling/interactions of the surface plasmon oscillations of silver with the semiconductor/dielectric at the inner (Fe_3O_4/Ag) and outer (Ag/host) interfaces and/or to near-field inter-particle interaction, respectively.

Moreover, it is found that the polarizabilities, α'_{eff} and α''_{eff}, increases as the value of the metal fraction β is increased (or equivalently as the core radius r_1 is decreased).

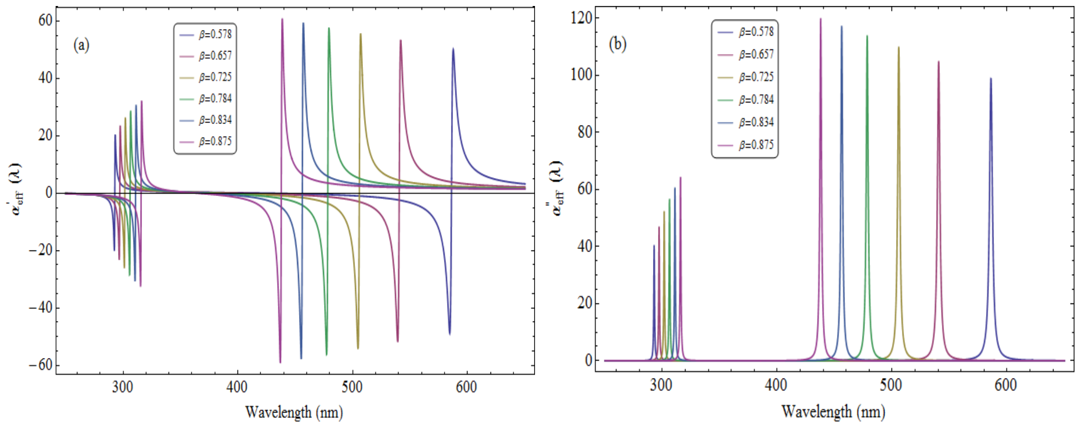

Figure 3.2: The real (a) and imaginary (b) parts of the electric polarizability versus wavelength for different values of β; with $\varepsilon_h = 1.77$ and $r_2 = 30$ nm fixed constant.

Moreover, the second set of peaks are more pronounced than the first set. This may be explained with the fact that the surface area of the outer surface (Ag/host interface) of the Ag shell is larger than that of the inner surface area (magnetite/Ag interface), and hence large number of carriers available at the outer interface than the inner.

The analysis also shows that when β is increased, the first set of peaks in the UV region are red-shifted which is mainly attributed to the decrease of the size of the NPs, i.e., the semiconducting Fe_3O_4 core. On the other hand, the second set of peaks are blue-shifted with an increase of β, due to an increase in the thickness of the metallic shell. Indeed, the two resonance peaks corresponding to each NPs become closer and closer to each other as β is increased indicating that the metallic shell plays the dominant role in determining both the real and imaginary parts of the electric polarizability.

3.4.2 Refractive Index

In this section, the real and imaginary parts of the refractive index of $Fe_3O_4@Ag$ core-shell spherical nanoinclusions are numerically analyzed using Eqs. (3.3.15) and (3.3.16) together with the corresponding expressions for ε_{eff} and μ_{eff}, i.e., Eqs. (3.2.14) and (3.2.30). The following parameter values are used: $\varepsilon_1 = 5.85$ and $\mu_1 = 9.0$ for Fe_3O_4 with the other parameters being the same as that used in Section 3.4.1.

Figure 3.3 depicts the graphs of the real ($n_1(\lambda)$) and imaginary ($n_2(\lambda)$) parts of the refractive index of the spherical nanoinclusions as a function of the wavelength of the incident radiation for different values of β. As the Figures show, there are two sets of resonance peaks. The first set of peaks for both n_1 and n_2 are located around $\lambda = 300$ nm in the UV region and is linked to the dispersion/absorption at the inner (magnetite/Ag) interface. The second set of peaks are those found above the wavelength of $\lambda = 420$ nm all in the visible spectral region, which are connected to Ag/host interface. As it is seen from the graphs, propagation of light/photon is more pronounced in the second set of peaks than the first set of peaks. As it can be clearly seen from Fig. 3.3, the effect of decreasing the radius of the core, i.e., increasing β, results in a decrease of the refractive index; accompanied with a slight blue shift in the first set of peaks and red shift in the second set of peaks. In addition, the resonances for each NPs gets more closer to each other, when the metal fraction β is increased.

For $Fe_3O_4@Ag$ nanostructure, the Fermi level of Ag is near ‘weak’ energy levels of Fe_3O_4; therefore, electrons can be transferred readily from the Ag weak energy levels to the Fermi level of Fe_3O_4, where these electrons are excited by incident ray. The energy level of these excited electrons is near the conduction band of Ag;

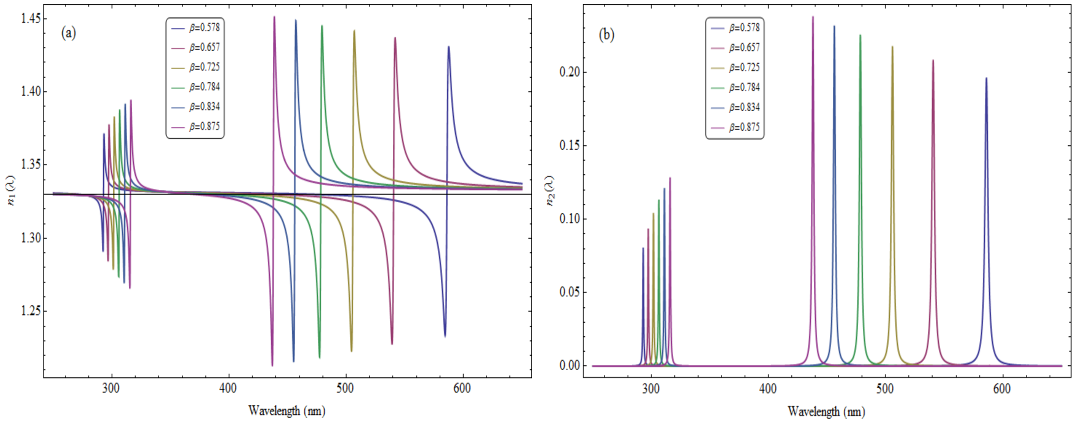

Figure 3.3: The real (a) and imaginary (b) parts of the refractive index versus wavelength for different values of β. Also, $f = 0.001$, $r_2 = 30\ nm$, and $\varepsilon_h = 1.77$.

therefore, these excited electrons are transferred to the conduction band of Ag where they become a part of the electron/hole recombination process, increasing the near band edge emission. As a consequence of the electrons transfer, the visible emission will be reduced and will be enhanced which is in agreement to that reported in Ref. [129]. This maximum value of refractive index can be used for medical application in nanofields like cancer treatment, cancer detection.

In addition to the metal fraction β, the refractive index of the system depends on other factors such as the surrounding medium (the dielectric function ε_h of the host matrix) and the filling factor. The effect of the dielectric function ε_h on the real and imaginary parts of the refractive index of an ensemble of spherical $Fe_3O_4@Ag$ NPs embedded in a host matrix as a function of the wavelength of the incident radiation is shown in Fig. 3.4. It is shown that as ε_h is increased from $1.00 - 2.25$ in steps of 0.25 the the resonance peaks of both $n_1(\lambda)$ and $n_2(\lambda)$ increase with the peaks of the second set located above $\lambda = 460\ nm$ more pronounced than the first set of peaks located

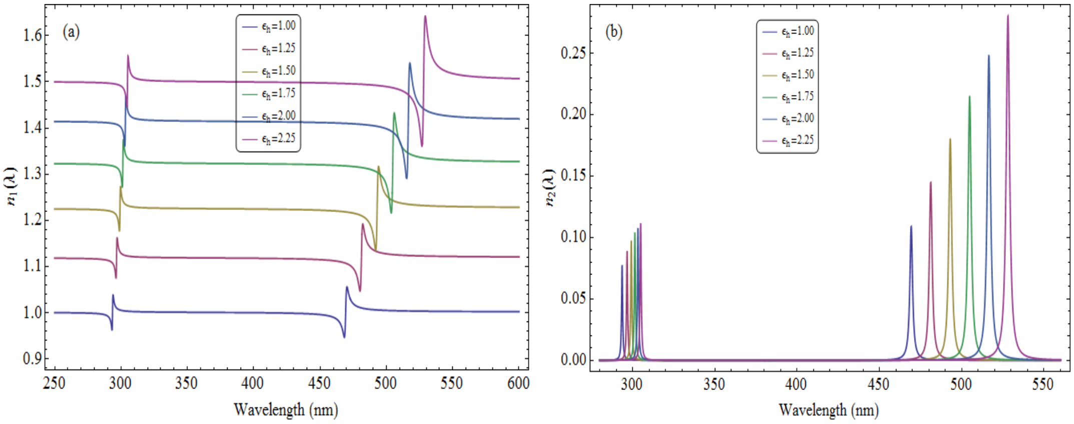

Figure 3.4: The real (a) and imaginary (b) parts of the refractive index as a function of wavelength for different values of the dielectric function of the host, ε_h; with $\beta = 0.65$, $r_2 = 30\ nm$ and $f = 0.001$.

around $\lambda = 300\ nm$. Both set of peaks shift toward high wavelength regions (red shift) with an increase in ε_h. Moreover, for each values of ε_h the "reference" value of the real part of the refractive index, which is given by $n_1 = \sqrt{\varepsilon_h}$, shifts upward along the n_1-axis as the value of ε_h is increased.

Figure 3.5 shows the dependence of the real and imaginary parts of the refractive index of the system on the filling fraction (the volume fraction of inclusions in the composite) f; versus wavelength for fixed values of β, r_2, and ε_h. The Figure depicts that there are two sets of resonance peaks for both the $n_1(\lambda)$ and $n_2(\lambda)$, located on either sides of $\lambda = 300\ nm$ (first sets shown as insets) and $\lambda = 506\ nm$ (second peaks). It is seen that all the peaks get larger and larger as filling factor is increased from $f = 0.001 - 0.006$, in steps of 0.001. In other words, when the filling factor (f) is increased, the intensity of the refractive index is highly enhanced suggesting that the shell thickness and the density of the packed nanosphere arrays can play great role to improve the photoluminescence [130]. It is worth noting that unlike that of

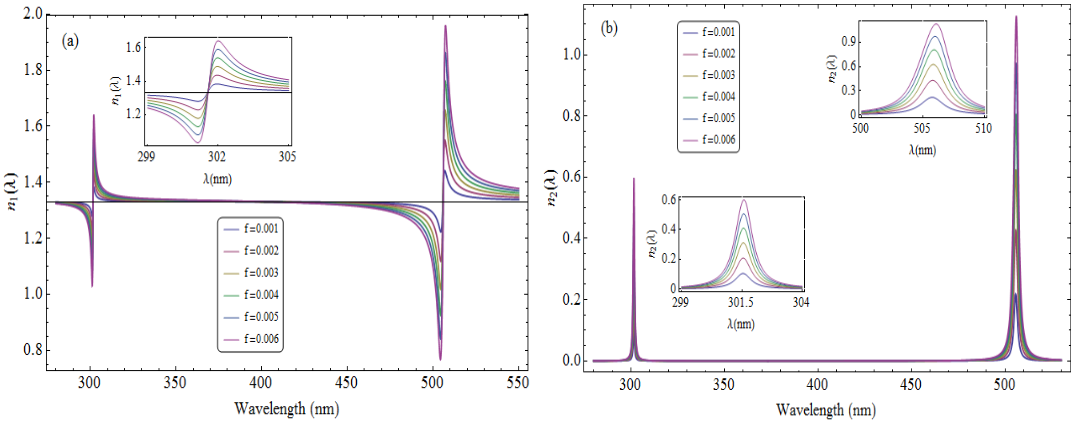

Figure 3.5: The real (a) and imaginary (b) parts of the refractive index versus wavelength for different values of filling fraction, f; with $\beta = 0.65$, $r_2 = 30\ nm$ and $\varepsilon_h = 1.77$.

observed with β and ε_h (see Figs. 3.3 and 3.4), varying the filling fraction f does not result to a shift of the resonance peaks of both the real and imaginary parts of n, i.e., it only results in their enhancement with no significant shift observed in the location of the peaks which is in a good agrement with the result recently reported [120].

3.5 Optical Absorbance

An important parameter that is used to characterize the optical properties of a sample is the absorbance. Assuming that the incident electromagnetic wave is polarized along the positive z-axis, the intensity, $I(z)$, of light that passes through a thickness z of a sample is given by [130]

$$I(z) = I(0)e^{-\alpha z}, \tag{3.5.1}$$

where $I(0)$ is the intensity of light before passing through the sample (at $z = 0$) and α is the absorption coefficient defined by

$$\alpha = \frac{4\pi n_2}{\lambda}. \tag{3.5.2}$$

Here λ is the wavelength of the incident radiation and n_2 is the imaginary part of the refractive index.

The absorbance of the system is defined as $A = \ln[I(z)/I(0)]$. In our case, setting $z = t_{Ag}$ in Eq. (3.5.1), we find that the absorbance to be:

$$A(\lambda) = \frac{4\pi n_2}{\lambda} t_{Ag}, \tag{3.5.3}$$

where $t_{Ag} = r_2 - r_1$ is the thickness of the silver shell.

Optical properties and enhanced optical-tunability of core/ shell nanoparticles (NPs) are determined by shape, size, permittivity, and geometrical arrangement of building blocks. However, the properties of magnetite core particles such as reactivity, thermal stability, and optical properties could be investigated in order to achieve overall stability of particles and the dispersibility of core particles.

The graphs of the optical absorbance of an ensemble of spherical $Fe_3O_4@Ag$ nanoparticles embedded in a dielectric host matrix ($\varepsilon_h = 1.77$) versus wavelength for different values of β (or thickness t_{Ag}) of the metallic shell are shown in Fig. 3.6. The filling fraction and the size of the NPs are kept constant - $f = 0.001$ and $r_2 = 30\ nm$, respectively. The figure shows that there are two sets of absorption peaks - the first in the UV spectral region in the vicinity of $\lambda = 300\ nm$ and the second set located in the visible region above $\lambda = 420\ nm$. It is seen that as t_{Ag} is increased the absorption peaks of the first set of resonant peaks in the UV region increases with the peaks shifting towards low energy values (red shift) and the second

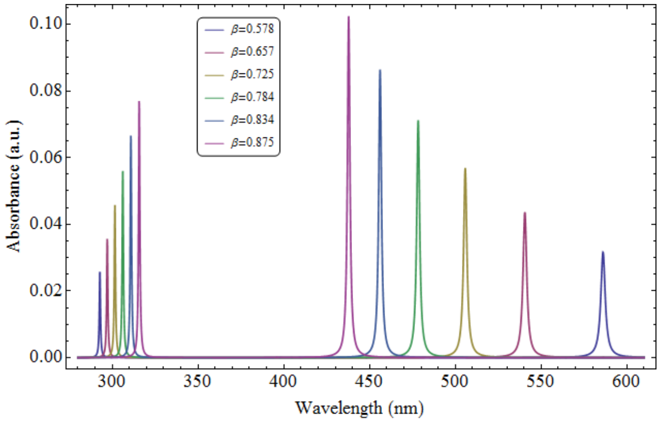

Figure 3.6: The absorbance versus wavelength for different values of β; with $f = 0.001$, $r_2 = 30\ nm$ and $\varepsilon_h = 1.77$.

set of peaks also increases with a shift towards high energy values (blue shift). It is worth noting that the absorption peaks of the first sets arise due to near band edge absorption of the free exciton recombination while the red shift of the absorption edge with an increase of t_{Ag} (or a decrease of the core radius r_1) is attributed to increase in the energy gap of the core nanoparticles [125]. On the other hand, the absorption peaks of the second set located above the wavelength of $\lambda = 420\ nm$ arises due to the deep level emissions which are attributed to the surface plasmon resonance of silver nanoshell - this explains as to why the absorption peaks gets enhanced as well as blue shifted as the thickness of the silver shell increased from $7.5 - 15.0\ nm$ (or $\beta = 0.578 - 0.875$). Furthermore, the effect of varying the dielectric host matrix ε_h on the optical absorbance as a function of the wavelength of the incident radiation is plotted as shown in Fig. 3.7. Here, the following parameter values kept constant: $f = 0.001$, $r_2 = 30\ nm$ and $\beta = 0.65$. It shows that the absorbance have two sets of peaks - the first around $\lambda = 300\ nm$ in the UV region and the second peaks located

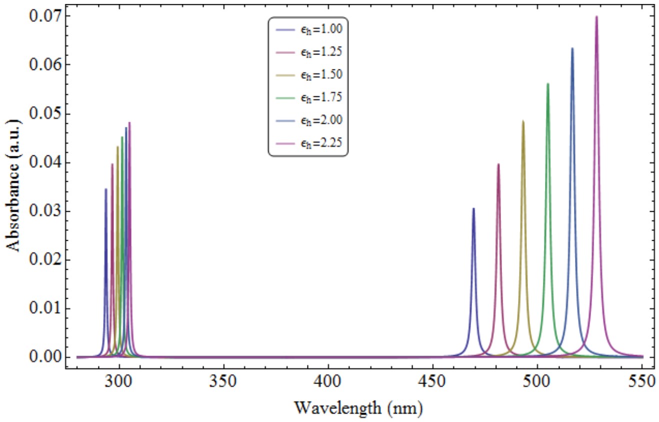

Figure 3.7: The absorbance versus wavelength for different values of ε_h; with $\beta = 0.65$, $r_2 = 30\ nm$ and $f = 0.001$.

above $\lambda = 465\ nm$ in the visible spectral region. In addition, unlike that obtained in Fig. 3.6 both sets of resonance peaks are red shifted as the value of the dielectric function of the host matrix is increased. Also, it is found that both sets of absorbance peaks increase as ε_h is increased with more enhancement being observed in the second set of peaks than the first. The absorption efficiency spectra of Fe_3O_4 NPs with different radius coated by Ag outer shell thickness and the LSPR peak wavelength of $Fe_3O_4@Ag$ NPs with the volume fraction of the shell which is in good agrement with Refs [125]-[132].

Figure 3.8 shows the dependence of the optical absorbance on the filling factor f as a function of the wavelength of the incident radiation, with the following parameter values kept constant: $\beta = 0.65$, $r_2 = 30\ nm$ and $\varepsilon_h = 1.7689$. It can be observed that both sets of resonance peaks of the absorbance increase with an increase of the filling factor from $f = 0.001 - 0.006$ in steps of 0.001; with no significant shift in the respective peaks position in which it is in a good agreement with the result reported

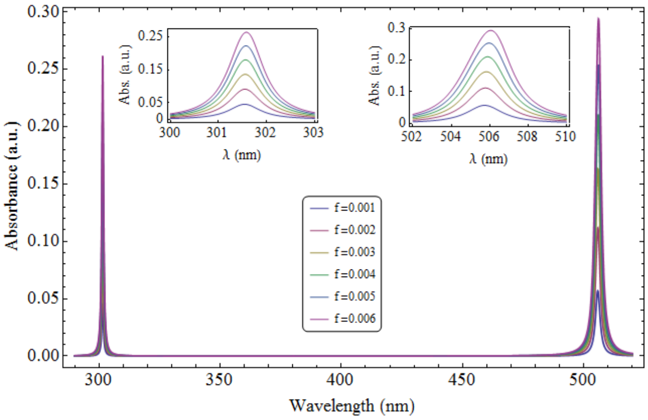

Figure 3.8: The absorbance versus wavelength for different values of metal fraction, f; with $\beta = 0.65$, $r_2 = 30\ nm$ and $\varepsilon_h = 1.77$.

by [120]. The inset highlights the set of peaks located around $\lambda = 300\ nm$.

3.6 Conclusions

In this chapter, we investigated the effects of changing the metal fraction, host matrix, and filling fraction on the optical properties of systems of spherical core/shell $Fe_3O_4@Ag$ nanoparticles embedded in a dielectric matrix. It is found that the real and imaginary parts of the polarizability, and refractive index as well as the optical absorbance of the system plotted for different values of β as a function of wavelength possess two sets of resonance peaks in the UV (in the vicinity of $\lambda \sim 300\ nm$) and visible (above $\lambda \sim 420\ nm$) spectral regions. These sets of peaks arise due to the coupling/interactions of the surface plasmon oscillations of silver with the semiconductor/dielectric at the inner (Fe_3O_4/Ag) and outer (Ag/host) interfaces and/or to near-field inter-particle interaction. Moreover, when β is increased, the first set of peaks in the UV region are red-shifted which is mainly attributed the decrease of the size of the semiconducting Fe_3O_4 core, while the second set of peaks are blue-shifted with an increase of β, due to an increase in the thickness of the metallic shell.

Furthermore, the graphs of the real and imaginary parts of the refractive index and absorbance as a function of wavelength for different values of host matrix (for fixed $\beta = 0.65$ and $f = 0.001$) possess two set of peaks - the first in the UV (around $\lambda \sim 300\ nm$) and the second in the visible (above $\lambda \sim 460\ nm$) spectral regions. It is found that with an increase in the permittivity ε_h of the host, n_1, n_2, and the absorbance A are enhanced accompanied. In this case, both sets of peaks are red shifted with an increase in ε_h. We also found that the increase in f enhances the peak intensity without a shift in position for all cases.

Finally, the enhancement of the optical properties of the system (spherical core/shell $Fe_3O_4@Ag$ nanoparticles embedded in a dielectric host matrix) is because of the strong coupling/ interactions of the surface plasmon oscillations of silver with the semiconductor/dielectric at the inner (Fe_3O_4/Ag)nano-core. It means that the silver nanoshell strongly modify the optical properties of Fe_3O_4 nanoparticles which correspondingly alter/modify its potential applications.

The results obtained may be utilized in device fabrication and applications that integrates the plasmonic effects of noble metals with magnetic semiconductors (e.g., Fe_3O_4) in a core/shell nanostructure.

Chapter 4

The Effect of Surface Plasmonic Resonances on Magneto-Plasmonic $Fe_3O_4@Ag$ Spherical Core-Shell Nanoparticles

4.1 Introduction

A great attention has been given to the development of nanomaterials as they exhibit unique material properties as compared to their bulk counterpart. These unique properties includes optical, magnetic, specific heat, melting point, surface activities, chemical and biological properties [133]. Nanomaterials forms heterogeneous structures composed of a noble metal and a semiconductor. These peculiar type of systems offers to design materials with novel and unique physical chemistry properties. As isolated systems, the optical properties of semiconductor quantum dots (QDs) and noble metal nanoparticles (NPs) are characterized by excitons and plasmons, respectively. In both cases, the required wavelengths to produce such excitations are governed mainly by the nanoparticle nature, size, shape, and local environment [36].

As an important class of nanomaterials, core-shell nanoparticles (NPs) that integrate two dissimilar materials with distinct functionalities have attracted more and more attention, since they have emerged at the frontier between materials chemistry and many other fields, such as biomedical, optics, catalysis. Because core-shell NPs enable the synergistic coupling of the two constituents, they could offer the modified properties by changing either the constituting materials or the core to shell ratio. Therefore, this nanostructure can meet the diverse application requirements. Among various core-shell NPs, magnetic/noble metal hybrid NPs have been widely studied as they possess intriguing magnetic/plasmonic and magnetic/catalytic properties, and they can be used in many fields, for example optical devices, chemical reactions as magnetically recyclable catalysts, bioimaging, targeted drug delivery. Ag-based magnetic hybrid NPs play an important role in specially chemistry, physics and material science. By varying the size of the Fe_3O_4 cores and Ag shell, the optical properties of nanohybrids can be tuned in a broad spectral ranges [134].

Magnetic and/or plasmonic nanostructures demonstrate multiple properties not present in individual nanomaterials. Such materials offer the advantage of being manipulated by an external magnetic field, showing tunable optical properties being adjustable in accordance with modifying shell thickness. Experimental and computational studies by [135] shows that the higher the magnetization in magnetic core nanoparticles, the more is the suitable response toward the exposed magnetic field and the higher the effectiveness in nanomedical diagnostics. Magnetic-plasmonic core shell NPs possess dual magnetic and plasmonic properties and have widespread applications in biomedical fields. The magnetic cores such as iron-oxide (IO) are greatly desired for applications such as magnetic separation, magnetic resonance imaging or magnetic guided drug delivery. The IO-cores can be chemically stabilized by coating them with noble metals, which not only provides a chemically inert surface, but also introduces interesting plasmonic properties which can be utilized for sensing, imaging, and photothermal therapy [136].

The possibility of building new nanostructures by mixing noble metals Ag and magnetic Fe_3O_4 nanoparticles (NPs) opens up a wide spectrum of desirable synergistic and complementary effects. One of the challenges is the conjunction of these two dissimilar materials in a controlled way. Thus, great efforts have been made on synthetic routes to command the bonding of the heteroparticle [137]. The plasmon resonance wavelength, light scattering, absorption and extinction cross-section of core-shell are affected by shell thickness, core diameter, electronic properties of shell and surrounding environment at outer interface between the surface and incident light, and inner interface between metal and semiconductor. Localized surface plasmon resonance gives rise to an enhancement of electric field, localization of energy at nanometer scale, and strongly enhanced absorption and scattering of light.

Magnetic nanoparticles with a core-shell structure promises for many applications due to their multi-functionality including optical, electronic, and magnetic properties [138]. In particular, these $Fe_3O_4@Ag$ core-shell NPs combine the magnetic and optical properties of Fe_3O_4 and Ag together, exhibiting great potential in the fields of bio-related separation, ultrasensitive detection and cellular imaging [134]. Fe_3O_4 (Magnetite) is one of the magnetic nanoparticles. Different reports are demonstrating that magnetic Fe_3O_4 can be used for waste water purification, such as to adsorb arsenite, arsenate, cadmium, nickel [139, 140] used to remove alkalinity and hardness, desalination, decolourization of pulp milleffluent and removal of natural organic compounds. After adsorption, Fe_3O_4 can be separated from the medium by a simple magnetic process [138].

Noble metals nanoparticles, such as Ag and Au, strongly absorb light in the visible region due to coherent oscillations of the metal conduction band electrons in strong resonance with visible frequencies of light. This phenomenon is known as surface plasmon resonance (SPR) and is highly dependent on NPs size, shape, surface, and dielectric properties of the surrounding medium. Light absorbed by nanoparticles is readily dissipated as heat. Due to their large absorption cross sections, plasmonic NPs can generate a significant amount of heat and increase temperatures in their vicinities [27], [140]-[143].

Silver NPs have been applied as a broad spectrum and highly effective bactericide. The antibacterial mechanism is associated to the release of silver ions. For medical applications, an $Ag@Fe_3O_4$ core-shell structure allows one to add a magnetic functionality to silver properties. Such nanostructure could lead to interesting advances to solve the lack of bio-compatibility of silver, eliminating its contact with tissues (iron-oxide can be considered biocompatible, at least up to the mg/ml range). However, an intriguing behavior was observed on $Ag@Fe_3O_4$ NPs: its bactericidal efficiency is stronger than $Ag - Fe_2O_3$ hetero-dimers or plain Ag [144]-[146]. Surface plasmon absorption has been observed for silver particles in various media, including aqueous solutions, gelatin and glass. Size effects exhibited by nearly spherical silver particles are similar to those for gold. While, extinction is the attenuation of an electromagnetic wave by scattering and absorption as it traverses a particulate medium. In homogeneous media the dominant attenuation mechanism is usually absorption. Comparison of extinction spectra for small particles of various sizes with absorption spectra for the bulk parent material reveals both similarities and differences [27].

To investigate the optical properties and response (absorption and scattering) of NPs with light (electromagnetic radiation) interaction, one has to measure the effective dielectrics, ϵ_{eff}, and permeability, μ_{eff}, [121]. In this chapter, we studied the effect of plasmon resonance on the theoretically modelled spherical $Fe_3O_4@Ag$ core-shell NPs. Silver nanoparticle was selected as a shell on magnetite nanospheres, due to its nontoxic, strong absorption in the UV and visible spectrum [122] and surface plasmon resonance (SPR) which plays a great role in determining the optical response of nanoparticles. The chapter is structured as follows: In Section 5.2, the effective dielectrics and permeability of the theoretically modelled magnetic-semiconductor/metal core-shell spherical NPs embedded in a dielectric host matrix are derived. In Section 5.3, equations for the effective polarizabilities, absorption cross-section and scattering cross-section are derived. The numerical results are presented and discussed in Section 5.4. Detailed analysis of the effect of plasmonic resonance on $Fe_3O_4@Ag$ core-shell NPs, namely the absorption cross-section, scattering cross-section and extinction cross-section are presented. Finally, concluding remarks are presented in Section 5.5.

4.2 Theoretical Model

In this chapter, we considered a model of $Fe_3O_4@Ag$ spherical core-shell NPs, which is composed of Magnetic-half metallic iron (III) oxide (Fe_3O_4) core of radius a_c and an outer metallic (Ag) shell of radius a_s embedded in a dielectric host matrix as shown in Fig. 4.1, where $a_c < a_s$. Because of the core material is magnetic with permeability, $\mu \gg 1$, the magneto-optical properties of the system requires determination of its effective permittivity ε_{eff} and permeability μ_{eff}. Based on electrostatic approximation and the Maxwell-Garnet effective medium theory, theoretical analysis have been done to derive ε_{eff} and μ_{eff}. Moreover, using these theoretically determined values, calculations has been done on the magneto-optical parameters such, as the electric polarizability, absorption and scattering cross-sections.

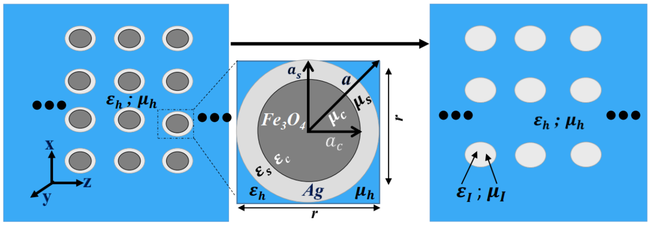

Figure 4.1: Schematic of a core-shell spherical NPs embedded in a matrix. The permittivities and permeabilities are ε_c, μ_c for the core, ε_s, μ_s for the shell, and, ε_h, μ_h for the host matrix, respectively. Also, a_c, a_s are the radii of the core and the shell, $r = 2a$ is the diameter of core/shell, and a is the distance from the center of the NP to an observation point.

4.3 Optical Properties of $Fe_3O_4@Ag$ Nanoparticles

In this section, we present the equations for the optical parameters, i.e., the absorption, scattering, and extinction cross-sections with the help of the polarizability equations for a system composed of $Fe_3O_4@Ag$ core-shell NPs embedded in a liquid/water medium. Hence, in order to get an explicit expression for the absorption and scattering cross-sections, we must fix the permittivities and effective electric and magnetic polarizabilities of the system that consists of the magnetic core, metallic shell, and host matrix.

Recalling Eqn.(3.3.4), the corresponding electric polarizability becomes

$$\alpha_e = 4\pi a_s^3 \alpha_{eff}. \tag{4.3.1}$$

And from eqn (3.3.9), the magnetic polarizability becomes

$$\alpha_m = 4\pi a_s^3 \kappa_{eff}. \tag{4.3.2}$$

4.3.1 Absorption, Scattering, and Extinction Cross-Sections

The absorption cross-section, σ_{abs}, of the system consisting of spherical core-shell composite NPs embedded in a host matrix is given by [54]:

$$\sigma_{abs} = k\ Im[\alpha_e + \alpha_m], \tag{4.3.3}$$

where $k = 2\pi\sqrt{\varepsilon_h}/\lambda$. Note that α_m is a real constant.

In addition, we consider that the loss of electromagnetic wave upon propagation through the spherical nanoinclusions results by means of the generation of heat and scattering. The scattering cross-section, σ_{sc}, of the system can be shown to have the following form:

$$\sigma_{sc} = \frac{k^4}{6\pi} \mid \alpha_e + \alpha_m \mid^2 . \tag{4.3.4}$$

Furthermore, the extinction cross-section, σ_{ext}, of the system is given by

$$\sigma_{ext} = \sigma_{sc} + \sigma_{abs}, \tag{4.3.5}$$

where σ_{sc} and σ_{abs} are given by Eqs. (4.3.3) and (4.3.4), respectively.

4.4 Numerical Analysis

Next, we numerically analyzed the polarizability as well as the absorption, scattering, and extinction cross-sections of the theoretically modelled spherical $Fe_3O_4@Ag$ core-shell NPs embedded in a dielectric host matrix. These optical parameters are analyzed by varying the material parameters β and ε_h). For the numerical evaluations, we used *Mathematica version 10* software. The following parameter values are used in the simulation: $\varepsilon_\infty = 4.5$, $\omega_p = 1.46 \times 10^{16}\ rad/s$ and $\gamma = 1.67 \times 10^{13}\ rad/s$ for the silver shell; and $\varepsilon_c = 5.85$ and $\mu_c = 9.0$ for magnetite.

4.4.1 Electric Polarizability

Figure 4.2 depicts the real and imaginary parts of the frequency dependent complex electric polarizability (α'_{eff} and α''_{eff}) of the spherical $Fe_3O_4@Ag$ nanoinclusions as a function of the wavelength of the incident radiation for different values of the metal fraction, β, and fixed values of $\varepsilon_h = 1.77$ and NPs size $a_s = 10\ nm$. It is shown that

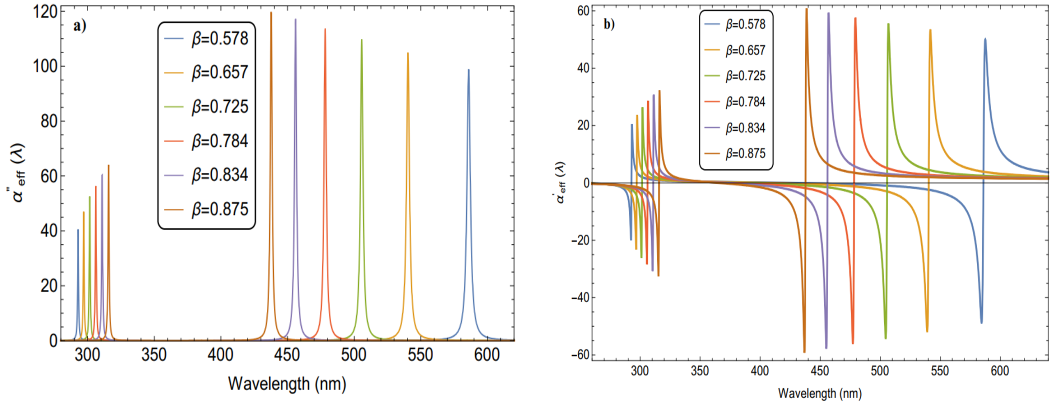

Figure 4.2: The real a) and imaginary b) parts of the electric polarizability versus wavelength for different values of β; with $\varepsilon_h = 1.77$ and $a_s = 10\ nm$.

both α'_{eff} and α''_{eff} possess two sets of resonance peaks - the first in the UV region in the vicinity of the wavelength $\lambda = 300\ nm$ and the second peaks in the visible spectral region above the wavelength of $\lambda = 430\ nm$. The first set of peaks for both real and imaginary parts are blue shifted as β decreases and second sets of peaks are red shifted as β decreases. The first and second sets of peaks arise due to the coupling of the surface plasmon oscillations of the silver shell at the inner semiconductor/metal (Fe_3O_4/Ag) interface and outer (Ag/host matrix) interface, respectively.

Furthermore, it is found that the values of both $\alpha_{eff}^{'}$ and $\alpha_{eff}^{''}$ increases as the value of the core radius a_c is decreased (or equivalently as the metal fraction β is increased). Besides, the first set of resonance peaks are less intense than the second set of peaks. This may be explained with the fact that the surface area of the outer surface (Ag/host matrix interface) of the Ag shell is larger than that of the inner surface area (magnetite/Ag interface), and hence large number of carriers available at the outer interface than the inner.

Moreover, the analysis shows that when β is increased, the first set of peaks in the UV region are red-shifted which is mainly attributed to the decrease of the size of the NPs, i.e., the semiconducting Fe_3O_4 core. Conversely, the second set of peaks are blue-shifted when β is increased, due to an increase in the thickness of the metallic shell. Certainly, the two resonance peaks corresponding to each NPs become closer and closer to each other as β is increased indicating that the metallic shell plays the dominant role in determining both the real and imaginary parts of the electric polarizability.

Similarly, the graphs of $\alpha_{eff}^{'}$ and $\alpha_{eff}^{''}$ as a function the wavelength of the incident EMW for the spherical nanoinclusions for different values of dielectric function of the host, ε_h and fixed values of $\beta = 0.725$ and $a_s = 10$ nm are shown in Fig. 4.3. From the figures it is obvious that both $\alpha_{eff}^{'}$ and $\alpha_{eff}^{''}$ possess two set of resonance peaks - the first in the UV region in the vicinity of the wavelength $\lambda = 300$ nm and the second peaks in the visible spectral region above the wavelength of $\lambda = 450$ nm. The

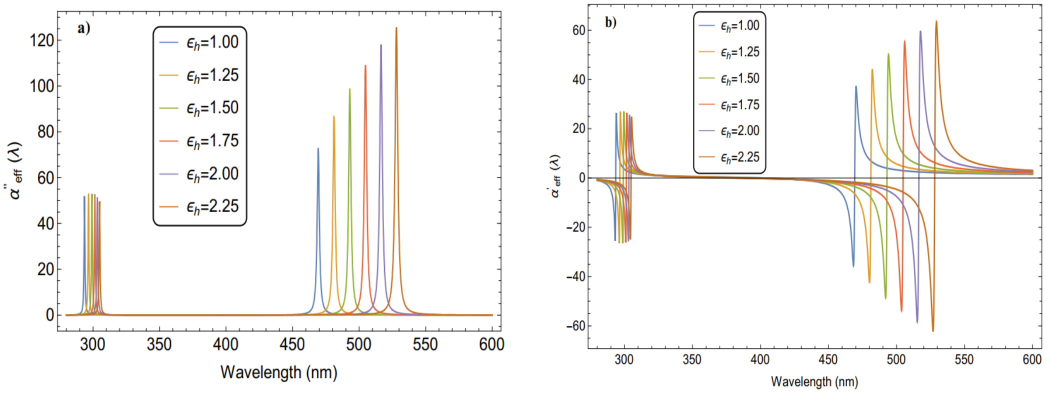

Figure 4.3: The real a) and imaginary b) parts of the electric polarizability versus wavelength for different values of ε_h; with $\beta = 0.725$ and $a_s = 10\ nm$ fixed constant.

first and second sets of peaks are red-shifted as ε_h increases.

Likewise, it is found that the polarizabilities, $\alpha^{'}_{eff}$ and $\alpha^{''}_{eff}$, increases in the second set of peaks, while no significant change take place in the first set of resonance peaks as the value of the ε_h increases. Note also that when ε_h is increased, the two sets of resonance peaks get far apart each other, for both the real and imaginary parts of the polarizability.

4.4.2 Absorption and Scattering Cross-Section

The absorption cross-section of $Fe_3O_4@Ag$ core-shell spherical nanoinclusions are numerically analyzed using Eq. (4.3.3) together with the corresponding expressions for α_e and α_m, i.e., Eqs. (4.3.1) and (4.3.2). The absorption cross-section (σ_{abs}) of the spherical nanoinclusions as a function of the wavelength of the incident EMW for different values of β and ε_h as shown in the Figs. 4.4a) and b). The graphs possess two sets of resonance peaks - the first set of peaks in both cases are located in the vicinity of $\lambda = 300\ nm$ in the UV region which are attributed to the interaction at the inner (Fe_3O_4/Ag) interface. The second set of peaks are found above the wavelength of $\lambda = 450\ nm$ all in the visible spectral region, which corresponds to the resonances at the outer (Ag/host) interface. As β increases, the two sets of peaks get far apart from each other accompanied with a spectral shift towards lower wavelengths in the first set of peaks and shifted to the higher wavelengths in the second set of peaks (see Fig. 4.4a)). The peak values of σ_{abs} are found to be more pronounced in the second set of peaks than the first set of peaks.

As it's seen from the graphs, the effect of a rapid onset of strong absorption, occurring in the UV regions for all dielectric medium/host ε_h, is dependent on the particles size. That is, when the value of β is increased, the absorption peaks sharply drops (less intense) for both the first and second peaks (see Fig. 4.4a) for a constant $\varepsilon_h = 1.77$. On the other hand, for a particular value of $\beta = 0.725$, the absorption cross-section for both the first and second sets of peaks sharply increases as ε_h increases and red-shifted as shown in Fig. 4.4b.

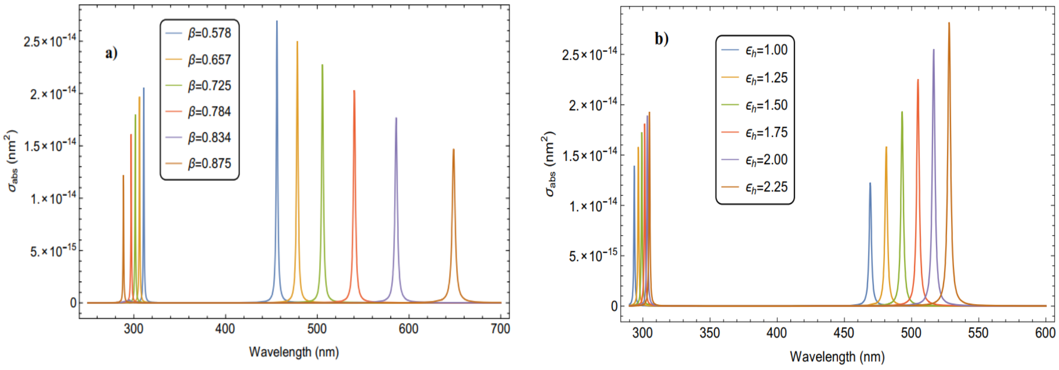

Figure 4.4: The absorption cross-section versus wavelength a) for different values of β and b) for different values of ε_h; with $f = 0.003$ and $a_s = 10\ nm$.

Figures 4.5a and 4.5b depict the scattering cross-section as a function of the wavelength of the incident EMWs for different values of β and ε_h. In each figures there are two sets of resonance peaks. The first set of resonance peaks positioned near to $\lambda = 300\ nm$ in the UV region and is associated with the inner (magnetite/Ag) interface. The second set of peaks which are connected to Ag/host interface are located above the wavelength of $\lambda = 450\ nm$ all in the visible spectral region. Figure (4.5a illustrate that, scattering of light is sharply increased (more scattering takes place) in the first set of peaks than the second set of peaks and gets sharply decreased as β increases. Furthermore, the two sets of peaks increases as ε_h increases as shown in the Fig. 4.5b. From both Figs. 4.5a and b, it is observed that the first resonance peaks are more pronounced than the second set of peaks. As the size of the system of core/shell nanoparticles gets smaller and smaller, the metal fraction, β, is also decreased. This leads to the decrease in the scattering cross-sections.

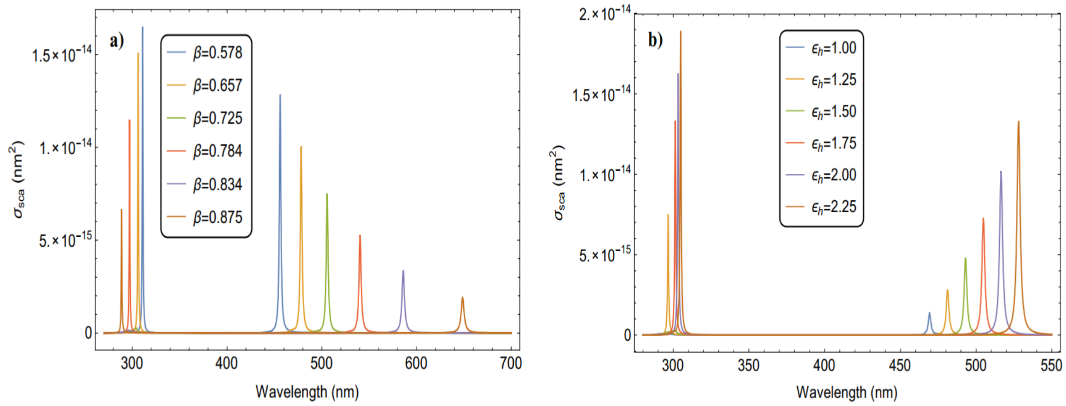

Figure 4.5: The scattering cross-section as a function of wavelength a) for different values of β and b) for different values of ε_h; with fixed values of $f = 0.003$ and $a_s = 10\ nm$.

In Fig. 4.5a, the two sets of resonances gets closer each other as β decreases accompanied by the shift towards the higher energy in the second peaks and emission spectral shift to lower energy in the first peaks. Both sets of resonance peaks are red-shifted (see Figs. 4.5) as ε_h increased. For both figures 4.5a and b there are no noticeable peaks found in the first sets of peaks at particular values $\beta = 0.725$ and at $\varepsilon_h = 1.50$. This may be due to the fact that, the absorption is more likely to dominate over scattering processes at the particular values of $\beta = 0.725$ and at $\varepsilon_h = 1.50$. On the other hand, the dielectric medium at the value of $\varepsilon_h = 1.50$ in the host matrix may affect the propagation of the incident electromagnetic wave.

4.4.3 Extinction Cross-Section

Figures 4.6 depict the graphs of extinction cross-section, σ_{ext} as a function of wavelength for different values of β and ε_h for the spherical nanoinclusions. As it is seen from the graphs, the extinction cross-section possess two sets of resonance peaks. The first set of peaks for Figs. 4.6a and b, the resonance peaks are located close to $\lambda = 300\ nm$ in the UV region and the first set of peaks are due to resonances at the inner (magnetite/Ag) interface. The second set of peaks are those found above the wavelength of about $\lambda = 450\ nm$ all in the visible spectral region.

As Fig. 4.6a) depicts, the two sets of resonances gets closer to each other as β is decreased and the spectra shift towards lower frequencies in the first set of peaks, and shift toward higher frequencies for the second set of peaks. Both sets of resonance peaks are red-shifted (see Fig. 4.6 b) as ε_h is increased.

The extinction cross-section depends on the chemical composition of the particles, their size, shape, orientation, the surrounding medium, the number of particles, and the polarization state and frequency of the incident EMWs [27]. The system of spherical core/shell nanoparticles that is considered in this study is composed of two

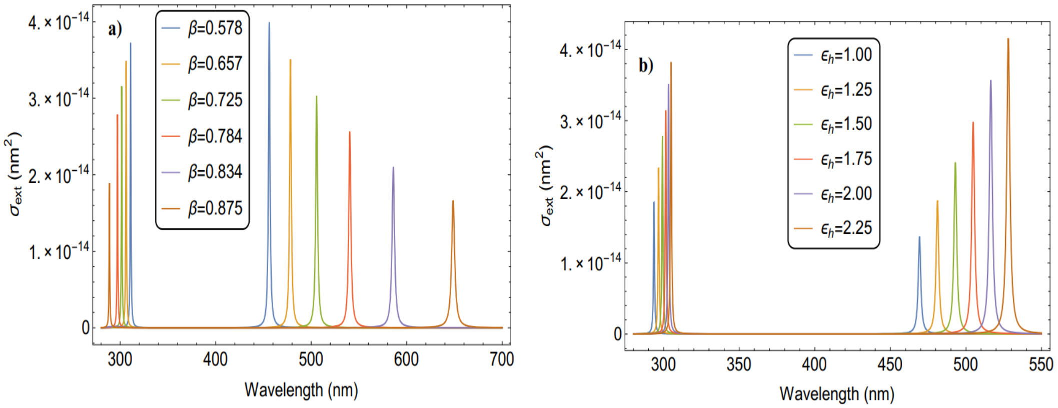

Figure 4.6: The extinction cross-section versus wavelength for different values of a) β and b) ε_h; with fixed values of $f = 0.003$ and $a_s = 10\ nm$.

chemically dissimilar nanoparticles - one as the semiconducting core and the other as a plasmonic shell. We found that the extinction cross-section is dependent on the size and chemical composition of the semiconducting core or the metallic shell.

4.5 Conclusion

In this study, we investigated the effects of varying parameters like the metal fraction and host matrix on the systems of spherical core/shell $Fe_3O_4@Ag$ nanoparticles embedded in a dielectric host matrix. It is found that the real and imaginary parts of the polarizability, absorption cross-section, scattering cross-section as well as the extinction cross-section of the system plotted for different values of β and ε_h as a function of wavelength possess two sets of resonance peaks in the UV (in the vicinity of $\lambda \sim 300\ nm$) and visible (above $\lambda \sim 450\ nm$) spectral regions. These sets of peaks arise due to the coupling of the surface plasmon oscillations of silver with the energy gap of the semiconducting core at the inner (Fe_3O_4/Ag) interface and at the outer metal/dielectric (Ag/host matrix) interface. Moreover, when β is increased, the first set of peaks in the UV region are which is mainly attributed the decrease of the size of the semiconducting Fe_3O_4 core, while the second set of peaks are blue-shifted with an increase of β, due to an increase in the thickness of the metallic shell for the graphs of the real and imaginary parts of the polarizability. On the contrary, for absorption and scattering cross-sections the resonance peaks are shifted towards higher frequencies in the first peak and red-shifted for the second set of peaks as β increases.

Furthermore, the graphs of the real and imaginary parts of the polarizability as a function of wavelength for different values of the dielectric function of the host matrix (for fixed $\varepsilon_h = 1.77$) possess two set of peaks - the first in the UV (around $\lambda \sim 300\ nm$) and the second in the visible (above $\lambda \sim 420\ nm$) spectral regions. It is found that with an increase in the permittivity ε_h of the host, the resonance peaks of σ_{abs}, σ_{sc} and σ_{ext} are enhanced accompanied with a red or blue shift. In this case, both sets of peaks are shifted to higher wavelength with an increase in ε_h.

Finally, the enhancement of the optical properties of the system is because of the strong coupling of the surface plasma oscillations of the silver shell with the energy gap of the magnetic semiconducting ($Fe_3O_4@Ag$) nano-core. It means that the silver nanoshell strongly modifies the optical properties of Fe_3O_4 nanoparticles which correspondingly modify its potential applications. The results obtained may be utilized in device fabrication and applications that integrates the plasmonic effects of noble metals with magnetic semiconductors such as Fe_3O_4 in core/shell nanostructures.

Chapter 5

Summary of Conclusions and Future Work

5.1 Summary of Conclusions

In this thesis work, we investigated the surface plasmonic resonance effects of varying various parameters such as the metal fraction, filling factor and the dielectric function of the host matrix on the systems of spherical core/shell $Fe_3O_4@Ag$ nanoparticles embedded in a dielectric host matrix. In addition to this, the enhancement of optical response of spherical $Fe_3O_4@Ag$ core-shell nanoparticles were studied based on electrostatic approximation and the Maxwell-Garnet effective medium theory to obtain ε_{eff} and μ_{eff}. The effects of the above mentioned parameters and the enhancement in its Magneto-plasmonic properties of systems of core/shell $Fe_3O_4@Ag$ spherical nanoparticles embedded in a dielectric host matrix were investigated theoretically and numerically.

Moreover, using these theoretically determined values, calculations has been done on the magneto-optical parameters such, as the electric and magnetic polarizability, the refractive index, an optical absorbance and the extinction cross-sections as well as the scattering cross-sections of the modeled core-shell NPs. It is found that the real and imaginary parts of the polarizability, refractive index, optical absorbance, absorption cross-section, scattering cross-section as well as the extinction cross-section of the system plotted by varying the parameters such as metal fraction (β) filling factor f and dielectric function of the host matrix (ε_h) as a function of wavelength possess two sets of plasmon resonance peaks in the UV (in the vicinity of $\lambda \sim 300\ nm$) and visible (above $\lambda \sim 450\ nm$) are observed in the spectral regions. By varying these parameters, The two sets of plasmon resonance peaks are observed. These sets of peaks arise due to the coupling/interactions of the surface plasmon oscillations (collective oscillation of surface electrons) of silver with the semiconductor/dielectric at the inner (Fe_3O_4/Ag) and outer (Ag/host) interfaces and/or to near-field interparticle interaction.

Additionally, the graphs of the real and imaginary parts of the polarizability as a function of wavelength for different values of metal fraction β and the dielectric function of the host matrix (for fixed $\varepsilon_h = 1.77$) possess two set of peaks - the first in the UV (around $\lambda \sim 300\ nm$) and the second in the visible (above $\lambda \sim 420\ nm$) spectral regions. when β is increased, the first set of peaks in the UV region are are red-shifted which is mainly attributed the decrease of the size of the semiconducting Fe_3O_4 core, while the second set of peaks are blue-shifted with an increase of β, due to an increase in the thickness of the metallic shell for the graphs of the real and imaginary parts of the polarizability. On the contrary, for absorption and scattering cross-sections the resonance peaks are shifted towards higher frequencies in the first peak and red-shifted for the second set of peaks as β increases.

Furthermore, It is found that with an increase in the permittivity ε_h of the host, the resonance peaks of σ_{abs}, σ_{sc} and σ_{ext} are enhanced accompanied with a red or blue shift. In this case, both sets of peaks are shifted to higher wavelength with an increase in ε_h. Likewise, the graphs of the real and imaginary parts of the refractive index and absorbance as a function of wavelength for different values of host matrix (for fixed $\beta = 0.65$ and $f = 0.001$) possess two set of peaks - the first in the UV (around $\lambda \sim 300\ nm$) and the second in the visible (above $\lambda \sim 460\ nm$) spectral regions. It is found that with an increase in the permittivity ε_h of the host, n_1, n_2, and the absorbance A are enhanced accompanied. In this case, both sets of peaks are red shifted with an increase in ε_h. We also found that the increase in f enhances the peak intensity without a shift in position for all cases.

Lastly, the effect of surface plasmonic resonance and the enhancement of the magneto-optical response on the system (spherical core/shell $Fe_3O_4@Ag$ nanoparticles embedded in a dielectric host matrix) is because of the strong coupling/ interactions of the surface plasmon oscillations (collective oscillation of surface electrons) of silver with the energy gap of the magnetic semiconductor/dielectric (Fe_3O_4/Ag)nanocore at the inner and/or to near-field inter-particle interaction. Coating a magnetite nano core with noble metals allows the magnetite QD to interact with the surface plasmon oscillation induced by radiation. When the frequency of radiation is close to the surface plasmon frequency of the coated metal, the local surface plasmon resonance occurs. Optical properties and enhanced optical-tunability of core/ shell nanoparticles (NPs) are determined by shape, size, permittivity, and geometrical arrangement of building blocks.

The modification of the spectral shape of the MO response of $Fe_3O_4@Ag$ can be directly ascribed to the excitation of a plasmonic resonance in the MO material. In particular, it is now understood that is the interplay between the amplitude and phase of the plasmonic resonance and to those of the MO coupling (spin-orbit coupling) of the magnetic material that gives rise to enhancements. It means that the silver nanoshell strongly modify the optical properties of Fe_3O_4 nanoparticles which correspondingly alter/modify its potential applications. The results obtained may be utilized in device fabrication and applications that integrates the plasmonic effects of noble metals with magnetic semiconductors such as Fe_3O_4 in core/shell nanostructures.

5.2 Future Work

The plasmonic and optical properties of magneto-optical core-shell composite nanostructures are not only dependent on the core size, shell thickness, composite size, and host medium, but also depend on the material of the constituents, elastic properties, number of layer, and core shape. In addition, the mechanical properties of various types of composite nanostructures are the several topics that remain unsolved problems need to be further investigations. Thus, the following points are our future work :

- magnetic and Plasmonic response of $Fe_3O_4@Ag$ core-shell spherical, spheroidal, and cylindrical composite nanostructures.
- The effect of shape, host medium and number of layers on the magneto-optical properties of $Fe_3O_4@Ag$ based composite nanoparticles.
- Stress/Strain effect on magnetic/plasmonic multilayered $Fe_3O_4@Ag$ core-shell nanostructures.

- Strain effects on the SERS enhancements for Ag/Fe_3O_4/Au Core@shell spherical Nanoparticles are among the list of future works.

5.3 Publications

1. Kinde Yeneayehu, Teshome Senbeta, and Belayneh Mesfin, *Enhancement of the Optical Response of Fe_3O_4/Ag Core-shell Nanoparticles*, Physica E: Low-dimensional Systems and Nanostructures, **134**, 114822, (2021).

2. Kinde Yeneayehu, Teshome Senbeta, and Belayneh Mesfin, *The Effect of Surface Plasmonic Resonances on Spherical Magneto-Plasmonic Fe_3O_4@Ag Core-Shell Nanoparticles*, SINET Ethiopian Journal of Science **45(2)**: 132 _ 142 (2022). DOI:10.4314/sinet.v45i2.2

Bibliography

[1] Kathy Lu, Navin Manjooran, Miladin Radovic, Eugene Medvedovski, Eugene A. Olevsky, Chris Li, Gurpreet Singh, Nitin Chopra, Gary Pickrell, *Advances in Nanomaterials and Nanostructures*, John Wiley & Sons, Inc., Volume 229 (2011).

[2] Sudha, Parappurath N. *Emerging Applications of Nanoparticles and Architecture Nanostructures Nanomaterials history, classification, unique properties, production and market*, 341-384. (2018).

[3] C. F. Bohre and D. R. Huffman, *Absorption and Scattering of Light by Small Particles* JohnWiley and Sons, New York, (1983)

[4] D. Aaron R. Barkhouse, Richard Haight, Noriyuki Sakai, Homare Hiroi, Hiroki Sugimoto, and David B. Mitzi, *Cd-free buffer layer materials on* $Cu_2ZnSn(S_xSe_{1-x})_4$*: Band alignments with ZnO, ZnS, and* In_2S_3, Appl. Phys. Lett. 100, 193904 (2012)

[5] R. R. LaPierre, A. C. E. Chia, S. J. Gibson, C. M. Haapamaki, J. Boulanger, R. Yee, P. Kuyanov, J. Zhang, N. Tajik, N. Jewell, and K. M. A. Rahman, *IIIV nanowire photovoltaics: Review of design for high efficiency*, Phys. Status Solidi RRL 7, 815 (2013)

[6] P. Fan, U. K. Chettiar, L. Cao, F. Afshinmanesh, N. Engheta, and M. L. Brongersma, *An invisible metalsemiconductor photodetector*, Nature Photon. 6, 380-385 (2012)

[7] S. Z. Oener, S. A. Mann, B. Sciacca, C. Sfiligoj, J. Hoang, and E. C. Garnett, *$Au - Cu_2O$ core-shell nanowire photovoltaics*, Appl. Phys. Lett. 106, 023501 (2015)

[8] S. A. Mann and E. C. Garnett, *Extreme light absorption in thin semiconductor films wrapped around metal nanowires*, Nano Lett. 13, 3173-3178, 120 (2013)

[9] Nucharee Chomchoey, Darunee Bhongsuwan and Tripob Bhongsuwan, *Magnetic Properties of Magnetite Nanoparticles Synthesized by Oxidative Alkaline Hydrolysis of Iron Powder*, Kasetsart J. (Nat. Sci.) **44** : 963-971 (2010).

[10] Amin, Dr. Gul, *ZnO and CuO Nanostructures: Low Temperature Growth, Characterization, their Optoelectronic and Sensing Applications*, Disertation, p 1 - 2, (2012).

[11] Compen-Jasso, Facundo Ruiz, J.R. Martnez, A. Herrera-Gmez *Magnetic properties of magnetite nanoparticles synthesized by forced hydrolysis*, Materials Letters **62** 42484250,(2008).

[12] Jerome Alexander Cuenca, Keith Bugler, Stuart Taylor, David Morgan, Paul Williams, Johann Bauer and Adrian Porch, *Study of the magnetite to maghemite transition using microwave permittivity and permeability measurements*, J. Phys. Condens. Matter **28** 106002 (2016).

[13] M. A. Ramazanov, A. M. Maharramov, R. A. Ali-zada, H. A. Shirinova, F. V. Hajiyeva, *Theoretical and experimental investigation of the magnetic properties of polyvinylidene fluoride and magnetite nanoparticles-based nanocomposites*, Journal of Theoretical and Applied Physics, (2018).

[14] Ian Y. Goon, Leo M. H. Lai, May Lim, Paul Munroe, J. Justin Gooding, and Rose Amal, *Fabrication and Dispersion of Gold-Shell-Protected Magnetite Nanoparticles: Systematic Control Using Polyethyleneimine*, Chem. Mater., 21, 673681, (2009).

[15] H.E Ghandoor, H. M. Zidan, Mostafa M.H. Khalil and M. I. M. Ismail, *Synthesis and Some Physical Properties of Magnetite (Fe_3O_4) Nanoparticles*, Int. J. Electrochem. Sci., **7** 5734 - 5745 (2012).

[16] Chun-Rong Lin, Yuan-Ming Chu, Sheng-Chang Wang, *Magnetic properties of magnetite nanoparticles prepared by mechanochemical reaction*, Materials Letters **60** 447450 (2006).

[17] Z. vindrycha;b, A. Youssefb and Z. Janu, *Link between Magnetic and Dielectric Properties in Magnetite*, Acta Physica Polonica A, Vol. **118** No. 5 (2010).

[18] K. Persson, *Materials Data on Fe_3O_4*, Materials Project, Data set, LBNL Materials Project, Lawrence Berkeley National Laboratory, Berkeley, California (2015).

[19] Prabhash Prasannan Geetha, Ajith Ramachandran, Swapna S. Nair, *Tuning of localized surface plasmon resonance in copper-copper oxide core-shell quantum dots for the application in biosensors*, (2020).

[20] Panuwat Chaiyachate, Artit Chingsungnoen and Thananchai Dasri, *Theoretical Calculation of the Optical Properties of Dielectric Material @ Noble Metal Core-Shell Composite Nanoparticles*, Indian Journal of Science and Technology, Vol **10**(13),(2017).

[21] Shiang-Feng Tang1, Tzu-Chiang Chen, Shih-Yen Lin and Hsing-Yuan Tu, *Intersubband Transitions in the Quantum Dot Layers for Quantum Confined Photodetector*, Indian Journal of Science and Technology, Chapter (02), June, (2014).

[22] Luis J. Mendoza Herrera, David Muñeton Arboleda, Daniel C. Schinca, and Lucia B. Scaffardi *Determination of plasma frequency, damping constant, and size distribution from the complex dielectric function of noble metal nanoparticles* , Journal of Applied Physics **116**, 233105, (2014)

[23] João Conde, Gonçalo Doria, and Pedro Baptista, *Noble Metal Nanoparticles Applications in Cancer*, Journal of Drug Delivery,(2012).

[24] Panuwat Chaiyachate, Thananchai Dasri and Artit Chingsungnoen,*Theoretical calculation of the optical absorption property of nanoparticles composed of an Au Core and Si shell embedded in silica*, Mater. Res. Express **7** 015072, (2020)

[25] K. Santhosh Kumar, Vijay Bhooshan Kumar, and Pradip Paik, *Recent Advancement in Functional Core-Shell Nanoparticles of Polymers: Synthesis, Physical Properties, and Applications in Medical Biotechnology*, Journal of Nanoparticles, Volume (2013).

[26] Zhiyong Fan, Rehan Kapadia, Paul W. Leu, Xiaobo Zhang, Yu-Lun Chueh, Kuniharu Takei, Kyoungsik Yu, Arash Jamshidi, Asghar A. Rathore, Daniel J. Ruebusch, Ming Wu, and Ali Javey, *Ordered array of dual-diameter nanpillars for maximized optical absorption*, Nano Lett. 10, 3823 (2010)

[27] Otto L. Muskens, Jaime Gmez Rivas, Rienk E. Algra, Erik P. A. M. Bakkers, and Ad Lagendijk, *Design of Light Scattering in nanowire materials for Photovoltaic Application*, Nano Letters. **8**, 9, 2638-2642 (2008)

[28] Craig F. Bohren and Donald R. Huffman, *Absorption and scattering of light by small particles*, (John Wiley and Sons, 1998)

[29] S. A. Maier. *Plasmonics: Fundamentals and Applications.* Springer, (2007).

[30] W.J. Yin, L. Dai, L. Zhang, R. Yang, L. Li, T. Guo, Y. Yan, *Stability, transparency, and conductivity of* $Mg_xZn_{1-x}O$ *and* $Cd_xZn_{1-x}O$*, designing optimum transparency conductive oxides*, Journal of Applied Physics 115 (2)

[31] Prabhakar, J. T., Wang, Y. S., Thomas, P. J., and O'Brien, P. *Optical properties of ZnO nanocrystals doped with Cd, Mg, Mn, and Fe ions*, Journal of Physical Chemistry B, 110(43), 21412-21415, (2006).

[32] B. U. Haq, R. Ahmed, S. Goumri Said, *Solar Energy Materials and Solar Cells*, Solar Energy Materials and Solar Cells 130 6-14, (2014).

[33] H. C. van de Hulst. *Light Scattering by Small Particles.* Dover Publications, (1981)

[34] G.B. Arfken, H.J. Weber, *Mathematical Methods for Physicists*, Elsevir Science, Ed. 6th, (2001).

[35] Uwe Kreibig and Michael Vollmer, *Optical Properties of Metal Clusters*, (Springer Series in Materials Science, 25), (1995).

[36] Ezequiel R. Encina, Manuel A. Perez, Eduardo A. Coronado, *Synthesis of Ag@ZnO core/shell hybrid nanostructures: an optical approach to reveal the growth mechanism*, Journal of Nanoparticle Research. **15:1688** (2013).

[37] Stephan Link and Mostafa A. El-Sayed, *Spectral Properties and Relaxation Dynamics of Surface Plasmon Electronic Oscillations in Gold and Silver Nanodots and Nanorods*, J. Phys. Chem. B 103, 8410-8426 (1999).

[38] Anatoly V. Zayats, Igor I. Smolyaninov, Alexei A. Maradudin, *Nano-optics of surface plasmon polaritons*, Physics Reports 408, 131-314 (2005).

[39] S. Ramadurgam and C. Yang, *Semiconductor-Metal-Semiconductor Core-Multishell Nanowires as Negative-Index Metamaterial in Visible Domain*, Scientific Reports 4, 1 (2014).

[40] W. Liu, A. E. Miroshnichenko, R. F. Oulton, D. N. Neshev, O. Hess, and Y. S. Kivshar, *Scattering of core-shell nanowires with the interference of electric and magnetic resonances*, Opt. Lett. 38, 2621-2624 (2013).

[41] Zi-Qiang Cheng, Yu-Ting Zhong, Fan Nan, Jia-Hong Wang, Li Zhou, QuQuan Wang, *Plasmonic near-field coupling induced absorption enhancement and photoluminescence of silver nanorod arrays*, J. Appl. Phys. 115, 224302 (2014)

[42] Kyung Yong Ko, Hyemin Kang, Jungkil Kim, Woo Lee, Hee Sung Lee, Seongil Im, Ji Yeon Kang, Jae-Min Myoung, Han-Gil Kim, Soo-Hyun Kim, Hyungjun Kim, *High efficiency* $n-ZnO/p-Si$ *coreshell nanowire photodiode based on*

well-ordered Si nanowire array with smooth surface, Materials Science in Semiconductor Processing, 27, 297-302 (2014)

[43] Jingnan Cai, Yasuhiko Ishikawa, and Kazumi Wada, *Strain induced bandgap and refractive index variation of silicon*, Opt. Express 21, 7162-7170, (2013)

[44] J. D. Jackson, *Classical electrodynamics*, (John Wiley, New York, 1999)

[45] Leta Jule, Vadim Malnev, Belayneh Mesfin, Teshome Senbeta, Francis Dejene, and Kittessa Roro, *Fano-like resonance and scattering in dielectric(core)metal(shell) composites embedded in active host matrices*, Phys. Status Solidi B 252, 2707 (2015)

[46] Leta T. Jule, *Theoretical and experimental study of core-shell structured ZnO/ZnS and growth mechanism of un-doped and doped ZnO nanomaterials*, thesis, University Of The Free State Republic Of South Africa, (2016).

[47] R.Paniagua Dominguez, D. R. Abujetas, L. S. Froufe Perez, J. J. Saenz, J. A. Sanchez Gil, *Impedance-Matched, Double-Zero Optical Metamaterials Based on Weakly Resonant Metal Oxide Nanowires*, Photonics 5(2):7 (2018)

[48] A. D. Kondorskiy, K.S. Kislov, N.T. Lam, V.S. Lebedev, *Absorption of light by hybrid metalorganic nanostructures of elongated shape*, J. Russian Laser Res. 36(2), 175-192 (2015)

[49] Challa S.S.R. Kumar, *UV-Vis and PL Spectroscopy for Nanomaterials Characterizations*, Springer-Verlag Berlin Heidelberg, pp. 6, 240 (2013).

[50] R.B.M. Schasfoort and Anna J. Tudos University of Twente, Enschede, *Handbook of Surface Plasmon Resonance*, The Netherlands, The Royal Society of Chemistry 2-15 (2008).

[51] Prashant K. Jain, Xiaohua Huang, Ivan H. El-Sayed, And Mostafa A. El-Sayed, *Noble Metals on the Nanoscale: Optical and Photothermal Properties and Some Applications in Imaging*, Sensing, Biology, and Medicine

[52] Raether H, Heitmann D and Pockrand I, *Surface plasmons on smooth and rough surfaces and on gratings* Verlag: Springer, (1998)

[53] Barnes W, Dereux A and Ebbesen T, *Surface plasmon subwavelength optics*, Nature 424, 824-830, (2003).

[54] Clapp R, Medintz L, Mattoussi H. *Förster resonance energy transfer investigations using quantum-dot fluorophores.*, Chem phys chem. 7(1), 47-57, (2006).

[55] K. Bagga, D. F. Brougham, T. E. Keyes and D. Brabazon, *Magnetic and noble metal nanocomposites for separation and optical detection of biological species*, Phys. Chem. Chem. Phys., **17**, 27968-27980, (2015)

[56] Dab Chahinez, Thomas Reji and Ruediger Andreas, *Modeling of the surface plasmon resonance tunability of silver/gold coreshell nanostructures*, RSC Adv., 8, 19616,(2018)

[57] Xiangyang Liu, Shun Wang, Jingwei Zhang, Jiwei Zhang, Yuzong Gu, *Photoelectric properties and charge dynamics in ZnO nanowires/*$Cu_4Bi_4S_9$ *and ZnO nanowires/*In_2O_3/Cu_4Bi_4S9 *heterostructures* J. Appl. Phys. 116, 245101 (2014)

[58] G. Grzela, R. Paniagua-Domnguez, T. Barten, Y. Fontana, J. A. Snchez-Gil, and J. G. Rivas, *Nanowire antenna emission*, Nano Lett. 12, 5481-5486 (2012)

[59] Tuniz, Alessandro, Boris T. Kuhlmey, Parry Y. Chen, and Simon C. Fleming. *Weaving the invisible thread: design of an optically invisible metamaterial fibre.* Optics express 18, no. 17 18095-18105, (2010).

[60] Pavan Kumar Kasanaboina, Estiak Ahmad, Jia Li, C. Lewis Reynolds Jr., Yang Liu, Shanthi Iyer, *Self-catalyzed growth of dilute nitride* $GaAs/GaAsSbN/GaAs$ *core-shell nanowires by molecular beam epitaxy*, Appl. Phys. Lett. 107, 103111 132 (2015)

[61] A. Mirzaei, I. V. Shadrivov, A. E. Miroshnichenko, and Y. S. Kivshar, *Cloaking and enhanced scattering of core-shell plasmonic nanowires*, Opt. Express 21, 10454 (2013)

[62] Ron Gurwitz, Rotem Cohen, Ilan Shalisha, *Interaction of light with the ZnO surface: Photon induced oxygen breathing, oxygen vacancies, persistent photoconductivity, and persistent photovoltage*, J. Appl. Phys. 115, 033701 (2014)

[63] X. Wang, K. L. Pey, C. H. Yip, E. A. Fitzgerald, D. A. Antoniadis, *High efficiency* $n-Si/p-Cu_2O$ *core-shell nanowires photodiode prepared by atomic layer deposition of* Cu_2O *on well-ordered Si nanowires array*, J. Appl. Phys. 108, 124303 (2010)

[64] A. Kim, Y. Won, K. Woo, C.H. Kim, and J. Moon, *Highly transparent low resistance* $ZnO/Agnanowire/ZnO$ *composite electrode for thin film solar cells*, ACS Nano 7, 1081 (2013)

[65] S.K. Kim, R. W. Day, J. F. Cahoon, T. J. Kempa, K.D. Song, H.G. Park, and C. M. Lieber, *Tuning Light Absorption in Core/Shell Silicon Nanowire Photovoltaic Devices through Morphological Design*, Nano Lett. 12, 4971 (2012)

[66] S. Albaladejo, R. Gmez-Medina, L. S. Froufe-Prez, H. Marinchio, R. Carminati, J. F. Torrado, G. Armelles, A. Garca- Martn, and J. J. Senz, *Radiative corrections to the polarizability tensor of an electrically small anisotropic dielectric particle*, Opt. Express 18, 3556 (2010)

[67] Abdelilah Mejdoubi and Christian Brosseau, *Intrinsic electrostatic resonances of heterostructures with negative permittivity*, American Institute of Physics, 102, 094104 (2007)

[68] A. D. Mallorqu, F. M. Epple, D. Fan, O. Demichel, and A. Fontcuberta Morral, *Crystalline silicon solar cells with laser ablated penetrating V-grooves: Modeling and experiment*, Phys. Status Solidi A, 209, 1588 (2012)

[69] Shaobo Shi, Jianping Xu, Xiaosong Zhang, and Lan Li, *Effect of annealing on the structural and luminescent properties of ZnO nanorod arrays*, J. Appl. Phys. 109, 103508, (2011)

[70] Challa S.S.R. Kumar (Editor), *UV-VIS and Photoluminescence Spectroscopy for Nanomaterials Characterization*, (Springer, 2013).

[71] Ashfaqul Anwar Siraji and Yang Zhao, *Simple effective medium approximation with Rayleigh scattering*, Optics Letters, 1860 Vol. 42, No. 9 1 2017

[72] Jinyao Tang, Ziyang Huo1,Sarah Brittman, Hanwei Gao, and Peidong Yang, *Solution-processed coreshell nanowires for efficient photovoltaic cells*, Nature Nanotechnology 6, 568 (2011)

[73] X. H. Li, P. C. Li, D. Z. Hu, D. M. Schaadt, and E. T. Yu, *Light trapping in thin-film solar cells via scattering by nanostructured antireflection coatings.* J. Appl. Phys. 114, 044310 (2013)

[74] Rodrguez-Gonzalez B., Attouchi F., Cardinal M. F., Myroshnychenko V., Stephan O., Garca de Abajo F. J., Luis Marzan, L. M. Kociak, M. *Surface Plasmon Mapping of Dumbbell-Shaped Gold Nanorods: The Effect of Silver Coating*, Langmuir 28, 9063 (2012)

[75] Haridas Kumarakuru a, Zelalem N. Urgessa, Ezra J. Olivier, Johannes R. Botha, Andre Venter, Johannes H. Neethling, *Growth of ZnS-coated ZnO nanorod arrays on (1 0 0) silicon substrate by two-step chemical synthesis*, Journal of Alloys and Compounds 612, 154 (2014)

[76] Viktor Myroshnychenko, Jessica Rodriguez-Fernandez, Isabel PastorizaSantos, Alison M. Funston, Carolina Novo, Paul Mulvaney, Luis M. LizMarzanb, F. Javier Garcia de Abajo, *Modelling the optical response of gold nanoparticles*, Chem. Soc. Rev. 37, 1792 (2008)

[77] Abdelilah Mejdoubi and Christian Brosseau, *Intrinsic resonant behavior of metamaterials by finite element calculations*, Phys. Rev. B 74 165424 (2006)

[78] Zaiping Zeng, Christos S. Garoufalis, Andreas F. Terzis, and Sotirios Baskoutas, *Linear and nonlinear optical properties of ZnO/ZnS and ZnS/ZnO core*

shell quantum dots : Effects of shell thickness, impurity, and dielectric environment, J. Appl. Phys. 114, 023510 (2013)

[79] Yael Gutirrez, Dolores Ortiz, Rodrigo Alcaraz de la Osa, Jos M. Saiz , Francisco Gonzlez and Fernando Moreno, *Electromagnetic Effective Medium Modelling of Composites with Metal-Semiconductor Core-Shell Type Inclusions*, Catalysts, *9*, 626, (2019)

[80] Abdelilah Mejdoubi and Christian Brosseau, *Abdelilah Mejdoubi and Christian Brosseau*, J. Appl. Phys. 103, 084115 (2008)

[81] A. Mejdoubi, M. Malki, M. Essone Mezeme, Z. Sekkat, M. Bousmina, and C. Brosseau, *Optical scattering and electric field enhancement from coreshell plasmonic nanostructures*, J. Appl. Phys. 110, 103105 (2011)

[82] B. K. Meyer, H. Alves, D. M. Hofmann, W. Kriegseis, D. Forster, F. Bertram, J. Christen, A. Hoffmann, M. Straburg, M. A. Dworzak, U. Haboeck, A. V. Rodina, *Bound exciton and donoracceptor pair recombinations in ZnO*, phys. stat. sol. (b), vol. 241, pp. 231-260, (2004).

[83] David J. Griffiths, *Introduction to electrodynamics*, (Prentice Hall, New Jersey, 1999).

[84] Aijaz, A. Naqvi, Q. Baqir, Abuzar, *Investigation of the plasmon resonance of core-shell nanoparticle in near-infrared region*, 06, (2019)

[85] T.S. Moss, *Photoconductivity in the Elements*, Academic Press Inc., New York, (1952).

[86] N.M. Ravindra, Preethi Ganapathy, Jinsoo Choi *Energy gaprefractive index relations in semiconductors An overview*, Infrared Physics & Technology 50, 1, 2129, (2007)

[87] Challa S.S.R. Kumar, *UV-Vis and PL Spectroscopy for Nanomaterials Characterizations*, Springer-Verlag Berlin Heidelberg, pp. 240 (2013).

[88] Yi-Tao Long, Chao Jing, *Localized Surface Plasmon Resonance Based Nanobiosensors*, (Springer, 2014).

[89] Ada Serrano Rubio, Modified Au-Based Nanomaterials Studied by Surface Plasmon Resonance Spectroscopy: Springer Theses, (Springer, 2015).

[90] Katsuaki Tanabe, J. Chem. *Perspective: Fundamental aspects of time-dependent density functional theory*, Phys. 11, 236 (2016)

[91] Vincenzo Giannini, Antonio I. Fernandez-Domnguez, Susannah C. Heck and Stefan A. Maier, *Plasmonic nanoantennas: fundamentals and their use in controlling the radiative properties of nanoemitters*, Chem. Rev. 111, 38883912 (2011).

[92] Soren Raza, Sergey I Bozhevolnyi, Martijn Wubs and N Asger Mortensen, *Nonlocal optical response in metallic nanostructures*, J. Phys. Condens. Matter 27, 183204 (2015).

[93] K. Lance Kelly, Eduardo Coronado, Lin Lin Zhao, and George C. Schatz, *The Optical Properties of Metal Nanoparticles: The Influence of Size, Shape, and Dielectric Environment*, J. Phys. Chem. B 107, 3 (2003).

[94] Sujit Kumar Ghosh and Tarasankar Pal, *Interparticle Coupling Effect on the Surface Plasmon Resonance of Gold Nanoparticles: From Theory to Applications*, Chem. Rev. **107**, 4797 (2007).

[95] Jorge Perez-Juste, Paul Mulvaney, Luis M. Liz-Marzan, Patterning and encryption using gold nanoparticles, Int.J.Nanotechnol. Vol. 4 No. 3 215 (2007).

[96] Azim Akbarzadeh, Davood Zare, Ali Farhangi, Mohammad Reza Mehrabi, Dariush Norouzian, Synthesis and Characterization of Gold Nanoparticles by Tryptophane, American Journal of Applied Sciences 6 (4): 691-695, (2009).

[97] Brullot W., Valev V.K., Verbiest T., Magnetic-plasmonic nanoparticles for the life sciences: calculated optical properties of hybrid structures., Nanomedicine: Nanotechnology, Biology and Medicine 8, 559-568 (2012).

[98] Baptista P., Gonalo Doria, Joo Conde, Bruno Veigas, Leticia Giestas, Carina Almeida, Maria Assuno, Joo Rosa and Pedro V. Baptista, Noble Metal Nanoparticles for Biosensing Applications., Journal of drug delivery (2011).

[99] Lpez-Lorente A.I.; Simonet B.M.; Valcrcel M., Analytical Potential of Hybrid Nanoparticles, Anal. Bioanal. Chem., 399, 43-54 (2011).

[100] Nomoev A.V.; Bardakhanov S.P.; Schreiber M.; Bazarova D.G.; Romanov N.A.; Baldanov B.B.; Radnaev B.R.; Syzrantsev V.V, Structure and Mechanism of the Formation of CoreShell Nanoparticles Obtained through a One-Step Gas-Phase Synthesis by Electron Beam Evaporation., Beilstein J. Nanotechnol. 6, 874-880 (2015).

[101] Allafchian A.; Jalali S.A.H.; Bahramian H.; Ahmadvand H., *Preparation, Characterization, and Antibacterial Activity of* $NiFe_2O_4$*/Pama/*$AgTiO_2$ *Nanocomposite.*, J. Mag. Mag. Mater., 404, 14-2, (2016)

[102] R.G. Chaudhuri, S. Paria, *Core/Shell nanoparticles: classes, properties, synthesis mechanisms, characterization, and applications*, Chem. Rev. 112(4), 2373 (2012).

[103] R. Zamiri, A. Zakaria, R. Jorfi, G. Zamiri, M. Shokati Mojdehi, H. Abbastabar Ahangar, A. Khorsand Zak, *Laser assisted fabrication of ZnO/Ag and ZnO/Au core/shell*, J. Appl. Phys. A 111(2), 487-493 (2013).

[104] J.T. Jiu, M. Nogi, T. Sugahara, *Ag/*TiO_2 *core-shell nanocables prepared with a one-step polyol process*, J. Nanopart. Res. 14, 1241 (2012).

[105] *Ü*. *Ö*zgür Y.I., Alivov C., Liu A., Teke M.A., Reshchikov S., Doğan V., Avrutin S.J., Cho H., Morkoc, *A comprehensive review of ZnO materials and devices*, Journal of Applied Physics, 98, 041301 (2005).

[106] V. Coleman and C. Jagadish, Zinc Oxide Bulk, *Thin Films and Nanostructures: Basic Properties and Applications of ZnO*, Elsevier, Science Ltd, Oxford, pp. 1-20. (2006).

[107] Amy Dawson and Prashant V. Kamat, *Semiconductor-Metal Nanocomposites. Photoinduced Fusion and Photocatalysis of Gold-Capped* TiO_2 *(*TiO_2*/Gold) Nanoparticles*, Journal of Physical Chemistry. B 105, 960-966 (2001)

[108] Dmitri V. Talapin, Jong-Soo Lee, Maksym V. Kovalenko and Elena V. Shevchenko, *Prospects of Colloidal Nanocrystals for Electronic and Optoelectronic Applications*, Chem. Rev. 110, 389-458 (2010).

[109] Mahdi Ghazanfari, Fatemeh Johar, Ahmad Yazdani, *Synthesis and characterization of* Fe_3O_4*@Ag core-shell: structural, morphological, and magnetic properties*, Journal of Ultrafine Grained and Nanostructured Materials, Vol. 47, No. 2, pp. 97-103 (2014).

[110] Ie.V. Pylypchuk, Iu.P. Mukha, N.V. Vityuk, K. Szczepanowicz, L.P. Storozhuk, A.M. Eremenko, P. Warszy'nski, and P.P. Gorbyk, *Tryptophan-Stabilized Plasmonic* Fe_3O_4/Ag *Nanoparticles.*, Springer (August 2018).

[111] Maria Eugenia F. Brollo, RomanLopez-Ruiz, Diego Muraca, Santiago J.A. Figueroa, Kleber R. Pirota, and Marcelo Knobel, *Compact Ag@*Fe_3O_4 *Core-shell Nanoparticles by Means of Single-step Thermal Decomposition Reaction*, Scientific Reports 4: 6839 (2014).

[112] Thanh Dung Ngo, ThiMyHanh Le, The Huu Nguyen, Thien Vuong Nguyen, Tuan Anh Nguyen, Trong Lu Le, Thi Thai Nguyen, Thi Thanh Van Tran, ThiBichThao Le, and Ngoc Hai Doan, *Antibacterial Nanocomposites Based on* $Fe_3O_4 - Ag$ *Hybrid Nanoparticles and Natural Rubber-Polyethylene Blends*, International Journal of Polymer Science, Volume 2016.

[113] Phuong Nguyen-Tri, Van Thang Nguyen and Tuan Anh Nguyen, *Biological Activity and Nanostructuration of* $Fe_3O_4 - Ag$*/High Density Polyethylene Nanocomposites*, J. Compos. Sci. 3, 34 (2019).

[114] Prerana D. Tomke, Virendra K. Rathod, $Fe_3O_4@Chitosan-AgNP$ *nanocomposite for catalytic reduction of anthropogenic pollutant and agricultural pathogens*, International Journal of Biological Macromolecules 149, 989-999 (2020)

[115] Shiva Aghaei, Seyedhossein Hekmatimoghaddam, Mehdi Kalantar, Mohammad Hassan Sheikha, Mohammad Sobhan, Ali Jebali, $Fe_3O_4@Ag$ *Nanoprobe for Detection of Ovarian Cancer Cell Line Using Magnetic Resonance Imaging*, International Journal of Medical Laboratory 5(2): 123-132 (2018).

[116] Yuanfeng Pang, Chongwen Wang, Jing Wang, Zhiwei Sun, Rui Xiao, Shengqi Wang, $Fe_3O_4@Ag$ *Magnetic nanoparticles for micro RNA capture and duplex-specific nuclease signal amplification based SERS detection in cancer cells*, Biors and Bioelectronics 79, 574-580 (2016).

[117] Zhi Yong Bao, Jiyan Dai, Dang Yuan Lei, and Yucheng Wu, *Maximizing surface-enhanced Raman scattering sensitivity of surfactant-free* $Ag-Fe_3O_4$ *nanocomposites through optimization of silver nanoparticle density and magnetic self-assembly*, Journal Of Applied Physics 114, 124305 (2013).

[118] Araz Norouz Dizaji, Mehmet Yilmaz and Erhan Piskin, *Silver or gold deposition onto magnetite nanoparticles by using plant extracts as reducing and stabilizing agents*, Artificial Cells, Nanomedicine, and Biotechnology 44: 1109-1115 (2016).

[119] Ahmad Yazdani, Mahdi Ghazanfari and Fatemeh Johar, *Light trapping effect in plasmonic blockade at the interface of* $Fe_3O_4@Ag$ *core/shell*, RSC Adv., 5, 40989, 2015

[120] Teshome Senbeta, *Enhanced magneto-optical properties of* Fe_3O_4*@Au nanoparticles and its reverse core-shell nanostructure embedded in host matrix* SiO^2 , Photonics and Nanostructures - Fundamentals and Applications, (2023)

[121] Challa S.S.R. Kumar, *UV-Vis and PL Spectroscopy for Nanomaterials Characterizations*, Springer-Verlag Berlin Heidelberg, pp. 240 (2013).

[122] Vladimir V. Apyari, Stanislava G. Dmitrienko, Yury A. Zolotov, *Unusual application of common digital devices: Potentialities of Eye-One Pro mini-spectrophotometer A monitor calibrator for registration of surface plasmon resonance bands of silver and gold nanoparticles in solid matrices*, Sensors and Actuators B 188, 1109-1115 (2013)

[123] S.E. Starodubtcev, N.V. Korolev, A.F. Klinskikh, and P.A. Meleshenko, *Reduced polarizability and local-field effect in selfassembled ensemble of nanoparticles*, J. Nano- Electron. Phys., Vol. **5, No. 1**, pp. 1-5 (2013).

[124] H-M. Chang and C. Liao, *A Parallel Derivation to the Maxwell-Garnett Formula for the Magnetic Permeability of Mixed Materials*, World Journal of Condensed Matter Physics, 1, 55-58 (2011).

[125] Gashaw Beyene, Teshome Senbeta, and Belayneh Mesfin, *Size dependent optical properties of ZnO@Ag core/shell nanostructures*, Chinese Journal of Physics 58, 235-243 (2019).

[126] S.E. Starodubtcev, N.V. Korolev, A.F. Klinskikh, and P.A. Meleshenko, *Reduced polarizability and local-field effect in selfassembled ensemble of nanoparticles*, J. Nano- Electron. Phys., Vol. 5, No. 1, pp. 1-5 (2013).

[127] J.D. Jackson, *Classical Electrodynamics*, J. Wiley and Sons Inc. 3rd. Ed. (1999).

[128] H-M. Chang and C. Liao, *A Parallel Derivation to the Maxwell-Garnett Formula for the Magnetic Permeability of Mixed Materials*, World Journal of Condensed Matter Physics, 1, 55-58 (2011).

[129] Yan Zhao, Shuanghao Li, Yong Zeng, and Yijian Jiang, *Synthesis and properties of Ag/ZnO core/shell nanostructures prepared by excimer laser ablation in liquid*, APL Mater. 3, 086103 (2015).

[130] Challa S.S.R. Kumar, *UV-Vis and PL Spectroscopy for Nanomaterials Characterizations*, Springer-Verlag Berlin Heidelberg, pp. 6, 240 (2013).

[131] Ahmad Yazdani, Mahdi Ghazanfari and Fatemeh Johar, *Light trapping effect in plasmonic blockade at the interface of* Fe_3O_4*@Ag core/shell*, RSC Adv.,**5**, 40989, 2015

[132] Ezequiel Roberto Encina, and Eduardo A. Coronado, *Size Optimization of Iro n Oxide@Noble Metal CoreShell Nanohybrids for Photothermal Applications*, J. Phys. Chem. C, 18 Feb (2016).

[133] A. Chingsungnoen, P. Chaiyachate and T. Dasri, *Composite* Fe_3O_4*@Au Core-Shell Nanoparticle: Tunable and Enhancement of Optical Absorption Property*, Oriental Journal Of Chemistry, vol.33, No.(4), pp. 1642-1647 (2017).

[134] Fan, W. Z. *Effect of component volume ratio on the absorption spectra of Ag@*Fe_3O_4 *core-shell nanoparticles*. Modern Physics Letters B, 33(7), 1950071. (2019)

[135] Kheradmand, E. P. *Optical and magnetic properties of iron-enriched* $Fe/Fe_xO_y@Au$ *magnetoplasmonic nanostructures.* Applied Nanoscience. (2020)

[136] Shweta, B. J. *Near-field and far-field optical properties of magnetic plasmonic core-shell nanoparticles with non-spherical shapes: Adiscrete dipole approximation study.* AIP Advances (2019)

[137] Ahmad, Y. M. . *Light trapping effect in plasmonic blockade at the interface of* $Fe_3O_4@Ag$ *core-shell.* RSC Adv, 5, 40989.(2015)

[138] Poedji L. H., M. F. *Synthesis and Properties of* Fe_3O_4 *Nanoparticles by Co-precipitation Method to Removal Procion Dye.* International Journal of Environmental Science and Development, 4(3).(2013)

[139] Luciano, C. F. . *Waste Water - Treatment Technologies and Recent Analytical Developments: Applications of Magnetite Nanoparticles for Heavy Metal Removal from Wastewater.* (2013)

[140] Ana, O. R.-J. *Development of Multifunctional Liposomes Containing Magnetic/Plasmonic* $MnFe_2O_4/Au$ *Core-Shell Nanoparticles.* Pharmaceutics, 11(10).(2019)

[141] Kerker, M. (1969). *The Scattering of Light and Other Electromagnetic Radiation* (1st ed. ed.). New York, New York, USA: Academic Press.

[142] Papavassiliou, C. *Optical properties of small inorganic and organic metal particles.* Prog. Solid State Chem, 12, 185271-(1979).

[143] Vollmer, U. a. *Optical Properties of Metal Clusters*, (1st ed. ed.) Heidelberg: Springer. 978-3-642-08191-0 (1995)

[144] Maria, E. F., *Compact* $Ag@Fe_3O_4$ *Core-shell Nanoparticles by Means of Single-step Thermal Decomposition Reaction*. Scientific Reports(4), 683, (2014).

[145] Morones, J. R. *The bactericidal effect of silver nanoparticles. The bactericidal effect of silver nanoparticles*. Nanotechnology, 16(10), 2346-2353.(2005).

[146] Xu, R. M., *Ag nanoparticles sensitize IR-induced killing of cancer cells*. Cell Research, 19(8), 1031-1034 (2009).

[147] Teshome Senbeta, *Enhanced magneto-optical properties of* $Fe_3O_4@Au$ *nanoparticles and its reverse core-shell nanostructure embedded in host matrix* SiO_2, Photonics and Nanostructures - Fundamentals and Applications, (2023).

Chapter 6

Appendix

From Eqn. 3.2.1 to Eqn. 3.2.3, the coefficients A, B, C, D and F are unknown constants that can be determined using appropriate boundary conditions at the core/shell and shell/host interfaces. At this point it is worth noting that the second term on the right-side of Eq. (3.2.3) represents the induced potential outside the core-shell NP. The total induced field outside the concentric spheres represents the optical response of the system.

We may use the transfer matrices method for the spherical layers to obtain the expressions of the constants used in Eqns. 3.2.1, 3.2.2, 3.2.3. It is better to start with a single layer expression of transfer matrices and then the result can be generalized for multiple layers. For a single layer spherical nanoparticle embedded in host matrix the potential can be expressed as

$$\Phi = (Ar + \frac{B}{r^2})\cos\theta. \tag{6.0.1}$$

Using the boundary conditions for tangential of $\overrightarrow{E}$ and normal of $\overrightarrow{D}$ fields at r = R, as it is given by [147]

$$\left(A_1 R + \frac{B_1}{R^2}\right) = \left(A_2 R + \frac{B_2}{R^2}\right),$$

$$\varepsilon_1\left(A_1-\frac{2B_1}{R^3}\right)=\varepsilon_1\left(A_2-\frac{B_2}{R^3}\right),$$

These two equations can be written in a matrix form as

$$\hat{S}_1(R)\varphi_1=\hat{S}_2(R)\varphi_2, \tag{6.0.2}$$

where $\varphi_1=\begin{pmatrix} A_1 \\ B_1 \end{pmatrix}$, $\varphi_2=\begin{pmatrix} A_2 \\ B_2 \end{pmatrix}$ and

$$\hat{S}_n(R)=\begin{pmatrix} R & \frac{1}{R^2} \\ \varepsilon_n & -\frac{2\varepsilon_n}{R^3} \end{pmatrix}.$$

Here $n=1$ for core, $n=2$ for shell and $n=3$ for host matrix. The potential of the electric field at the center of the core nanoparticle is finite,

$$\varphi_1=\begin{pmatrix} A_1 \\ 0 \end{pmatrix}=A_1\begin{pmatrix} 1 \\ 0 \end{pmatrix}$$

With this φ_2 can be expressed as

$$\varphi_2=S_2^{-1}(R)\hat{S}_1(R)\varphi_1=\hat{M}\varphi_1,$$

where

$$\hat{M}=S_2^{-1}(R)\hat{S}_1(R), \tag{6.0.3}$$

and

$$S_n^{-1}=\frac{1}{3}\begin{pmatrix} \frac{2}{R} & \frac{1}{\varepsilon_n} \\ R^2 & \frac{R^3}{\varepsilon_n} \end{pmatrix} \tag{6.0.4}$$

Comparing Eq. (3.2.1) and Eqn(6.0.1) together with $B_1=0$, we see that $A=-E_0A_1$. This modifies the potential equation given by Eq. (6.0.1) for outer region as

$$\Phi_{out}=\big(-E_0r+\frac{B}{r^2}\big)\cos\theta. \tag{6.0.5}$$

and

$$\begin{pmatrix} -E_0 \\ B \end{pmatrix} = A\hat{M}\begin{pmatrix} 1 \\ 0 \end{pmatrix} = A\begin{pmatrix} M_{11} & M_{12} \\ M_{21} & M_{22} \end{pmatrix}\begin{pmatrix} 1 \\ 0 \end{pmatrix} \tag{6.0.6}$$

Performing the product operation in equation (6.0.6) gives

$$A = \frac{-E_o}{M_{11}}$$

and

$$B = AM_{21} = -E_o\frac{M_{21}}{M_{11}}$$

where B describes the amplitude of the scattered field. The above matrix representation can be generalized to multiple layers of NPs as follow:

$$\hat{M} = \prod_{n=1}^{N} \hat{S}_{n+1}^{-1}(r_n)\hat{S}(r_n) \tag{6.0.7}$$

Our model NPs consists of two concentric spherical layers; core and shell embedded in host matrix as illustrated in Fig.(3.1) and hence the number of layers are n = 2. For n = 2 Eq. (6.0.7) takes the following form

$$\hat{M} = \hat{S}_3^{-1}(r_2)\hat{S}_2(r_2)\hat{S}_2^{-1}(r_1)\hat{S}_1(r_1), \tag{6.0.8}$$

$$= \frac{1}{9}\begin{pmatrix} \frac{2}{r_2^2} & \frac{1}{\varepsilon_h} \\ r_2^2 & \frac{-r_2^3}{\varepsilon_h} \end{pmatrix}\begin{pmatrix} r_2 & \frac{1}{r_2^2} \\ \varepsilon_2 & \frac{-2\varepsilon_2}{r_2^3} \end{pmatrix}\begin{pmatrix} \frac{2}{r_1^2} & \frac{1}{\varepsilon_2} \\ r_1^2 & \frac{-r_1^3}{\varepsilon_2} \end{pmatrix}\begin{pmatrix} r_2 & \frac{1}{r_1^2} \\ \varepsilon_1 & \frac{-2\varepsilon_1}{r_1^3} \end{pmatrix}$$

It is clear that the final results of the above matrix product will give 2×2 matrices of the form

$$\hat{M} = \begin{pmatrix} M_{11} & M_{12} \\ M_{21} & M_{22} \end{pmatrix} \tag{6.0.9}$$

The complete evaluation of the matrices product indicated in Eq. (6.0.8) gives the values of M_{11} and M_{21} as follow

$$M_{11} = \frac{1}{9\varepsilon_2\varepsilon_h}\left[(2\varepsilon_2 + \varepsilon_1)(2\varepsilon_h + \varepsilon_2) + \frac{2r_1^3}{r_2^3}(\varepsilon_h - \varepsilon_2)(\varepsilon_2 - \varepsilon_1)\right] \tag{6.0.10}$$

$$M_{21} = \frac{r_2^3}{9\varepsilon_2\varepsilon_h}\left[(2\varepsilon_2 + \varepsilon_1)(\varepsilon_h - \varepsilon_2) + \frac{r_1^3}{r_2^3}(\varepsilon_2 - \varepsilon_1)(\varepsilon_h + 2\varepsilon_2)\right] \tag{6.0.11}$$

The electric polarizability a of the core-shell NPs embedded in the host matrix is defined as

$$\alpha = -4\pi\frac{M_{21}}{M_{11}} \tag{6.0.12}$$

Using Eqs. (6.0.10) and (6.0.11) in (6.0.12), we obtain the complete expression for α as [147]

$$\alpha = \left[\frac{(\varepsilon_1 + 2\varepsilon_2)(\varepsilon_2 - \varepsilon_h) + \nu_f(\varepsilon_1 - \varepsilon_2)(2\varepsilon_2 + \varepsilon_h)}{(\varepsilon_1 + 2\varepsilon_2)(\varepsilon_2 + 2\varepsilon_h) + 2\nu_f(\varepsilon_1 - \varepsilon_2)(\varepsilon_2 - \varepsilon_h)}\right]Dr_2^3. \tag{6.0.13}$$

Using Eqs (3.2.4) and (3.2.6), we found that the dipole moment of the system to be $\vec{p} = 4\pi\varepsilon_h F\vec{E}_h$ or it can be expressed by using Eq. (3.2.7). Thus the polarizablity and the Coefficient **F** related by the equation as

$$F = \frac{\alpha D}{4\pi} \tag{6.0.14}$$